TEMPORAL VARIABILITY OF THE IO PLASMA TORUS INFERRED FROM GROUND-BASED [SII] EMISSION OBSERVATIONS

Fabíola Pinho Magalhães

Doctorate Thesis of the Graduate Course in Space Geophysics, guided by Drs. Walter Demetrio Gonzalez Alarcon, Ezequiel Echer, and Mariza Pereira de Souza Echer, approved in September 16, 2016.

URL of the original document:
<http://urlib.net/8JMKD3MGP3W34P/3MC5SSH>

INPE

São José dos Campos

2016

TEMPORAL VARIABILITY OF THE IO PLASMA TORUS INFERRED FROM GROUND-BASED [SII] EMISSION OBSERVATIONS

Fabíola Pinho Magalhães

Doctorate Thesis of the Graduate Course in Space Geophysics, guided by Drs. Walter Demetrio Gonzalez Alarcon, Ezequiel Echer, and Mariza Pereira de Souza Echer, approved in September 16, 2016.

INPE

São José dos Campos

2016

Aluno (a): *Fabíola Pinho Magalhães*

Título: **"TEMPORAL VARIABILITY OF THE IO PLASMA TORUS INFERRED FROM GROUND-BASED [SII] EMISSION OBSERVATIONS"**

Aprovado (a) pela Banca Examinadora em cumprimento ao requisito exigido para obtenção do Título de *Doutor(a)* em

Geofísica Espacial/Ciências do Ambiente Solar-Terrestre

Dr. **Cristiano Max Wrasse**

Presidente / INPE / São José dos Campos - SP

Dr. **Walter Demetrio Gonzalez Alarcon**

Orientador(a) / INPE / SJCampos - SP

Dr. **Ezequiel Echer**
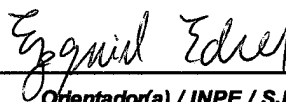
Orientador(a) / INPE / SJCampos - SP

Dra. **Mariza Pereira de Souza Echer**

Orientador(a) / INPE / São José dos Campos - SP

Dr. **Francisco Carlos Rocha Fernandes**
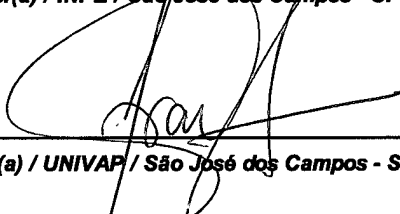
Convidado(a) / UNIVAP / São José dos Campos - SP

Dra. **Rosaly Mutel Crocce Lopes**

Convidado(a) / JPL/NASA / Passadena - Califórnia -

Dr. **Jeffrey Morgenthaler**

Convidado(a) / PSI / Estados Unidos - USA

Este trabalho foi aprovado por:

( ) maioria simples

(x) unanimidade

São José dos Campos, 16 de setembro de 2016

ACKNOWLEDGEMENTS

I will start thanking God, for making me believe and helping me to see my way through the end of this thesis. I also thank to my family, their support and presence was essential. My parents, brothers, sisters-in-law and my adorable nephews. I love you all!

To my friends, because without them sanity would be really hard. I thank all of them for listening, helping, supporting me as much as it could be possible.

I would like to thank Dr. Alisson Dal Lago and Dr. Polinaya Muralikrishna for being part of my first experiences at INPE. To Dr. Maria Virgínia Alves for her energy and sense of justice, always encouraging and helping us. To all my professors at INPE, I will take all the learning moments forever with me.

My profound thanks to my advisors: Dr. Walter D. Gonzalez Alarcon, Dr. Ezequiel Echer and Dr. Mariza Pereira de Souza Echer for the opportunity to participate in such an interesting project and also to trust my judgment. I enjoyed all the moments of discussion and new ideas, especially when i was not too confident with my results.

To the collaborators which I also consider as my advisors: Dr. Rosaly Lopes, Dr. Jeffrey P. Morgenthaler and Dr. Julie A. Rathbun. Each one had an important role helping on my thesis. I'm thankful for all the hours working and discussing the project. A special thank to Dr. Rosaly who kindly received me and supported me in all possible ways during my stay at the US.

And I hope this is not the end of a journey but the beginning of a new one.

ABSTRACT

Jupiter's magnetosphere is the largest one in the Solar System. It is a very complex system with several moons embedded, effects of planetary corotation and solar wind driven convection superposed, and several plasma physics processes occurring. Immersed within the magnetospheric plasma are the four Galilean moons which orbit around Jupiter. Io, the innermost of Jupiter's four Galilean moons, is the principal source of the magnetospheric plasma and responsible for nearly 1 ton/s of ions introduced into Jupiter's magnetosphere. Io has intense and energetic volcanic activity. The sulfur and oxygen present in Io's tenuous atmosphere, spewed by volcanoes, escapes forming an extended neutral cloud around Io and Jupiter. Subsequently, by ionization and pickup ions, a ring of charged particles encircling Jupiter is created, forming the Io plasma torus. The Io plasma torus is composed mainly of sulfur and oxygen ions. Also via atmospheric escape, an extended neutral is formed, composed mainly of sodium. The torus is about 2 Jupiter radii ($R_J = 71{,}492$ km) in width and is centered on Io's orbit around Jupiter at a distance of ~ 5.9 R_J. Considering this scenario, it is reasonable to expect that the Io plasma torus should be affected by changes in Io's volcanism. With that thought in mind, this thesis presents the analysis and results of the ground-based observations of the [SII] 6731 Å emission lines from the Io plasma torus for the year 1997. The observations occurred at the McMath-Pierce Solar Telescope at Kitt Peak and the data is part of a collaboration established during this thesis. The plasma torus is most dense around Io's orbit and from the [SII] 6731 Å emission lines we were able to obtain the brightness of both ansae. By conducting the Lomb-Scargle peridiogram we tried to measure the system III and IV periodicities. Due to a problem with scattered light too close to the ansae position, the results showed an amount of noise that does not allow a precise location of system IV. The importance to identify the system IV is the hypothesis that it is related to material radial transport through the Io plasma torus. Interactions between Io and the Jovian environment, particularly the Io plasma torus, are unique and not well understood. With this thesis we aim to improve the understanding of this complex coupled system.

Keywords: Io. Volcanism. Io Plasma Torus. Jupiter. Magnetosphere. Magnetosphere-ionosphere coupling.

ESTUDO DA VARIABILIDADE TEMPORAL DO TORÓIDE DE PLASMA DE IO INFERIDO A PARTIR DAS EMISSÕES DE [SII], DE OBSERVAÇÕES DA SUPERFÍCIE DA TERRA

RESUMO

Júpiter é o planeta que apresenta a maior magnetosfera do Sistema Solar. Imerso no plasma da magnetosfera estão as quatro maiores luas de Júpiter, conhecidas como Galileanas. O sistema de Júpiter é bastante complexo, principalmente devido às interações físicas que o envolvem. Io, a lua mais interna das galileanas, é a principal fonte de plasma e a responsável por cerca de 1 ton/s de íons introduzidos na magnetosfera do planeta. Io apresenta uma atividade vulcânica intensa e energética, responsável por formar a atmosfera tênue e não homogênea de Io. Parte do material presente na atmosfera de Io escapa formando uma nuvem neutra em torno de Io e Júpiter. Por ionização e troca de carga, um anel de partículas carregadas é formado ao redor de Júpiter, formando o chamado toróide de plasma de Io. O toróide de plasma é composto principalmente de íons de enxofre e oxigênio. Sua espessura é cerca de aproximadamente 2 raios de Júpiter ($R_J = 71{,}492$ km) e está centrada na órbita de Io, a uma distância de $\sim 5{,}9~R_J$. O material observado em Io é o mesmo encontrado no toróide de plasma e por esta razão é razoável esperar que a intensa atividade vulcânica de Io afete a variabilidade do toróide de plasma. A tese tem como objetivo apresentar análises e resultados provenientes de observações obtidas da superfície da Terra da linha de emissão do enxofre, na faixa do 6731 Å para o ano de 1997. As observações ocorreram no telescópio Solar McMath-Pierce, localizado no Kitt Peak. A região mais densa do toróide encontra-se em torno da órbita de Io e a partir das observações do enxofre ionizado é possível rastrear a parte mais densa do toróide e o brilho de cada "'ansa'". A partir da medida dos brilhos é possível obter-se as periodicidades de Júpiter. Para tal foi utilizado o periodograma de Lomb-Scargle. As interações existentes entre Io e Júpiter são únicas e muito dos seus processos físicos ainda não são compreendidos. Este trabalho tem como objetivo melhor compreender este sistema complexo acoplado.

Palavras-chave: Acoplamento magnetosfera-ionosfera. Io. Júpiter. Magnetosfera. Toróide de Plasma de Io. Vulcanismo.

LIST OF FIGURES

LIST OF TABLES

CONTENTS

1 INTRODUCTION

Over the last decades, several spacecraft have taken images and measurements of the Jupiter system. In situ measurements gave important information about Jupiter's magnetosphere, Io's volcanism and their interaction. Io is the innermost and smallest of the four Galilean moons (Io radii, $R_{Io} = 1815$ km). Its active and high-temperature volcanism is very variable and thanks to Galileo orbiter it was possible to observe significant eruptions and large plumes. Io's orbit lies at a distance of ~ 5.9 R_J (Jupiter radii, $R_J = 71,492$ km) and its rotational period is of ~ 42 hours. Io's active volcanic plumes expel a considerable amount of material to the atmosphere. The release of lava flows and plumes produces Io's patchy atmosphere, which is mainly composed by SO_2, SO, S, O (1). A significant fraction of the material lost to the atmosphere escapes as neutral atoms and molecules, mainly oxygen and sulfur atoms. The material which escapes from the gravitational pull of Io forms a neutral cloud that extends for several Jupiter's radii. The neutrals follow Io in its orbit about Jupiter until they are ionized through electron impact and charge exchange (2). Once ionized, the ions are accelerated to the nearly co-rotational flow of the ambient plasma, forming a torus of ions surrounding Jupiter, the Io Plasma Torus (IPT).

Figure 1.1 - Main components of Jupiter-Io coupled system.
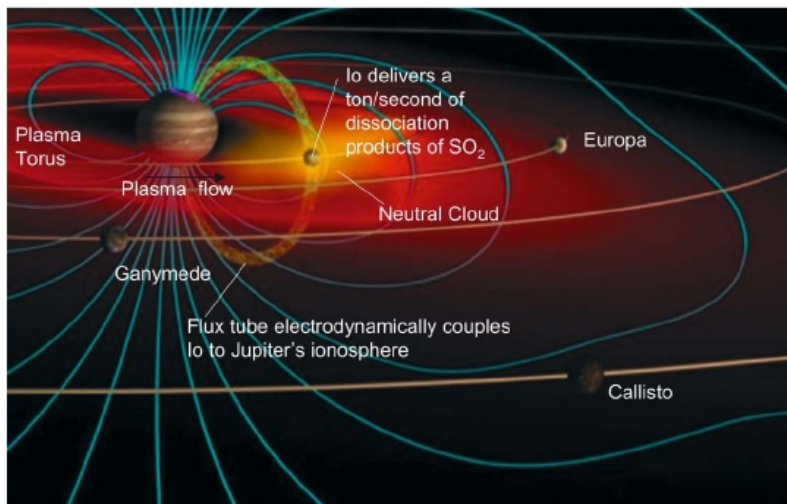
SOURCE: Lopes and Spencer (2007) (3)

Pioneer missions (10 and 11) revealed that Jupiter and Io were connected by an

electrical conduit known as the Io flux tubes[1] (4). The interaction between Io and the Jovian magnetosphere creates auroral and radio emissions at Jupiter (5, 6, 7). The flux-tubes, Io-Jupiter interaction and the four Galilean moons may be seen in Figure 1.1.

The first evidence of an electromagnetic connection between Io and Jupiter's magnetosphere was the detection of Io's control of the decametric (DAM) radio emissions, discovered by Bigg, E.K. (1964) (8). Brown and Chaffee (1974) (9) observed for the first time the sodium emission lines near Io, while the active volcanism on Io was discovered only in 1979 by the Voyager mission (10). Figure 1.2 shows the timeline of missions which studied the Jovian system and also the main discoveries during that period. The detection of the pair of emission lines at 6717 and 6730 Å in the vicinity of Jupiter was first evidenced by Kupo et al (1976) (11). The lines are identified by the forbidden doublet of [SII] at the Io Plasma Torus (IPT). The plasma torus is confined by the Jovian magnetic field and co-rotates with Jupiter at an angular velocity of $\Omega_J = 1.76 X 10^{-4}$ rad/sec, which corresponds to a rotational period of $\sim$ 10 hours.

The study of the Io-Jupiter interaction is an interdisciplinary subject and involves volcanology, atmospheric physics, astronomy, space geophysics, surface chemistry and plasma physics in its full complexity. Since the 1960s, the study of Io and Jupiter has not ceased. Although it's been more than fifty years, the scientific knowledge acquired from space missions and ground-based observations are quite recent and with questions to be answered. Monitoring programs from the ground and space are important tools and which will assist in understanding the system as a whole and how processes are connected.

---

[1]A flux tube is a cylindrical region of space containing a magnetic field. Both the cross-sectional area of the tube and the field contained may vary along the length of the tube, but the magnetic flux is always constant.

Figure 1.2 - Summary of the missions, artificial satellites and main discoveries of the Jovian system in the last decades. In green is highlighted the observations obtained at the Kitt Peak National Observatory (KPNO). The observations obtained during 1997 and 2008 are part of a collaboration with Dr. Jeffrey Morgenthaler. The results presented in this thesis are published for the first time.
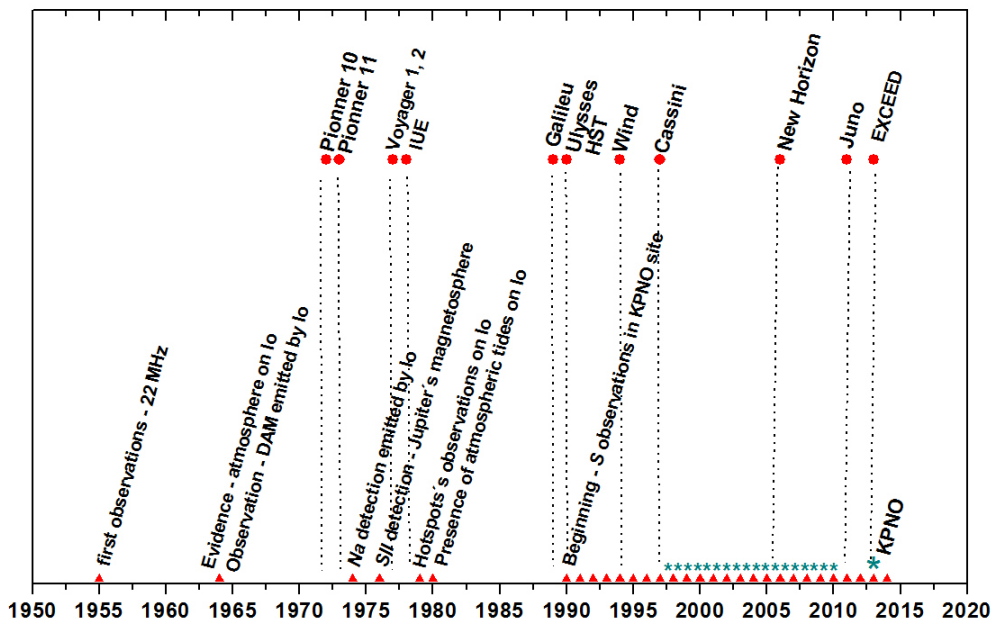
SOURCE: Author

1.1 Thesis motivation and Goals

The thesis main idea is to study how Io's volcanic activity is affecting its surroundings and Jupiter's inner magnetosphere. The study here presented was developed was based on Mendillo et al. (2004) (1) and Brown & Bouchez (1997) (12). Mendillo et al. (2004) (1) developed an interesting work where the main purpose was to understand how the changes in brightness of Jupiter's extended sodium nebula are related to the infrared emission brightness of Io. The enhancements in the infrared (IR) seems to be related to the levels of volcanic activity (lava flow). From that came the idea to work with the data of the Galileo orbiter instrument, the Near Infrared Mapping Spectrometer (NIMS). As it is going to be explained in the following chapters, the NIMS instrument measured thermal emissions of Io's surface. The measurements allow us to map Io's thermal emissions (eruptions) during the

3

the period of the Galileo mission, 1996-2003.

Brown & Bouchez (1997) ([12](#)) presented the results of sodium and sulfur observations during a period of six months in 1992. They also wanted to understand the role of volcano outbursts in the extended neutral cloud and the ionized sulfur at the plasma torus. The results showed that the Na mass increased while the plasma torus remained undisturbed. The plasma torus started to show a slow increase in intensity after the sodium mass had a considerable increase. That behavior was expected as the plasma torus brightness becomes proportional to the ionization and charge-exchange rates. Concerning the estimation in magnitude of Io's outburst, the subsequent increase in the S plasma mass following the Na outburst shows that atomic S must have increased in mass at the same time as atomic Na. According to their studies, the mass of Na is a direct tracer of the mass of the more dominant S component. Results from the Voyager's (1 and 2) mission imaged the same plumes during the four month period between both missions. Pele's plume, the largest one observed, was the only one to have turned off between Voyager 1 and 2 flyby. The results lead to believe that the largest plumes are the most variable ones. Another interesting aspect in their work ([12](#)) is the attention to time influence of an observed outburst to the increase in brightness of the neutral Na cloud and the plasma torus emission intensity. They had models to give a better understanding about supply and loss of the system.

Io is a very important driver of the magnetospheric physics at Jupiter. Its volcanism is responsible for the supply of ions to the whole magnetosphere. The conditions existing between the planet and the moon leads to an unique interaction between Io and Jupiter. The main goal of this thesis is to understand how the volcanic material escaping from Io, using the thermal emission data from the Near Infrared Mapping Spectrograph (NIMS/Galileo) instrument is affecting the Io plasma torus by using ground-based observations of the sulfur ionized emission lines at the 6731 Å. As it will be developed along the thesis chapter, due to some problems the final results are only part of the data initially established.

1.2 Thesis organization

Chapter two gives more details concerning Jupiter. Chapter three describes Io's main characteristics, such as volcanoes and plumes. The fourth chapter describes the Io plasma torus, its composition and structure, and also a description of the sulfur ionized lines. In Chapter five is presented the methodology developed and implemented in this thesis, with the instruments descriptions and the problems

found during reductions. Chapter six shows the results, and then conclusions and future work in chapter seven.

2 Jovian System

The region of space containing magnetic fields and plasma of solar origin is called heliosphere. Its composition is dominated by solar wind protons and electrons. The solar wind consists of magnetized plasma traveling outwards from the Sun at super-magnetosonic[1] speeds (13). Near the heliospheric equator the speed is $\sim$ 400 km/s (remembering the density of the material expelled from the Sun decreases with the squared distance).

It has been more than five decades since space missions started to explore the Jovian system. The success and discoveries of a mission have always boosted the development and launch of the others. The understanding of the Sun, the planets and moons have always helped us to understand the evolution of the Solar System and in particular the Earth. This chapter introduces important concepts of Jupiter and an overview of space missions, which at some point measured or imaged Jupiter and its Galilean moons.

2.1 Jupiter

Jupiter is the fifth planet in our planetary system, and it is located at 5.2 Astronomical Units (1 AU = 149 597 871 km) from the Sun. The sunlight which hits Jupiter is 25 times weaker than that reaches the Earth and Jupiter's orbit solar wind pressure is only 4 % that of Earth's one. Jupiter is mainly composed of hydrogen and helium and has a density of 1.326 g/cm^3. It does not have a solid surface and it has clouds made up of hydrogen and helium. Voyager 1 spacecraft discovered the presence of three thin rings around Jupiter in 1979, and are really difficult to be observed. The Jovian magnetosphere is rapidly rotating and full of plasma, while the Earth's magnetosphere has neither of these properties. Jupiter rotates in only 9 hours 55 minutes which is quite fast considering its immense size. Jupiter's magnetosphere is the largest object in the solar system, second after the heliosphere, and its large magnetic moment is smaller only than the Sun's.

A magnetic field may be detected directly using an in situ magnetometer or indirectly via effects of acceleration charges which consequently produce radiation, such as radio emissions. Another indication of magnetic field in a planet can be known by observations of localized aurorae (15).

---

[1]Just like the case of the air, where pressure and density differences travel at the speed of sound. In the magnetized plasma, pressure and density disturbances travel with magnetosonic speed.

Table 2.1 - Jupiter's main physical characteristics (14).

Jupiter	
Equatorial radius (km)	71,490
Semi-major axis (AU)	5.2
Mass (kg)	1.9×10^{27}
Orbital period (years)	11.9
Albedo	0.34
Magnitude (V_0)	2.70

Planetary magnetospheres are formed by the interaction of the planet's electromagnetic environment with the flow of the solar wind (16). That area of space surrounding the planet controls the motion of charged particles, influenced by the planet magnetic field (17). In general, magnetospheres can be 10 to 100 times larger than the planet itself and the shape is directly connected with the strength of the magnetic field. The planetary magnetosphere may be due to intrinsic fields (solar wind + planet field) or induced (interaction solar wind + planet's ionosphere). Due to the existence of such structures, the solar wind is prevented to affect the planet directly. Charged particles are observed in the magnetospheres, whose origins may be the solar wind, the planet's ionosphere, satellites or the ring current particles whose orbits are involved by the planet's magnetosphere (15). The overall drift motion of charged particles in a magnetosphere is governed by the gradient in the magnetic field strength, by the field line curvature and by the presence of electric fields. Electric fields perpendicular to magnetic field lines cause both ions and electrons to drift in the same direction and thus the potential difference is not decreased by a current, and such large scale electric fields can be stable (18).

There are two different processes which may generate the magnetosphere. In the case of the planets Venus, Mars and the comets, they are induced by the interaction of the solar wind with the body's ionosphere. Examples of magnetospheres produced due to the solar wind interaction with the planet magnetic field via a dynamo process are the Earth and the giant planets. Earth and Jupiter's magnetospheres resemble each other, but Jupiter's is over three orders of magnitude larger and the magnetotail extends beyond Saturn's orbit, has an internal source of plasma and fast rotation, and analogous to the Earth's Van Allen belts, there are radiation belts close to the planet (15). Jupiter has been widely observed, both by in situ and remote observations. Photon emissions occur at the ultraviolet and visible wavelengths while the accelerated electrons are observed at radio wavelengths.

Figure 2.1 - Illustration of Jupiter's magnetosphere from the meridian of the noon-midnight. Io is located in the inner magnetosphere of Jupiter. Io plasma torus and the current sheet are represented.
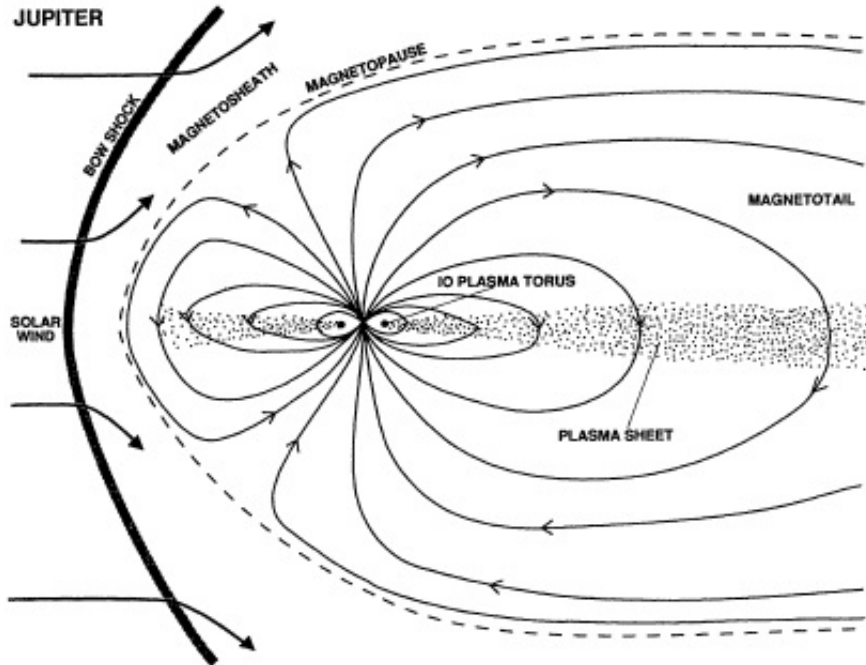
Jupiter's magnetosphere is classified in three principal regions: inner, middle and outer magnetosphere (18). The regions were divided such that the inner magnetosphere extends from the planetary surface to 10 R_J (Jovian radii where 1 $R_J = $ 71,492 km). The innermost Galilean moon of Jupiter, Io, lies within the inner magnetosphere. In this region the currents from the interior of Jupiter are dominant. The time-scale for field variations, both in magnitude and direction are long (20). The plasma predominantly supplied by the ionization of SO_2 is originated from Io at a rate of 1 ton/s or 10^{28} ions/s (21, 22). The middle magnetosphere is between 10-40 R_J (23), while the outer magnetosphere is considered to be ≥ 40 R_J. The inner magnetosphere is strongly controlled by Jupiter's magnetic field fast rotation; the plasma being approximately co-rotational (20). The middle magnetosphere is the region where the effects of an azimuthal current sheet in the equatorial plane produce a significant perturbation, leading to the stretching of the magnetic field lines in the radial direction. The outer magnetosphere is the region where the field has a large southward component and exhibits large temporal and/or spatial variations

9

in magnitude and direction in the response of changes in the solar wind pressure. This region includes the extensive Jovian magnetic tail (18).

2.1.1 Periods of Jupiter

Jupiter does not have a solid surface and for this reason the creation of a coordinate system, such as latitude and longitude, needs previous explanation. Coordinate systems are normally established on a solid surface. The rotation of the equator of a planet is obtained from observations, for example, of the movement of the clouds, so that the direction of the axis of rotation is determined with relative accuracy. The longitude is obtained by setting an arbitrary prime or zero meridian of longitude. In the case of the Earth, the prime meridian is at the Royal Observatory Greenwich. In Jupiter's case, the problem of establishing a longitude system is that the average period of rotation of the clouds is a function of latitude. The equatorial region rotates faster than the temperate and polar regions (20). The solution to this problem was to establish two separate longitude grids. The System I (λ_I) applies to high clouds (no polar), within 10° of the equator. The System II (λ_{II}) applies to higher latitudes, above 10°. However, another longitude system became necessary when radio signals were detected. It was observed that the magnetic field rotates at a rate intermediate between Systems I and II. Thus System III (λ_{III}) which describes the rotation of the Jovian magnetic field (20) was created. There are two latitude systems for Jupiter. There is the Jovigraphic system with the latitude measured positive northward from the spin equator and the magnetic latitude system defined by a centered tilted dipole. The northern end of this dipole is tilted 10° toward $\lambda_{III} = 200°$, and the southern end is, of course, tilted 10° toward $\lambda_{III} = 20°$. This explanation may be better understood with the illustration in Figure 2.2.

Figure 2.2 - Jovian coordinate convention. The view is from above the north pole with the
eastern (E) and western (W) sides of Jupiter as seen from the Earth (the ter-
restrial convention, east on the right and west on the left). The prime merid-
ian rotates counterclockwise at a constant rate Ω_J. Longitude is measured
clockwise from this prime meridian. This illustration shows the longitude of
some object (a satellite, spacecraft, or phenomenon) marked X. Although it
is shown λ_{III}, the same conventions goes for λ_I and λ_{II}, the only difference
being the numerical value of Ω_J, which is different for each system. And also
what causes the three prime meridians to move relative to each other.
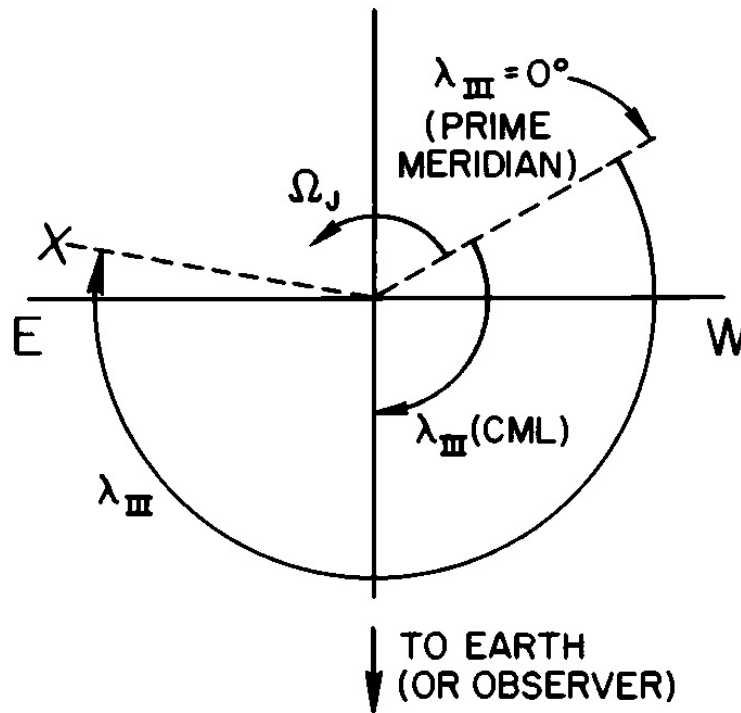
But a variation was identified in the frequency of Jupiter's rotational period. Then
this new possible period was known and named as System IV (λ_{IV}). The System IV
period is still not established since its characteristic and origin are not completely
understood. Previous works have observed the System IV and the periods obtained
were: Sandel Dessler's (1988) (24) was of 10.224 hours; Brown (1995) (25) 10.214 $\pm$
0.006 hours. Woodward (1994) (26) reanalyzed data from Roesler et al. (1984) (27)
and obtained a period of 10.2 $\pm$ 0.12 hour and their own ground-based observations
obtained a period of 10.14 $\pm$ 0.06 hour. Nozawa et al. (2004) (28) obtain a period

for the System IV of 10.18 ± 0.06 hours. Steffl et al (2006) (29) 10.07 ± 0.0039 hours. The summary of the Systems may be seen on Table 2.2. The time sequence of brightness values of each ansa can be used to investigate the presence of the System IV period.

Table 2.2 - Rotation period of the four systems observed in Jupiter.

System	Rotation Period	Reference
λ_I	9h 50' 30"	(30)
λ_{II}	9h 55' 40.6"	(30)
λ_{III}	9h 55' 29.71"	(31)
λ_{IV}	10h 20'	(27)
	10.224 h	(24)
	10.214 ± 0.006 h	(25)
	10.2 ± 0.12 h	(26)
	10.18 ± 0.06 h	(28)
	10.07 ± 0.0039 h	(29)

2.2   Missions to Jupiter

Including Juno, nine spacecraft have taken images and measurements of Jupiter and its moons. The first mission to start Jupiter's exploration was the Pioneer 10. It was launched in 1972 and was the first spacecraft to obtain images and make direct observations of Jupiter. The acknowledge of the intense radiation environment near Jupiter helped design the Voyager and Galileo spacecraft. The Pioneer 11 was launched on April 1973 and arrived at Jupiter in September 1979. The next missions to Jupiter were the Voyager space probes 1 and 2. They were identical copies of each other and were launched a few weeks apart. Both made important discoveries concerning Jupiter and the moons (14).

The Voyager missions were launched in 1977 and the initial objectives were to study Jupiter, Saturn and their respective moons. The Voyager 2 mission was extended to explore Uranus and Neptune and became the only spacecraft to study all four giant planets. After the year 1990, it started the *Voyager Interstellar Mission* with the objective to go beyond the Solar System. Thirty years after its launch, Voyager missions seem to have finally crossed the boundary and reached the heliopause

In the 1990s, ESA and NASA launched the Ulysses mission. The main goal was to explore the poles of the Sun. However, placing the probe in a polar orbit around the

Sun is not an easy task and it was necessary to obtain enough energy. The best option was to use the gravity assist of Jupiter. Although the scientific investigations at Jupiter were secondary objectives, the Jovian magnetosphere was explored as much as possible during the Ulysses - Jupiter flyby. The closest approach of Ulysses to Jupiter was in 1992. It passed through the Io Plasma Torus and the radio instrument measured the electron density distribution in the torus. Table 2.3 is a summary of all missions that explored Jupiter. It shows the year, the missions that reached the Jovian system and the mission's main purpose.

Table 2.3 - List of missions which studied the Jovian system. Information were obtained from the respective mission's website.

Mission	Launch	Jupiter Approach	Mission Goals
Pioneer 10	Mar/1972	Nov/1973	Jupiter's atmosphere, magnetosphere and moons, particularly Io, and dust distribution
Pioneer 11	Apr/1973	Dez/1974	Masses, interiors, atmospheres, moons and rings of Jupiter and Saturn
Voyager 1	Sep/1977	Mar/1979	Atmospheres, interiors, moons and magnetospheres of Jupiter and Saturn
Voyager 2	Aug/1977	Jul/1979	Explore all of the outer planets and their moons
Galileo	Oct/1989	Dez/1995	Jupiter and its moons, especially Europa and Io
Ulysses	Oct/1990	Feb/1992	Characterize the heliosphere as a function of solar latitude
Cassini	Oct/1997	Dez/2000	Saturn, its rings, icy moons, magnetosphere, and Titan
New Horizons	Jan/2006	Feb/2007	Understand the icy worlds at the edge of our solar system
Juno	Aug/2011	Jul/2016	Improve our understanding of the formation, evolution and structure of Jupiter

The Juno mission made the insertion orbit in the beginning of July of this year (2016). After the final tests and instrument calibrations, the science instruments will start working in October. Its main objectives are to study Jupiter's magnetic field, and the massive radiation belts, in order to have better answers concerning Jupiter's formation and how our entire solar system evolved. It will also take the time to observe aurorae. Besides Juno, another mission is approved and set to launch in 2022, a mission of the European Space Agency (ESA), JUICE (JUpiter ICe moons Explorer). The main goal is to study the icy moons Ganymede, Europa, and Callisto. The investigation proposes to study the composition of the icy moons, search for liquid water and also study the active geologic process. Unlike Io, the other three Galilean moons have their surface covered with frozen water.

The Japanese Aerospace Exploration Agency (JAXA) launched in 2013 the extreme ultraviolet (EUV) telescope called EXCEED (Extreme Ultraviolet Spectroscope for Exospheric Dynamics), on board the satellite SPRINT-A. The artificial satellite has the goal to observe tenuous gases and plasma around the planets in the Solar System (32). Its main target was Jupiter and to observe the IPT variability. The results may give new important insights concerning the IPT and Jupiter's aurorae. This overview aims to show that much has been achieved with all these decades of observations but it is still important the Jupiter's system in situ exploration, especially as many of the features may only be observed from space and close to the planet (or moon).

2.2.1 Galileo mission

After 12 years of development, Galileo mission consisted of two spacecraft, an orbiter and an atmospheric probe. It was launched on October 18, 1989. The spacecraft arrived at Jupiter on December 7, 1995, and had its end of mission on September 21, 2003, after fourteen years in space and eight years orbiting the Jovian system. The spacecraft used gravitational assist flybys of Venus and Earth to reach Jupiter, a trajectory called VEEGA (Venus-Earth-Earth Gravity Assist). Table 2.4 shows the 10 scientific instruments on board Galileo and a brief description of the instruments primary measurements. The main goal of Galileo mission was to study Jupiter and its moons, specially Io's volcanoes and the surface modification processes. The orbits were elaborated to be elongated ellipses around the planet, with each orbit taking about two months to be completed. The original two year orbital missions were extended three times to take advantage of the spacecraft's continuing capability to return valuable scientific information about the Jupiter system. The extended missions were Galileo Europa Mission (GEM) between 1998-1999, and the Galileo

Millennium Mission (GMM) between 2000-2002. Each of the 34 orbits of the Galileo mission may be seen in Figure 2.3. These long periods were important for observations of Io, since all the high-resolution data obtained by the mission were acquired during this period (33).

Table 2.4 - Galileo science payload (34).

Device	Primary measurements
Solid State Imager (SSI)	Map Galilean satellites at roughly 1-km resolution, and atmospheric circulation
Near-Infrared Mapping Spectrometer (NIMS)	Surface composition, atmospheric composition and temperature
Ultraviolet Spectrometer (UVS)	Gases and aerosols, auroral emissions, satellite airglow
Extreme Ultraviolet Spectrometer (EUV)	S, O ion emissions of the Io torus
Photopolarimeter-Radiometer (PPR)	Distribution of atmospheric particles; surface temperatures of the satellites
Magnetometer (MAG)	Monitor magnetic field for strength and changes
Energetic Particle Detector (EPD)	High-energy electrons, protons, and heavy ions in the magnetosphere
Plasma Subsystem (PLS)	Composition, energy, and 3-D distribution of electrons and ions
Plasma Wave Subsystem (PWS)	Electromagnetic waves and wave-particle interactions
Dust Detector Subsystem (DDS)	Mass, velocity, and charge of dust particles
Heavy Ion Counter (HIC)	Composition, and energy of low-energy ions in the environment

Flybys of the Galileo spacecraft were used to study the thermal structure and sulfur dioxide distribution of active volcanoes (35). The initial plan was for Galileo to have 11 orbits around Jupiter. During each orbit, Galileo and Jupiter were in solar conjunction, except for orbit 5th. Flybys at the Galilean moons were: 4 flybys of Ganymede, 3 flybys of Callisto, and 3 flybys of Europa. Although there were some difficulties and problems with the instruments, the discoveries on Europa made NASA to approve the first extension mission, GEM. The following extended mission was GMM. During the GMM a great opportunity came as in late 2000's as the Cassini spacecraft was also at Jupiter's neighborhood, passing on its way to Saturn. During orbit 29 in late December 2000, Galileo and Cassini obtained complemen-

Figure 2.3 - Galileo orbital tour around the Jupiter system.
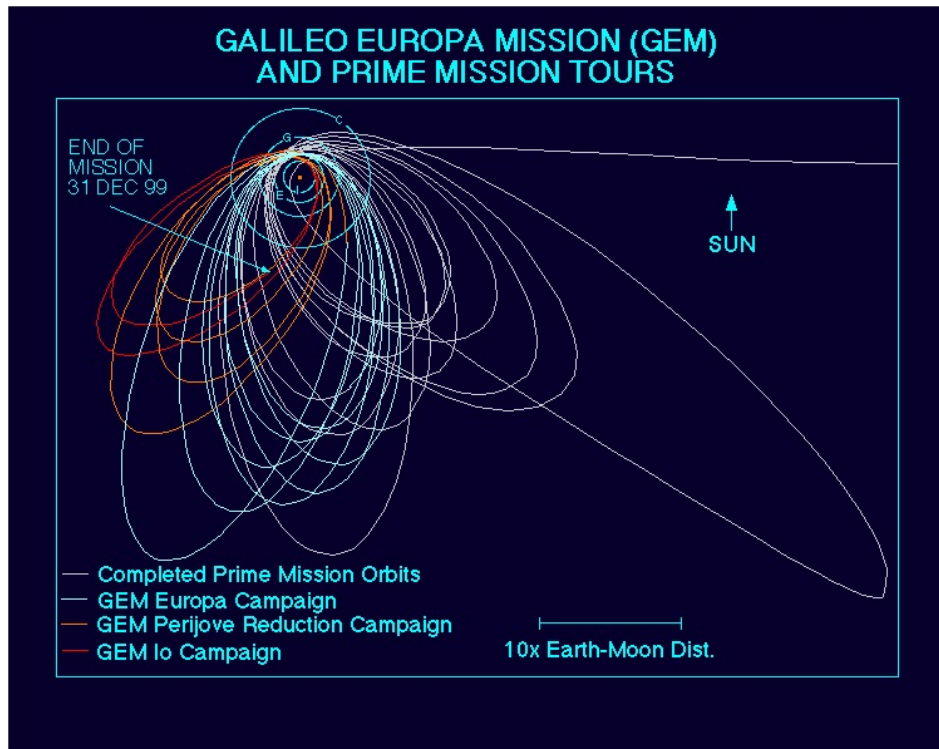
SOURCE: *solarsystem.nasa.gov/galileo/mission/journey − orbital.cfm*

tary coverage of Io, with Cassini providing better spectral and temporal coverage thanks to its more sophisticated imaging system and higher bandwidth, and Galileo providing better spatial coverage since it observed Io from a much closer distance.

The only Io flyby during Galileo nominal mission occurred at an altitude of 897 km over 8.5° south latitude, 101.1° west longitude (36). The orbits 12 through 19 was focused on Europa. The orbits 20 through 23 made flybys on Callisto. On October 11, 1999 was set a flyby on Io during orbit 24 at 611 km and another at orbit 25 at 301 km distance. The flyby at orbit 24 was an equatorial one and the spacecraft came 500 km close of Io's surface (34). Other flybys occurred at orbit 21, at 140,000 km of distance and orbit 27 on February 22, 2000. The three final Io flybys were orbits 31 and 33 in 2001-2002.

Io was observed in almost every orbit, which helped monitor Io's active volcanic vents and search for surface changes. An important period of activity occurred at Pillan patera during late June and early July in 1997 (orbit 9th). During that period some remarkable surface changes were observed. NIMS and SSI instruments together

([37](#)) were able to identify a total of 71 hotspots[2] by the end of the Galileo mission. The SSI was able to detect hotspots with temperatures higher than 700 K, while Io was in eclipse by Jupiter. The instruments used to monitor volcanism on Io were the Solid State Imaging (SSI), the Near Infrared Mapping Spectrometer (NIMS) and the Photo-Polarimeter Radiometer (PPR). The combination of the information obtained by the three equipments helped to improve the understanding of Io's volcanism.

---

[2]Hotspot denotes an active or recently active volcanic region, recognized by the observation of thermal emission significantly above the NIMS detection limit of 180 K (**??**)

3 Io - The volcanic moon

3.1 Introduction

The interior, the structure and composition of the moons are constrained by gravity and magnetic field of the main planet, and information from imaging and infrared observations (38). Voyager 1 spacecraft observed for the first time Io's volcanic activity (10) and since then Io (Figure 3.1) has been extensively studied and observed in an attempt to understand its volcanism and the interaction with the Jovian magnetosphere.

Figure 3.1 - Galileo image from Io taken on July 3rd, 1999. The image is a mosaic which used the near-infrared, green and violet filters. Most of Io's surface has pastel colors, punctuated by black, brown, green, orange, and red units near the active volcanic centers.
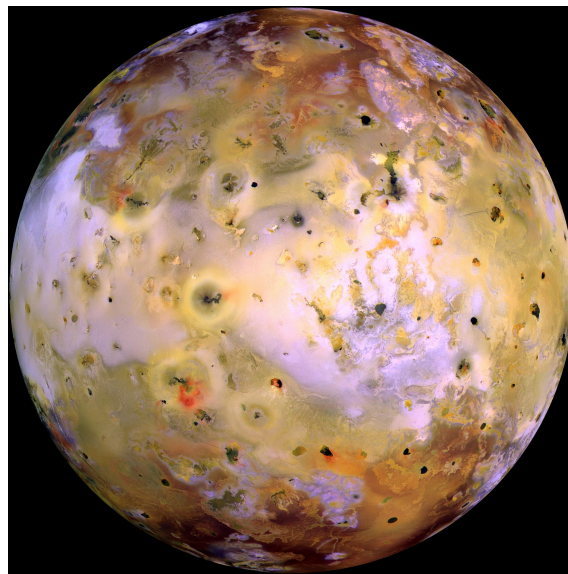
SOURCE: photojournal.jpl.nasa.gov/catalog/PIA02309

Io is part of the four Galilean moons and different from the others, Io has no water in its interior. Besides the water, all four Galilean moons have their main internal constituents made of metal and rock. Europa is a rocky body, with a surface of water ice and has a radius of 1565 km, slightly smaller than the Moon, which radius is 1737 km. The possibility of liquid water and also the proportion of rock to ice places Europa on the list of objects with astrobiological potential. The daytime surface

temperature was found to range from 120 to 135 k. Europa's density and icy surface suggest that it is primarily a silicate body that is partly differentiated. Ganymede, the third Galilean moon counting from Jupiter, is normally referred as the moon with the size of a planet. It is the largest moon known in the solar system, has a radius of 2631 km, and it is larger than the planet Mercury (2440 Km), aside being 3/4 of the size of the planet Mars (3390 km). Ganymede's geology does not give any indication of a subsurface of liquid layer, however the presence of a magnetic field is a good indication of layer of salty water below its icy surface (39). Callisto is a body covered by impact craters with different sizes. It is the second largest moon of Jupiter, with a radius of 2400 Km. It is the only Galilean moon to find itself at the outer magnetosphere of Jupiter. Figure 3.2 shows a picture of the four Galilean moons represented in scale and their main surface features. It is really interesting to observe how the four Galilean moons have different characteristics. According to the study developed by Heller and Pudritz (2015) (40), the results indicate that the Galilean moons were formed during the final stages of accretion onto Jupiter. Table 3.1 gives general features of the Galilean moons.

Figure 3.2 - The four Galilean moons shown in increasing distance from Jupiter: Io, Europa, Ganymede, and Callisto (from the left to the right). Their appearance are amazingly different even though they are relatively close to Jupiter, 350.000 kilometers for Io; and 800.000 kilometers for Callisto. These images were acquired on several orbits of the Galileo mission. Io is the most colorful of the Galilean moons. Its surface is covered by deposits from actively erupting volcanoes, hundreds of lava flows, and volcanic vents. Europa has a surface composed almost completely of water ice. Ganymede has a distinctive surface characterized by patches of dark and light terrain. And Callisto's dark surface is marked by numerous bright impact craters.
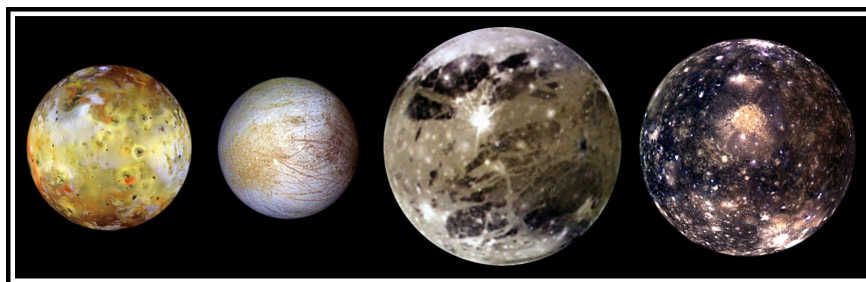
SOURCE: NASA/JPL/DLR

Io is the most volcanically active body known in the solar system and the innermost

Table 3.1 - General features of the Galilean moons. The mean distance is given related to Jupiter's center (www.nasa.gov).

Galilean moon	Equatorial radius (km)	Mass (kg)	Distance (km)	Sideral rotation period (days)	Magnitude (V_0)
Io	1815	8.94×10^{22}	421.600	1.7691	5.02
Europa	1569	4.8×10^{22}	670.900	3.5511	5.29
Ganymede	2631	1.48×10^{23}	1070.000	7.1545	4.61
Callisto	2400	1.08×10^{23}	1883.000	16.689	5.65

of the four Galilean moons. Its radius is 1821 km, the density is 3.53 g/cm^3, and has an orbital radius of 421,600 km (41). Io finds itself within Jupiter's inner magnetosphere and has no intrinsic magnetic field (42). Io's heat flow is of order 2.5 W/m^2 (43) and is the result of intense tidal heating, which generates widespread volcanic activity. The internal heating is due to distortions in Io's shape caused by the intense gravity of Jupiter and on a smaller scale by the gravity of Europa and Ganymede (44). It differs from the Earth's internal heating case which is due primarily to radioactive isotope decay. The massive heating of Io's interior was first described by Peale et al. (1979) (44). All four Galilean moons have spin and orbit synchronous, which means they always have the same face toward Jupiter. The moon's period are linked precisely by the expression $n_1 - 2n_2 = n_2 - 2n_3 = \nu$, where n_i is the mean motion of the moon. The orbital resonance between the Galilean moons is given so that every time Ganymede orbits Jupiter, Europa orbits it twice and Io orbits it four times (Figure 3.3). Their orbital resonance is known since the Voyager missions.

Figure 3.3 - Illustration resonance of Io, Europa and Ganymede
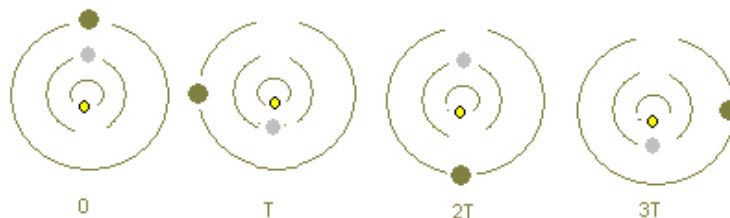
SOURCE: Person Education

Io's resurfacing is deeply connected with the volcanic plumes, lava flows and lava lakes that constantly bring new materials from the interior to the surface, keeping the resurfacing high. Io's colorful surface is due to different silicate and sulfur compounds. The surface temperature on Io at noon reaches a maximum of $\sim$ 128 k (45) and at night reaches a maximum of $\sim$ 95 k (46). Io has over 400 active volcanoes and more than 100 mountains. Most mountains on Io are not of volcanic origin, but are typically broad plateaus bounded by steep scarps or tilted blocks of layered crust (47). Most common volcanic landforms are the paterae, flat-floored depressions that are often irregularly shaped (48, 49). They may range from 2.5 to 200 km across. Its volcanic plumes and lava flows produces large surface changes and the materials produced by this volcanism make up Io's thin, patchy atmosphere. Io's volcanic ejecta also produce a large plasma torus around Jupiter. Table 3.2 presents some of the physical properties of Io.

Table 3.2 - Comparison of Io and Earth physical parameters. Adapted from Davies (2014) (50)

	units	Io	Earth
Equatorial radius	(km)	1826.5 ± 0.12^{b}	6378.3
Mean radius	(km)	1821.6 ± 0.5^{c}	6371.0
Surface gravity	(m/s^2)	1.796	9,8
Mass	(kg)	8.935×10^{22}	5.976×10^{24}
Volume	(m^3)	2.52×10^{19}	1.08×10^{21}
Mean density	(kg/m^3)	3527.5 ± 2.9^{c}	5517
Sidereal rotation period	(hours)	42.456	23.9345
Albedo		0.63	0.39
Heat flow (mean)	(W/m^2)	$\geq 2^{e}$	0.07^{d}

[b] Davies et al. (1998)

[c] Anderson et al. (2002)

[d] Turcotte and Schubert (1986)

[e] Veeder et al. (1994)

3.2   Io volcanism

Volcanism is known to change the surface of terrestrial bodies during their active period. The effects of past volcanic activity were observed on terrestrial bodies such as the Earth, the Moon, Venus, Mars, and Io. Currently there are four known active worlds in the solar system: Earth, Saturn's moon Enceladus, Neptune's moon Triton and of course, Io (50). But what is the definition of volcanism? When extra-terrestrial volcanoes were discovered, the traditional definition given to volcanoes observed on

Earth needed to undergo a few changes. Volcanic materials and eruptions on extra-terrestrial worlds can be quite different from the Earth. Broadly speaking it involves molten rock, gas, a hill or a mountain build up around a place or a opening but mainly the material erupted. A good definition for volcanism is given by (51): "*A volcano is an opening on a planet or moon's surface from which magma, as defined for that planetary body, is erupted*". The only other body besides Earth we have collected rocks and brought back to our planet is our Moon.

Three styles of volcanism were observed on Io and they are classified as: flow-dominated (known before as *Promethean*); explosion-dominated (known before as *Pillanian*), and Intra-patera (known before as *Lokian*) (52). The flow-dominated type was first observed at Prometheus volcano, but also later identified at Culann, Zamama, and Amirani. These volcanic centers are originated from either paterae or fissures and produce extensive compound lava flow fields (33). Their eruptions are steady, long-lived, lasting over years and normally are associated with small explosive plumes (< 200 km high) of vaporized sulfurous material (52). Prometheus image may be seen in Figure 3.4. The second type is called explosion-dominated, characterized as short-lived, with intense eruptions and high-temperatures. They are originated from either paterae or fissures, and produce extensive dark lava flow fields. They produce really vigorous outbursts and occur during short periods of time (lasting from days to a couple of months). The outbursts are the most dramatic infrared events and have very high fluxes and temperatures (41). These eruptions may or may not be associated with large (> 200 km high) explosive plumes.

The explosion-dominated type is a really interesting style of eruption, their deposits of plumes covering several hundreds of kilometers ($\sim$ 1200 km) (33) in diameter and are of several colors, such as white, yellow, red, and/or gray material according to the type of S material. In Figure 3.5 it is possible to observe the plume deposits caused by Pele (red ring) and Pillan (black ring). Pillan, Tvashtar, Surt, and Thor are also classified as explosion-dominated volcano type.

The third case is the intra-patera eruption (54). These observations were seen at many volcanoes including Loki, Pele, Emakong, and Tupan, and are confined within paterae, or volcano-tectonic depressions similar to terrestrial calderas, ranging sizes from 2 to 202 km diameter. These eruptions may or may not have plume eruptions associated with them, and often erupt as lava lakes. Pele volcano is the one also known to produce explosion dominated eruptions (55, 49, 56). Nevertheless, many of the volcanoes observed on Io exhibit more than one eruption style and most of the

Figure 3.4 - Composition of three different resolutions of the image of the volcano
Prometheus (flow-dominated). The upper mosaic is a high-resolution frame,
the lower left image a medium-resolution frame, and the lower right mosaic a
low-resolution color frame. The upper and the lower left image were obtained
during Galileo's third close flyby of Io, on February 22, 2000. The lower right
mosaic were obtained on June 30, 1999.
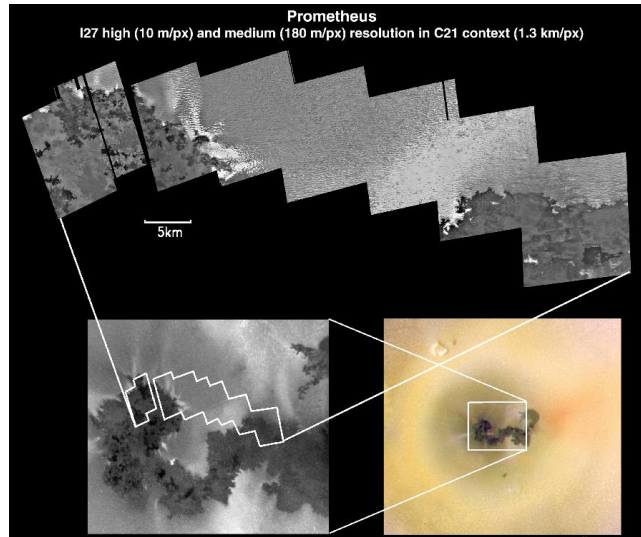
SOURCE: NASA/JPL/University of Arizona

active volcanoes show evidence of producing both explosive and effusive eruptions.
Figure 3.6 shows the intra-patera eruption

Loki is the largest and most powerful volcano on Io (45). It has been active since it
was discovered by the Voyager mission. More than two decades of ground-based ob-
servations (46, 57, 58) suggests that Loki eruptions are cyclic or quasi-cyclic, have a
200 km diameter horseshoe-shaped dark feature. Figure 3.6 shows a two temperature
map of the southern portion of Loki based on infrared-wavelength observations. Loki
is located approximately at $10°$ N and $310; \circ$ W on the Jupiter-facing hemisphere
(45). Loki's power output may reach 10^{13} W during periodic brightening (43). Its
periodicity is approximately 545 days. Loki accounts for almost 15 % of the moon's
heat flow (59). Its infrared brightness can be measured from the ground by using
Jupiter occultations of Io (60). Loki's temperature is greater than 900 k, which is
consistent with silicate lava (61).

Comparing Loki with Pele, Pele is fainter and due to its location it is not possible
to observe during Jupiter eclipses and occultations as Loki (41). Pele is 24 km in

Figure 3.5 - Image obtained by the SSI instrument of the Pillan volcano at several different resolutions. Pillan volcano has an explosion-dominated eruption style. At the bottom images, it is possible to observe the changes occurring in Pillan's surroundings. The large red ring was due to Pele's activity. These eruptions produce extensive flow fields that are rapidly set down over days to weeks.
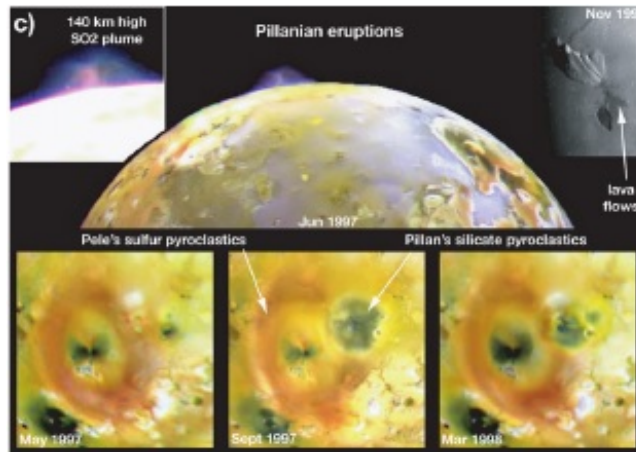
SOURCE: Keszthelyi et al. (2001) (53)

diameter and has a high-temperature thermal emission and plume deposits (62). Pele's plume is associated with the formation of an enormous red ring. The frequent changes in its red ring were strong indication of volcanic activity.

3.3 Plumes

More than 400 volcanic paterae dot the surface of Io (49) but only some of these volcanic centers have been seen to produce plumes. Most plumes are associated with new lava flows that explosively vaporize the existing superficial SO_2 ice, but the largest plumes vent sulfur-rich gases from the interior of Io. The color and opacity of dust plumes yields information on the dust grain size distributions and the dust deposition eruption rate (63).

Io's plumes may be observed when volatile vapors are expelled from volcanoes. They were first observed in 1979 (10) by Voyager 1, a 300 km high cloud. It was later identified as a plume generated by active volcanism. Plume's speed may reach up to 1 km/s (64). The study of plumes give important information about Io's interior composition, details of volcanic eruptions and also the effects it causes on Io's surface and atmosphere. The surface is in a constantly changing state due to

Figure 3.6 - High temperatures images from the western edge of the Loki volcano (Intra-patera). The lower right image show a hot temperature map and the upper right show hotter features. The image was taken on October 16, 2001.
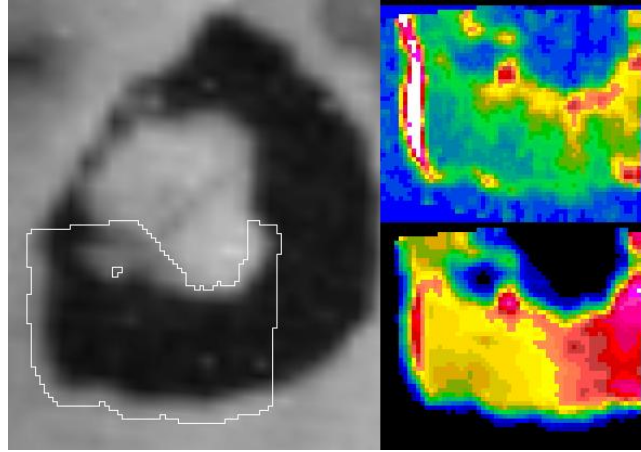
SOURCE: NASA/JPL

the fallout of the plumes, contributing to the rapid resurfacing, responsible for the burial of impact craters on Io's surface (64).

Plumes have been observed in different occasions, against the disk of Jupiter (65) or as shadows in the surface of Io. The confirmation of Pele's plume during Voyager approach on March 8, 1979 was the evidence needed for Io to be considered volcani-cally active. The Voyager spacecraft imaged a volcanic plume of 300 km height and 1,200 km wide. After this discovery other seven plumes were imaged by the Voyager spacecraft (66, 67, 37).

Io's volcanoes produce energetic plumes that drive the tenuous atmosphere, dis-tributing dust, neutrals and ions all over the Jovian system (48). Io offers the single opportunity to see volcanic processes that may have occurred on the early Earth (48). There are two principal distinct classes of plumes on Io. The first is observed as giant plumes that vent sulfur-rich gases from the interior of the moon and spray-paint the surface with enormous red rings. The second type are the smaller plumes, which are produced when the hot flows of silicate lava impinge on the volatile sur-face of SO_2 ice. The giant plumes are exemplified by the volcano Pele and they are a rarer type of plume. They are difficult to see in reflected light, exhale sulfur-rich gases from Io's interior and may reach heights of $\sim$ 400 km. The smaller plumes are exemplified by Prometheus and arise when hot silicate lavas flow over the icy

SO_2-rich substrate (63). Their typical heights are less than 100 km.

The New Horizons (NH) spacecraft on its way to Pluto returned images from Io's volcanoes between February and March of 2007. The NH flyby observed a 350 km high eruption at Tvashtar volcano (62° N and 122° W). The LEISA (Linear Etalon Imaging Spectral Array) instrument obtained spectral observations of Io and revealed a total of 35 hotspots, 11 of them seen more than once. Plumes seen for the first time by NH includes Zal and Kurdalagon (68).

Figure 3.7 - Images of gas and dust plumes from Zamama and Prometheus. The bottom images are enlargements of the plumes. It is possible to observe an excellent view of Zamama on the second image. The tall plumes are visible because they extend up into sunlight and their height are of $\sim$ 100 kilometers. On the third and fourth images it is possible to see other much fainter plumes.
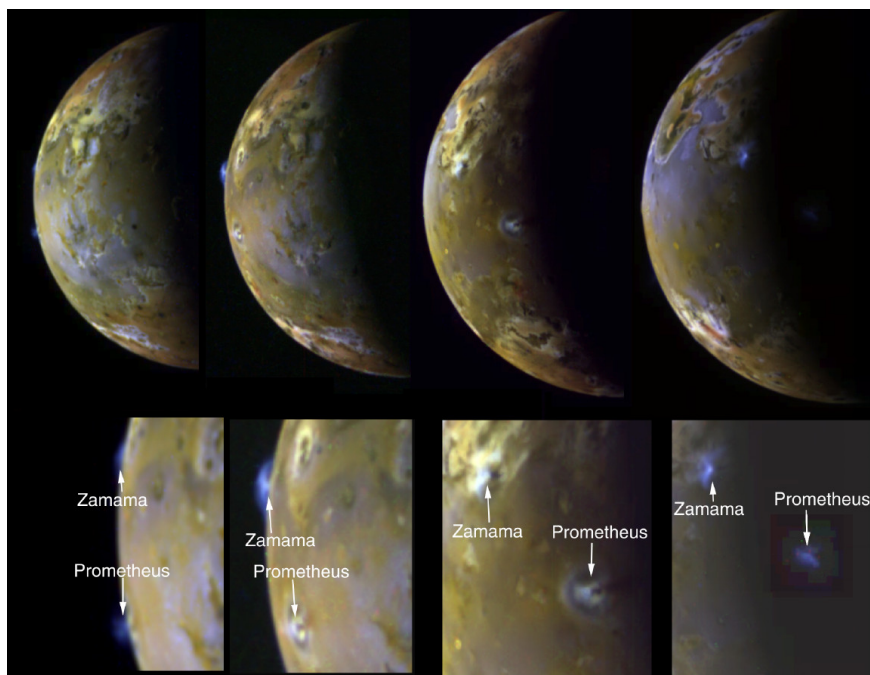
SOURCE: NASA/JPL/University of Arizona

3.4 Surface and Atmosphere

When Io's surface started to be studied one curious thing observed was the lack of impact craters on it. Although the impact fluxes are not precisely known, the resurfacing rate estimation to bury the craters as they are formed is 0.1 cm/yr. Io's surface consists of smooth plains broken by tectonic and erosional scarps, volcanic calderas, and rugged mountains, mostly of silicate composition. Many calderas are active and they are the sources of thermal emission (hotspots) and/or eruptive plumes. The sulfur dioxide, SO_2, is the only substance identified with confidence in the spectrum. It has numerous absorption bands in the UV and in the 1.9-4.1 microns.

SO_2 plays a role in the volcanic cycle on Io in very much the same way that water does on Earth. H_2O and CO_2, common volcanic volatiles on Earth, have not been detected on Io in significant concentrations (69, 70**??**). Io evolved a surface and a lithosphere rich in SO_2. Magma-SO_2 interactions drive much of Io's volcanic plume activity (50).

The equilibrium form of sulfur on Io is the common cyclo-octal molecule S_8. When heated or disrupted by charged particles, these rings can break up into short chains of sulfur atoms that are highly colored (50). At visible wavelengths it is possible to observe S_4 as it appears as a bright red.

After the Voyager mission, one important question remained: Io's surface composition and the nature of volcanism was made of sulfur or silicate? The intensive coloured surface was an indication of sulfur compounds. The sulfur and silicate compositions could be distinguished by their eruption temperatures. Sulfur's melting temperature is lower than basaltic silicates. Then, molten sulfur pools were expected to be in the range 400-600 k, while basalts over 1000 k (may reach as high as 1550 k) (33). Nevertheless, cooling silicates have temperatures in the same range as sulfur. That became a problem as measurements from Galileo showed that the temperatures observed were too high for sulfur. During the Galileo mission, volcanoes with higher temperatures were observed. Those results were calculated by the measurements of SSI and NIMS instruments, and the wavelength range to determine the temperatures between 1.1-5.1 microns (33). The eruption observed at Pillan hotspot in 1997 showed temperatures above 1800 k, which exceeds basaltic lava temperatures. The Pele hotspot was also observed at extremely high temperatures but in this case, due to the margin error of the measurements, it was not possible to distinguish between basaltic or ultramafic compositions (55, 71). Loki Patera, as being the most power-

ful volcano on Io, is observed quite easily from ground-based telescopes. When the eruptions are violent outbursts they are easily observed from the Earth. A violent eruption at Surt was seen using ground-based observations on February, 2001 (72). It is still not known if all lavas erupting on Io comes out at high temperatures or not, and what is causing these high temperatures.

Considering all these eruptions happening on Io's surface, it is not hard to accept that the atmosphere varies in longitude, latitude, and time. The atmosphere is directly supported both by volcanic injection of its primary constituent, SO_2, and frost sublimation (73). The large escape flux of different molecular and atomic species from the atmosphere populates the Jovian magnetosphere. Sodium is considered a good tracer for the more abundant species as the sulfur dioxide, and oxygen and sulfur dissociation products (74).

Models are the best way to understand how Io's atmosphere is formed and maintained. One of these models for Io's atmosphere consider that it is supplied locally by volcanic sources (75, 76). Galileo mission result's indicated a time-variable atmosphere with SO_2 gas concentrated near Io's equator (77). S, O, SO are expected from SO_2 photolysis and as primary products of high temperature volcanism (78, 79). More puzzling are the sources of Na, K and Cl that are also seen escaping from Io and populating the plasma torus and the extended neutral cloud (80).

4 Io Plasma Torus

The Io Plasma Torus (IPT) is a ring-shaped cloud of S^+, S^{++}, S^{+++}, O^+, O^{++}, and a small concentration of other ions. Material escaping from Io creates an environment in constant change. Its physics can only be understood by measuring and correlating the variations in its structure and properties such as density, temperature and state of motion (81). The conditions in the plasma torus are highly variable both spatially and temporally due to the dynamic environment at Io and in the magnetosphere (82). The plasma torus can be observed in the extreme ultraviolet (EUV) emission and in the optical wavelengths. The EUV emissions arise from interactions between torus superthermal ('hot') electrons and ions. Optical emissions come from interactions between thermal electrons and sulfur ions. The optical emission traces the densest part of the torus, the EUV traces the hottest part of the torus. It is most dense around Io's orbit (5.9 R_J). Therefore, from observations is it possible to obtain the temporal and spatial variability of the Io plasma torus. In this chapter, the plasma torus important processes are presented with the purpose to understand the optical observations of the sulfur ionized emission lines.

4.1 Introduction

Bigg (1964) (8) found that Io controls part of the radio emissions. Radio decametric emissions from Jupiter were discovered in 1954 (83) at 22.2 MHz. In situ measurements of Jupiter were obtained by the Pioneer 10 flyby in 1973. In 1974, Brown (84) observed neutral sodium emissions associated with Io using ground-based optical observations. And in 1976, Kupo et al. (11) discovered singly ionized sulfur (S^+) emission obtained by optical ground-based observations, coming from an inside region of Io's orbit (the inner cold torus), marking the discovery of the cold plasma torus and giving a new perspective of Io and the plasma surrounding it. Those discoveries gave a new perspective of the satellite-magnetosphere interactions. Three distinct regions are observed at the Io plasma torus: (i) the inner "'cold"' torus, between about 5 and 5.5 R_J, with a height of $0.1R_J$ off the equator; (ii) the ansa[1], between 5.6 and 5.8 R_J, and at a height of $\sim 0.6R_J$, where the [SII] density spikes; and (iii) the warm plasma torus which lies beyond the ansa

The ions observed at the Io plasma torus, sulfur (S) and oxygen (O), are derived from the breakdown of volcanic SO_2 (33). Besides the Io plasma torus it is observed the extended neutral cloud. The neutral cloud is directly connected with Io's escaping

---

[1]Ansa refers precisely to the strong glare from the ionized sulfur emissions S^+. The time of issue of the ansa is related to the temperature of the ions [SII]

processes of the atmosphere (84). Despite the sodium (Na^+) small abundance, it is easier to observe from the ground because of the sodium D lines are formed through a resonant transition at optical wavelengths. A good review of the processes forming the neutral cloud is seen at Wilson et al. (2002) (2). They show the neutralization of Na^+ by the pickup ions and also atmospheric sputtering. It is from the continuous ionization of the neutral cloud that the 'ring' of plasma is created around Jupiter, close to Io's orbit and moving around Jupiter about the co-rotation speed. Figure 4.1 explains the processes of Io's atmospheric escape, while Table 4.1 gives an idea of the timescales for escaping materials and the processes involved. The knowledge of timescales are important when trying to understand how long does it take for the materials to escape from Io and influence the sodium cloud and the plasma torus.

Figure 4.1 - Image of the Io's sodium cloud represented on three spatial scales, from 1000 R_J to 9 R_{Io}, left panel. In (d) is shown schematically the three atmospheric escape processes known.
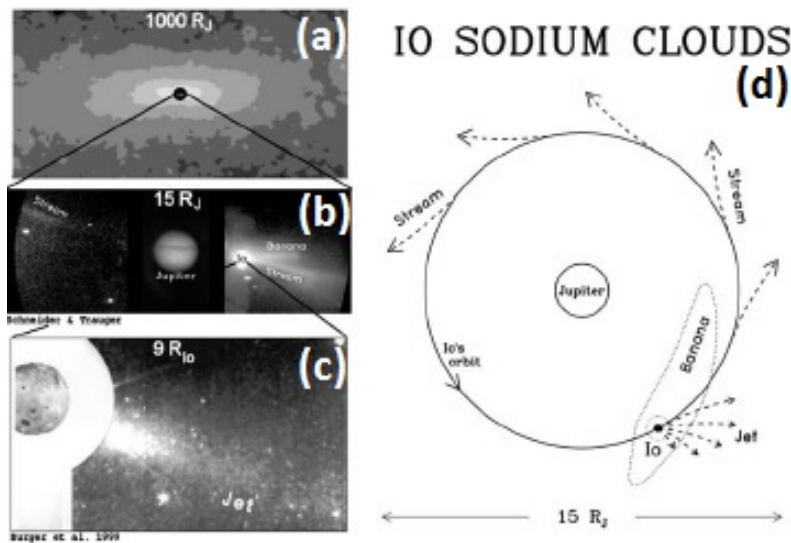
SOURCE: Lopes and Spencer (2007) (3)

At the torus, it is estimated that the ions remain there up to a time relative to 100 revolutions of Jupiter, which means that every rotation of the torus through the neutral cloud adds only 1 % of new plasma. The interaction of Io with the plasma torus is so strong that it is possible to observe auroral emissions at Jupiter in the vicinity of the magnetic footprint of Io (85).

Table 4.1 - Characteristic timescales for escaping materials. These are approximate timescales applied to the torus (n = 2000 electrons/cm^3; T_e. Adapted from Lopes and Williams (2005) (33).

Process	Example	Lifetime
Electron impact ionization	$O + e^- \rightarrow O^+$	~ 100 hr
	$S + e^- \rightarrow S^+$	~ 10 hr
	$Na + e^- \rightarrow Na^+$	~ 4 hr
Charge exchange	$O + O^+ \rightarrow O^+ + O^*$	~ 50 hr
Electron impact dissociation	$SO_2 + e^- \rightarrow SO + O$	~ 4 hr
Transport time to Hill sphere (6 R_{Io})	3 km/s (average)	~ 1 hr
transport time across cloud (6 R_J)	3 km/s (initial)	~ 20 hr

4.2 Io plasma torus variability

As mentioned before, Kupo, Mekler and Eviatar (11) were the first to identify the individual forbidden emission lines of sulfur ([SII], λ 6731 Å , 6716 Å). Since then a number of ground-based observations were obtained (86, 87, 88, 89, 90, 25, 91, 26, 92), especially because the of observed variability at the plasma torus. The plasma torus variability is still not well understand, and the main reason is the lack of continuous observations. From the Io Plasma Torus (IPT) it is possible to observe both sides of the torus simultaneously and monitor the positions of maximum brightness relative to the center of Jupiter. Another effect possible to obtain during observations is the brightness asymmetry produced by the modified electron density and temperature. Figure 4.2 shows the observation which occurred on September 18, 1997. It is possible to see the both ansae sides (dawn and dusk). The IPT variability is believed to be related to Io's volcanic activity as it does not occur steadily (28).

Figure 4.2 - Image observed at the McMath-Pierce Solar Telescope on September 18, 1997. It is one of the images reduced and analyzed during this thesis. Both dawn and dusk ansae are observed.
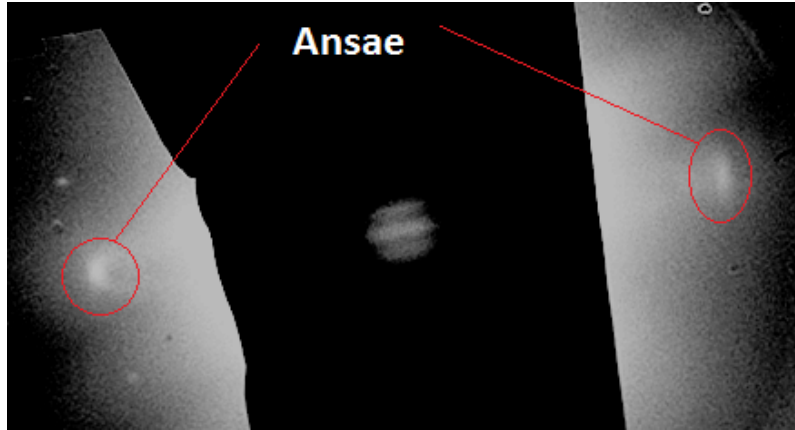
SOURCE: Author

Another important characteristic is the fact that Jupiter's magnetic dipole moment is not aligned with its rotation axis (Figure 4.3). It is tilted by $\sim 9.6°$ towards longitude $202°$ in the northern hemisphere (System III longitude). Jupiter's magnetic field confines the plasma torus toward the equator, not by the strength of the magnetic mirror, but by centrifugal forces[2] (33), causing the plasma torus to tilt, mainly due to inclination of the magnetic field ($10°$ inclination from Jupiter's rotation axis) of Jupiter, but also by the planet rapid rotation (10 hours). The plasma torus has a density in the vicinity of Io's orbit of ~ 1500 $ions/cm^3$ and 2000 $electrons/cm^3$ and presents a width of ~ 2 Jupiter radii ($\sim 143\ 000$ km) (93, 94). It is Jupiter's internal field which controls Io and has an strength of ~ 2000 nT. Because of the dipole tilt and its fast rotation, a time-varying magnetic flux induces electric currents in the conducting layers of the Galilean moons (which creates their induced magnetic field). The centrifugal equator is close but not identical to the magnetic equator, it is tilted ~ 7 degrees relative to the orbital plane of Io. The torus extends along the field lines to ± 1 R_{Io} from the centrifugal equator (95).

The magnetic equator is the plane that is perpendicular to the centered dipole and passes through Jupiter's center. Latitude is measured positive northward. Because the Io plasma torus is important, and because it consists principally of relatively

---

[2]The magnetic mirror is the basis of plasma confinement schemes. Charged particles can be reflected by the magnetic mirror and travel back and forth in the space between them, becoming entrapped

heavy ions with low energies, one other "equator" is necessary to fully describe the Jovian magnetosphere, and that is the "centrifugal equator."

Figure 4.3 - Jovian dipole equators where M is the dipole moment and Ω is the angular velocity. The spin equator is a plane that passes through the center of the planet, perpendicular to the spin axis. The magnetic equator is the surface defined by the locus of points of minimum magnetic field strength along a magnetic line of force from M. This point is located where r reaches its maximum value. The centrifugal equator is the surface defined by the locus of points that are the maximum distance (or where ρ is a maximum) from the spin axis for given lines of force.
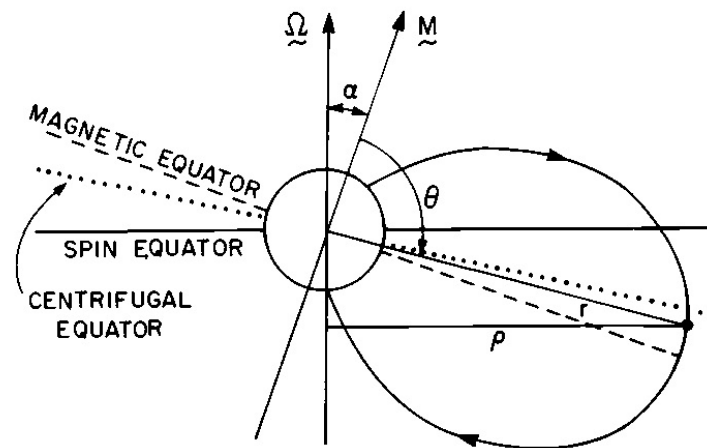
SOURCE: Dessler (1983) [20]

4.3 Dawn-dusk (east-west) asymmetry

The dawn-dusk asymmetry is an observed effect in which the dusk ansa side seems to be brighter than the dawn ansa side. Ip and Goertz (1983) (96), and Barbosa and Kivelson (1983) (97) proposed the existence of an electric field extending from dawn (east) to dusk (west) across the Jovian magnetosphere. Such a field might be created by the anti-sunward flow of plasma down to the magnetotail. This electric field would result in higher temperatures on the dusk side via adiabatic compression of the plasma, and a radial shift in the location of the torus by a few tenths of an R_J in the direction of the dawn ansa. The dawn-dusk position of the IPT ansa gives information about the magnitude and orientation of the IPT co-rotational electric field (97, 98, 99). The height of the ansa emission is related to the temperature of the [SII] ions parallel to Jupiter's magnetic field. The time sequence of the brightness values of each ansa can be used to derive the Systems III and IV periods.

The dawn-dusk position of the ansa of the IPT provides information of the magnitude and orientation of the co-rotacional electric field in the plasma torus, $\vec{\epsilon}$ (97, 99). The height of the emission of the ansa is linked to the parallel component of the magnetic field of Jupiter. If there is a change in the delivery rate of volcanic material of Io for the torus, a variation in the radial distribution of the plasma is observed. Consequently, the radial [SII] emission profiles reflect these variations (28). Then, their differences seem to occur due to the temperature and density of plasma which decreases rapidly with increasing radial distance. This feature shows that the ions' diffusion from Io's internal region moving against the electric potential is slow.

The input plasma diffusion rate is slow and the plasma has enough time to cool by radiation. As the plasma cools, it collapses into the centrifugal equator, contributing to the increase in local density. This process leads to state transition of temperature and ionization in the region between the cold torus (diffusion inward) and hot torus region (diffusion outward). The diffusion inward and outward of the plasma torus is better explained with the sketch in Figure 4.4. The width of the transition zone between the hot and cold regions of the torus is extremely narrow, 0.05 R_J, which seems to be a permanent feature of the torus. The diffusion equation is a partial differential equation that describes the density fluctuations in different materials:

$$\frac{\partial u(\overline{r},t)}{\partial t} = \nabla.(D(u(\overline{r},t),r)\nabla u(\overline{r},t)) \tag{4.1}$$

where $u(\overline{r},t)$ is the density of the diffusion material r = (x, y, z) and time t;

$D(u(\bar{r}, t), r)$ indicates the collective diffusion coefficient for density of u in r.

Figure 4.4 - Sketch of the coupling between the torus, magnetosphere, and ionosphere, and the processes involved at the plasma torus region.
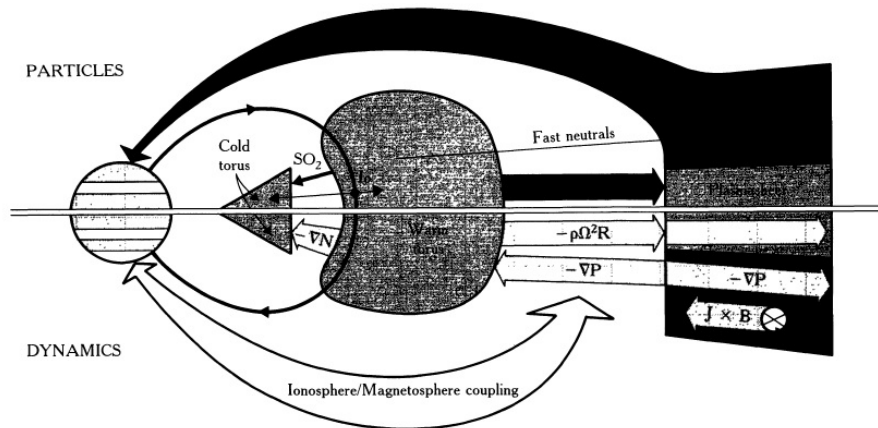
SOURCE: Bagenal (1989) (95)

The hot torus region emits a radiative energy flow in the EUV (Extreme UltraViolet) from the ionized sulfur and oxygen. This is the main reason for the large difference in temperature between ions and electrons.

5 Methodology

In this chapter the methods and techniques used for the observations and the image reduction are presented. Two types of images were used, one from ground-based observations at the McMath-Pierce Solar Telescope (MMPST) and the other from the spacecraft Galileo, using the Near-Infrared Mapping Spectrometer (NIMS) instrument. The technique used to reduce the images from the NIMS instrument are also presented despite the fact that the results won't be used in this thesis. More details will be given throughout the chapter.

5.1 Introduction

When an astronomical object is planned to be observed from the ground, some procedures need to be taken into account. Earth's atmosphere absorbs electromagnetic radiation at most infrared (IR), ultraviolet (UV), X-rays and gamma-rays, leaving an atmospheric transparency window at the radio and visible wavelengths. The near-infrared (NIR) range is also possible to be observed from ground-based telescopes, under certain conditions. The ground-based observations performed at the McMath-Pierce Solar Telescope (MMPST) were at the visible range of the spectrum. While the data from the NIMS instrument, as it was obtained from a spacecraft has no problem concerning Earth's atmosphere.

Nowadays, Earth's atmosphere is quite well known and studied. The knowledge of the atmosphere is an important tool to make sure the data obtained is from the target (in this case, Jupiter). The Sun's radiation reaching the Earth is absorbed and emitted by the atmosphere. In Figure 5.1 the absorption lines at the visible spectrum range are shown. The data used in this thesis were observed at the specific emission line of ionized sulfur, the 6731 Å line. In Figure 5.1 it is possible to observe that there is no significant signature at the 6731 Å line in Earth's atmosphere absorption lines. At the top of the figure, the range of the visible spectrum is shown. The line observed and used in this thesis is located at the red range of the visible spectrum.

Figure 5.1 - Spectrum of the absorption lines from Earth's atmosphere. It is noted that from H_α at 6562.81 Å to O_2 at 6860 Å the atmospheric absorption of the Sun is relatively smooth. It won't interfere with the [SII] 6731 Å observation lines.
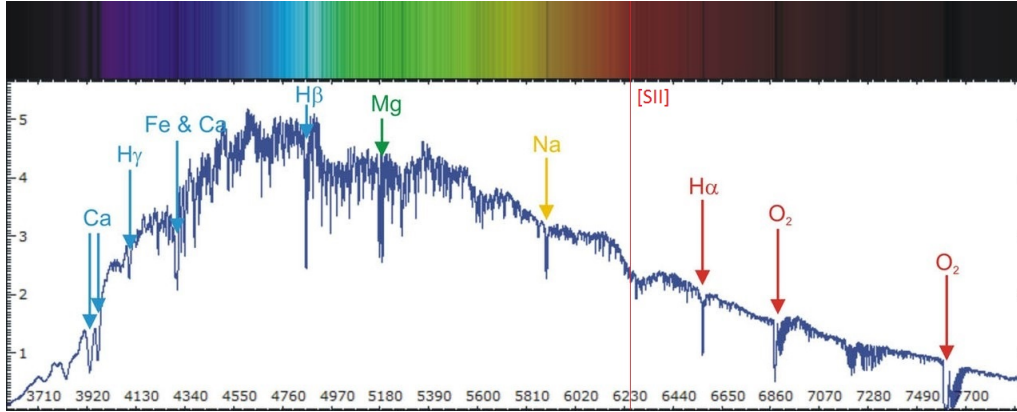
In Figure 5.2, the spectrum of the night-sky emission lines in the Earth's atmosphere is observed. As it is possible to see, there is no important emission in the range observed (6731 Å). It is safe to say the Earth's atmosphere will not be a problem for the observations. Concerning the space, for the light traveling from Jupiter to Earth, it is pretty safe to say that the vacuum of space won't be absorbing anything significant.

Figure 5.2 - Night-sky emission lines from Earth's atmosphere from 6200 to 7500 Å range.
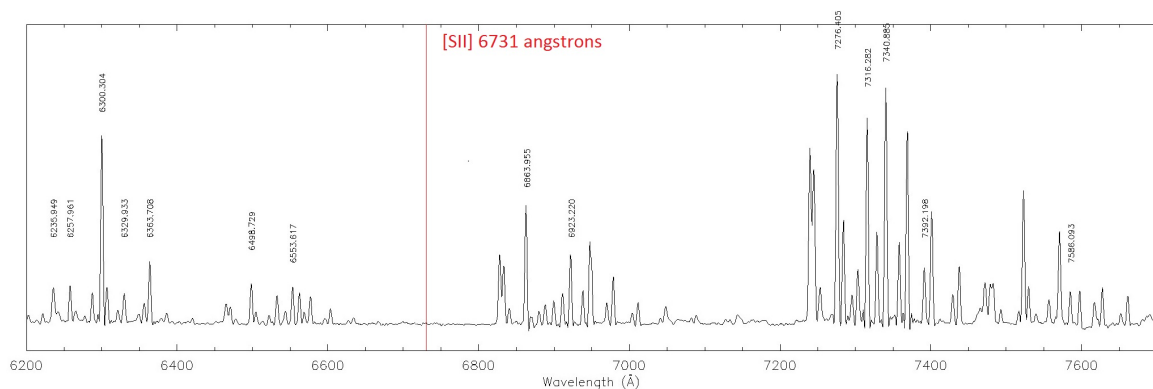
The previous Figures (5.1 and 5.2) showed that Earth's atmosphere has no considerable emission or absorption line at the 6731 Å . The next step is to interpret and decode the light received from the plasma torus in terms of the physical parameters. Figure 5.3 shows the geometrical relationship between the emission layer and the remote observation of light. The formalism here expressed is based in the theory presented at Dessler (1983) (100). The telescope collecting area, A (cm^2), and the field of view, Ω (sr), observes the emitting layer that is differentially thin and oriented perpendicular to the line of sight. The surface brightness is dJ_λ (photons/cm^2/sr/s), the differential volume is dr, the number density of emitter is n (cm^{-1}) and the average number of photons emitted in the line by each ion per second is ϵ_λ, the unit emission rate.

Figure 5.3 - The sketch shows the geometry for remote observations of emitting regions. The count rate for photons at the telescope relates the observed brightness to the physical process of emission along the line of sight.
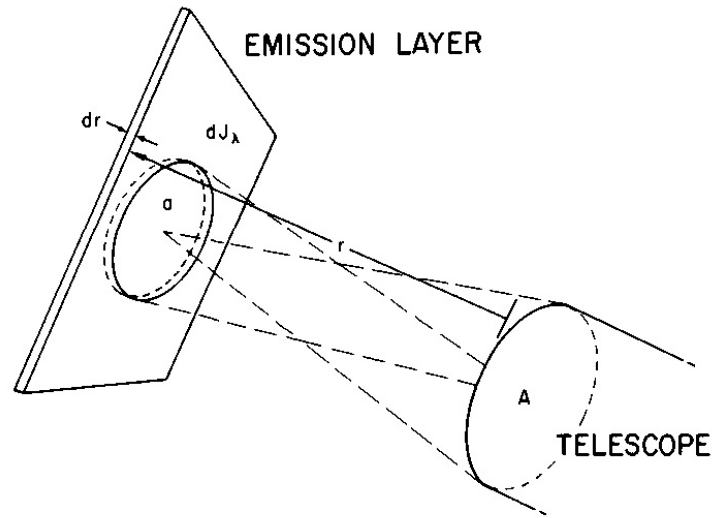
$$\text{COUNT RATE} = dJ_\lambda \cdot A \cdot \frac{a}{r^2} = \underbrace{n_i \cdot a\, dr}_{} \cdot \underbrace{n_e \alpha_\lambda \cdot \frac{A}{4\pi r^2}}_{}$$

SOURCE: Dessler (1983) (20)

The unit instrumental efficiency or the photon count rate is given by:

$$CountRate(s^{-1}) = dJ_\lambda A\Omega = dJ_\lambda A \frac{a}{r^2} \tag{5.1}$$

Considering an isotropic emission, the photon count rate at the telescope is

$$CountRate(s^{-1}) = nadr\epsilon_\lambda \frac{A}{4\pi r^2} \tag{5.2}$$

which combining with (5.1) gives

$$4\pi dJ_\lambda = n\epsilon_\lambda dr \tag{5.3}$$

By integrating along the line of sight through the source region, we obtain:

$$4\pi dJ_\lambda = \int n(r)\epsilon_\lambda(r)dr \tag{5.4}$$

The left side of Equation (5.4) is the observed quantity, the apparent emission rate. In the case J_λ is expressed in units of 10^6 photon/cm^2/sr/s, then $4\pi J_\lambda$ is in Rayleighs. The right side of the equation (5.4) is the sum along the line of sight of the number density of emitters weighted by their propensity to emit (20). The unit emission rate factor responds to the radiation or charged particle environment of the atoms or ions. For sulfur and oxygen atoms and ions, electrons populate upper atomic levels by means of inelastic collisions, and the atom or ion decays to the ground state by the emission of one or more photons. In this case, ϵ_λ is the product of the electron number density n_e, and a rate coefficient $\alpha_\lambda(T_e, n_e)$ which is a function not only of electron temperature but also of electron number density.

The red doublet of singlet ionized sulfur (6716 Å , 6731 Å) is an example of a case with $\alpha_{\lambda i}$, effectively temperature independent (101), permitting the electron density to be determined from the line ratio. Equations (5.1) to (5.4) are important tools for inverting photometric observations of line emission in terms of the underlying composition and physical state. To express the brightness emission of the light received from the Io torus, it was used the photometric unit, Rayleigh (102).

Two types of ionic emissions have been observed from the plasma torus, both of which are excited by collisions with electrons. The forbidden lines at wavelengths between 3000 Å and 10,000 Å arise from transitions between terms in the p^2 and

p^3 ground electron configurations of sulfur and oxygen. The more energetic lines may only be observed by spacecraft and are due to allowed transitions that occur at wavelengths ($\lambda < 1800$ Å) too short for resonant scattering of sunlight to be an important effect.

The observations presented in this thesis were focused to obtain the brightness emitted by the ionized sulfur observed at the Io plasma torus. Ground-based observations imply that the spatial distribution of SII inside Io's orbit is generally wedge-shaped. The wedge-shaped is here called as ansa and is situated on or near the centrifugal equator (103). The apex of the ansa as observed from the ground corresponds to the maximum SII density (87, 21). The sulfur is sputtered off the surface of Io and come off as a neutral atom (104). Consequently, the amount of ionized sulfur must be associated with a significant increase in the ionization rate (11). Once the sulfur is ionized, it will be captured by the magnetic field of Jupiter within a gyroperiod and will then corotate with the planet. Figure 5.4 presents the Grotrian diagram where the transitions for the SII emission lines are described. The transition array consists the jumps between two configurations, for instance, 3s - 4p. A multiplet includes all transitions between two terms: $3s^2P$ - $4p^2S°$. A line arises from a transition between two levels: $3s^2P_{3/2}$ - $4p^2S°_{1/2}$. It is usual to write forbidden transitions with a bracket, [ ].

In the optical emission from the torus in the red [SII] lines, the first excited levels of the ion $^2D°_{3/2}$ (1.842 eV), $^2D°_{5/2}$ (1.846 eV), $^2P°_{1/2}$ (3.042 eV), and $^2P°_{3/2}$ (3.047 eV) are connected to the ground state $^2S°_{3/2}$ only by electric quadrupole and magnetic dipole matrix elements (Figure 5.4). These upper levels are therefore populated only by electron collisions, not by photon absorption. Slow decay by photon emission occurs from the $^2D°_{3/2}$ and $^2D°_{5/2}$ levels with lifetimes 6×10^2 s (6731 Å) and 2×10^3 s (6716 Å), respectively. The $^2P°_{1/2}$, level radiative lifetime is 1.4 s leading to lines at 4068.6, 10320.5, and 10286.7 Å in the ratio 1:0.62:0.51.

Figure 5.4 - Grotrian diagram of SII. Levels with the same term are shown vertically. The electron configuration and J values (in order of increasing energy) are shown for each level.

S II

^{4}P

$3p^23d\ (\frac{5}{2},\frac{3}{2},\frac{1}{2})$

$3p^24s\ (\frac{1}{2},\frac{3}{2},\frac{5}{2})$

765

910

$3s3p^4\ (\frac{5}{2},\frac{3}{2},\frac{1}{2})$

1256

^{2}P^o

$3p^3(\frac{1}{2},\frac{3}{2})$

[10325]

[4069]

[4076]

^{2}D^o

$3p^3(\frac{3}{2},\frac{5}{2})$

[6716]

[6731]

$3p^3(\frac{3}{2})$

^{4}S^o

10^4K 10^4cm^{-1} eV
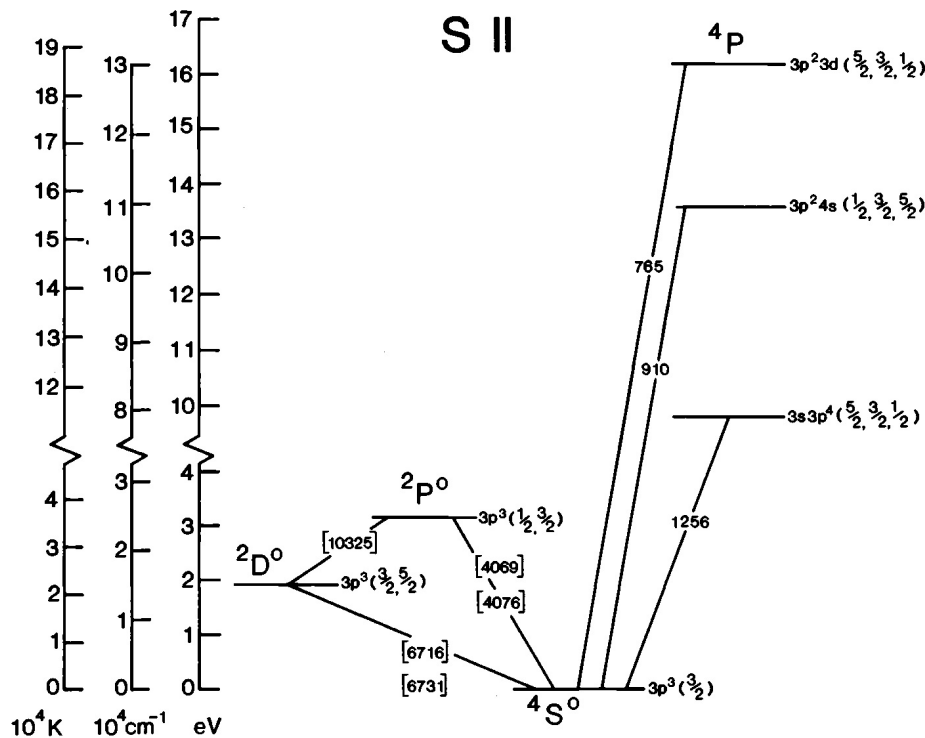
SOURCE: Dessler (1983 - Chapter 6) (100)

5.2   McMath-Pierce Solar Telescope

The McMath-Pierce Solar Telescope (Figure 5.5) was built in 1962 and it is located at the Kitt Peak National Observatory (KPNO), about 100 km of Tucson, Arizona. KPNO is part of the National Optical Astronomy Observatory (NOAO) where 22 optical telescopes and two radio telescopes are located. The Solar Telescope (*nsokp.nso.edu/mp*) is a 1.6 m f/54 reflecting telescope which contains a heliostat at the top of its main tower. There are three major telescopes operating: the Main, the West-auxiliary and the East-auxiliary. The East and West-auxiliary operate independently of the main telescope. These two auxiliary telescopes both have a 0.91-meter heliostat which are located beside the main heliostat. These auxiliary telescopes have a slightly shorter focal length and f-numbers of 50 and 44, respectively. The resolution of the auxiliary telescopes are 5.11 arcsec/mm (West) and 5.75 arcsec/mm (East) (105). All telescopes feed their beams through the op-

tical tunnel of the facility. As in all observatories, the MMPST also has its own weather station. These stations are quite important as they give information on atmospheric conditions at all times. All the images used in this thesis were obtained at the West-auxiliary telescope.

Figure 5.5 - (A): McMath-Pierce Solar Telescope located at Kitt Peak, United States; (B): View from the visitor center from part of the other telescopes existing at Kitt Peak. Both pictures were taken during the observation run of 2013.
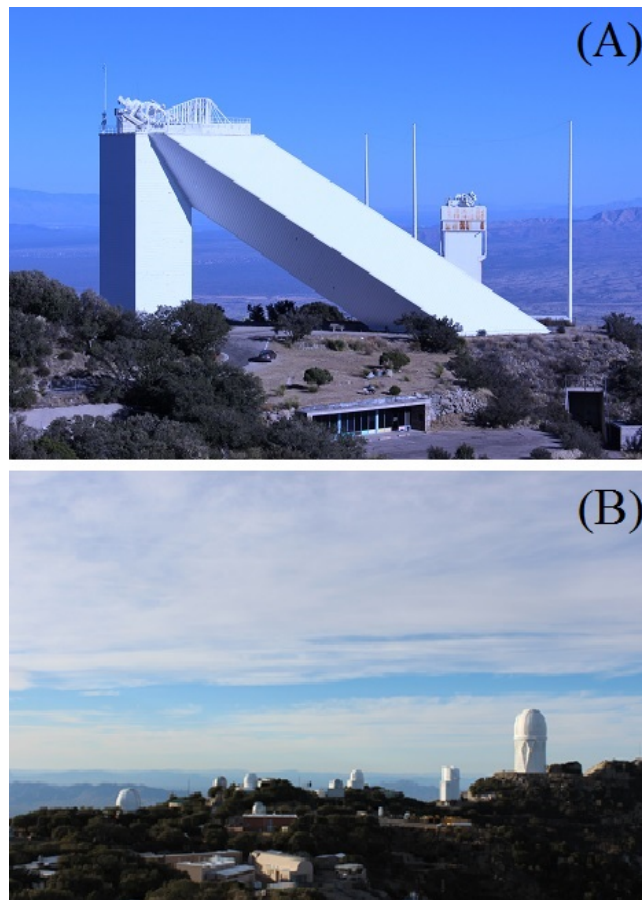
SOURCE: Author

The 1997-2001, 2003, 2007, and 2008 years of data of the [SII] 6731 Å emission line observations were granted by Dr. Jeffrey P. Morgenthaler (Planetary Science Institute - PSI) through a collaboration established during this thesis. These observations are part of his group's collection and had never been reduced or published. In 2013 I had the opportunity to participate in an observation run with Dr. Morgenthaler at the MMPST. The 2013 observation run used

the same instruments and techniques performed previously by the group. Previous works from the group may be seen in (26, 92). The observation of which I was part occurred in the end of the 2013 and lasted two weeks. During that period, another group was also at the solar telescope observing the comet ISON ($www.nasa.gov/mission-pages/asteroids/comet-ison/index.html$) whereof Dr. Morgenthaler was in charge. During those two weeks, I had the chance to learn about the instrumentation and the telescope during the observations. Also to interact with researchers from other institutes and make part of two different observations, one during the day, observing comet ISON, and the other during the night, observing Jupiter. The IPT observations, however, did not come as expected. During the first week, most of the time was dedicated to make the west-auxiliary telescope ready to observe. The time was used to fix the telescope, test the instruments and, of course, to learn. The observations were possible during the second week when the MMPST was finally ready to observe. But most of the second week the weather didn't help and most of the nights were cloudy, preventing the possibility of observations. The images observed in 2013 were not good to be used in our analysis. They were used to test the methods developed for the image reductions. All routines and calculations necessary were developed by me with Dr. Morgenthaler help. The amount of data from 1997 to 2008 has approximately 1000 frames. During the 2013 observational run about $\sim$ 15 science images (Jupiter's images) in total were obtained. The histogram (Figure 5.6) presents the total number of frames observed per year. The year of 1997 (data reduced in this thesis) is highlighted in magenta and the year of 2013 (observation run I participated) in blue.

Figure 5.6 - Histogram with the amount of science images observed per year, from 1997 until 2013. There were gaps in between.
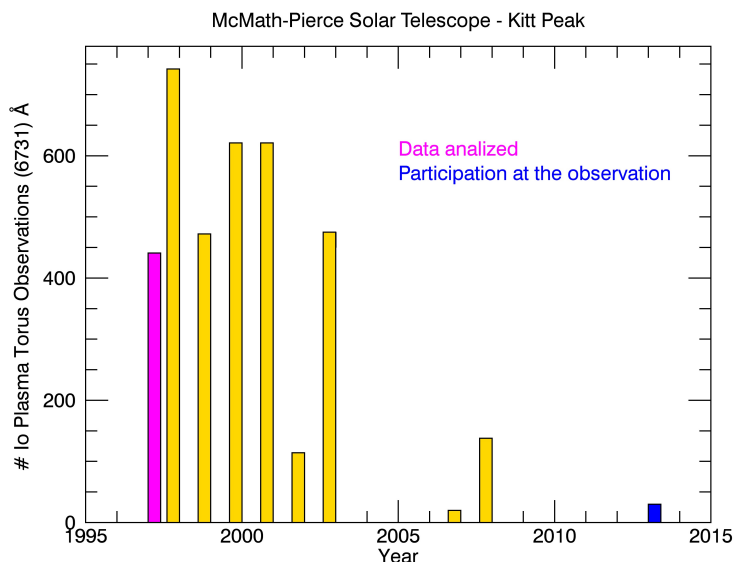
SOURCE: Author

5.2.1 Data

As presented at the histogram (Figure 5.6) it is possible to see that the period of observation available for reduction is of almost a decade. Nevertheless, when I started to work with the data, I realized that there was some important information of the images that were not available. It delayed the process of reduction but that time was used to go through all the thousand images (or frames) and check for the quality and state of each image. As it is going to be presented throughout this chapter, other problems have been found which prevented the reduction of all years but 1997. Data from the MMPST presented in this thesis is of 1997 and a total of 276 science (Jupiter) images. Including the calibration, bias and flat field images, a total of approximately 400 frames were analyzed. From the MMPST data, sulfur ionized ([SII]) emission lines from the Io Plasma Torus (IPT) were observed. From the frames it is possible to see the east (dawn) and west (dusk) ansae of the IPT. A total of 154 frames from the east ansa and 121 frames from the west ansa were analyzed. These data were obtained during 14 days in September and during 8 days in October of 1997.

5.3 Image reduction

After considering the context for the light received from the plasma torus and Earth's atmosphere, the next step was to test and choose the best filter to use during the observations. To observe the plasma torus, the 6731 Å filter was used. A Neutral Density (ND) filter was used to attenuate the brightness of Jupiter (Figure 5.7). The ND filter is a square filter of 50.8 x 50.8 mm, with optical density 3.0 ± 0.15, NE230B model, manufactured by Thor Labs. Its objective is to reduce the intensity in all wavelengths. To fit the ND filter to the holder, it had to be broken in half, leaving an approximately size of 25 mm × 50.8 mm. During the observation nights the sequence of the filters followed the given order: (i) 6731/12 Å ; (ii) Clear (no filter); and (iii) 9075/20 Å to be used as an off band. A filter transmission is given in percent over a spectral interval. This term is commonly used to specify transmission characteristics of long-wavelength pass, short-wavelength pass and wide-bandpass filters. In other words, the filter profile is a graphic that reads the fractional transmission versus wavelength. The 6731 Å filter profile used is presented in Figure 5.8.

Figure 5.7 - Image of the neutral density filter obtained during the observation run in 2013. In the lower image is shown the filter at the support used. The top picture is part of the imager used during the observations and the neutral density filter placed at the focus of the telescope.

SOURCE: Author

48

Figure 5.8 - Information of the filter transmission curve used during 2013 observation run. The FWHM spans 6724.30 Å to 6736.26 Å 90 % spans 6727.49 Å to 6732.33.
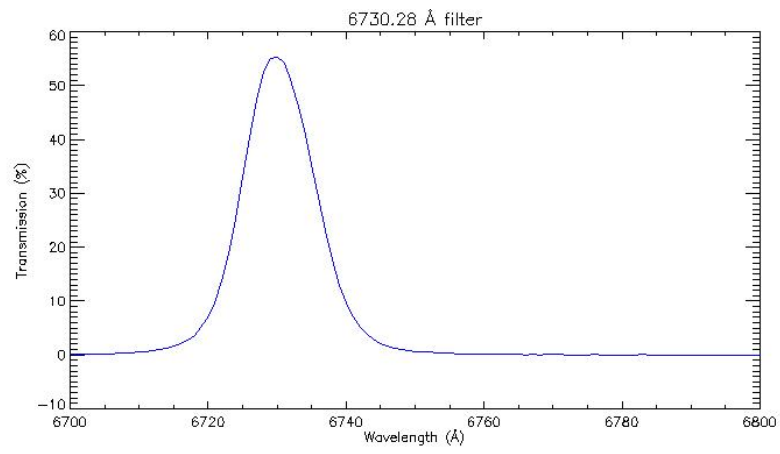
SOURCE: Author

The filters were coupled to the CCD (Coupled-Charged Device) camera and deployed in a turntable, making the change easier during the night. After testing all the filters available (9 filters were tested in total), we used the one that gave the best transmission response. Filters come with all the specifications and tests from the manufacturer but tests must be done before the start of the observation run. A methodology was developed and the tests were taken on the images of the 2013 observation. From the final result a flowchart with the main ideas was created (Figure 5.9) and then applied at the 1997 images. As it may be seen at the flowchart, the process was divided in four steps: (1) Pre-processing, (2) Processing, (3) Data reduction, and (4) Data analysis. Due to a storage problem, the images were saved at the pmi format which main purpose was only to reduce the size of the files. Then the main step was to convert from pmi to fits format. The routine developed use the information in the text header and a matrix containing the data in the binary portion to convert to the fits format again. With the header and matrix (image) in hand the basic image reduction could then be applied, such as bias calibration, flatfield and background reduction. This part of the pre-processing is to have all the reductions necessary to apply to the science images (or the images of Jupiter) and get it to the point where the scientific information could be extracted. That step was called as image processing. Data reduction was the part where the brightness was extracted from each ansa (dawn and dusk), as it will be show later on. Finally reaching the data analysis where it was possible to evaluate the results obtained and see if it was possible to obtain the objectives proposed.

Figure 5.9 - Flowchart of the main steps taken to reduce the ionized sulfur images observed at Kitt peak.
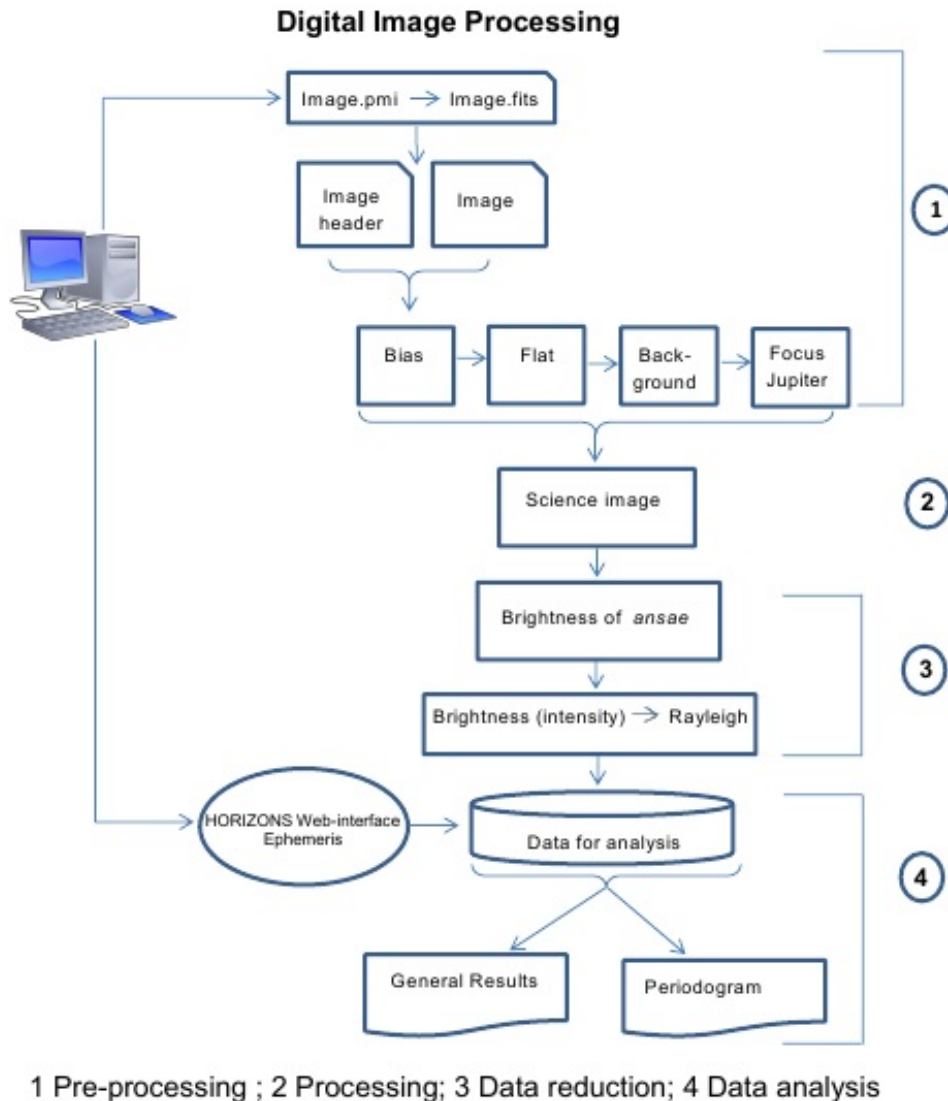
SOURCE: Author

5.3.1 Raw images

Image basic calibration is a necessary procedure to correct errors from the CCD, electronics and systematic errors of the telescope. The programming language used was IDL (Interactive Data language). IDL is a vectorized, numerical, and interactive language, used for data analysis. The images were stored in FITS format (Flexible

51

Image Transport System) (106). Those are image files developed to store, transmit and manipulate scientific images and meta-data associated with it. These types of images are quite common in astronomical observations. They can save information such as history of the data, coordinates, binary data format and free-form comments.

In the early years of astronomical observation, the photographic plate was the state of art recording images. It was used until 1990s. After, they were replaced by high-quality Charged-Coupled Device (CCD) image. The CCD deals with the motion of electrical charges, capturing images by its photon-active region. A CCD quality is evaluated by its Quantum Efficiency (QE). The QE is giving by its ability to absorb photons in the photosensitive silicon region, where photons are converted into electron-hole pairs, then to a pixel. The QE of modern CCDs is typically 80 % for visual photons (wavelengths between $\lambda \sim 400$ and 700 nm). The electrons in a pixel are converted into counts or ADUs (Analogue-to-Digital conversion Units). The conversion of units from pixel to ADU is found in Appendix 1.

Figure 5.10 - Quantum Efficiency performance at $+25°C$ of front-illuminated (FI), back-illuminated visible-optimized (BV), UV-enhanced silicon back-illuminated ('BU2') and back-illuminated deep-depletion CCDs with NIR AR-coating (BR-DD) and broadband dual AR-coating (BEX2-DD).
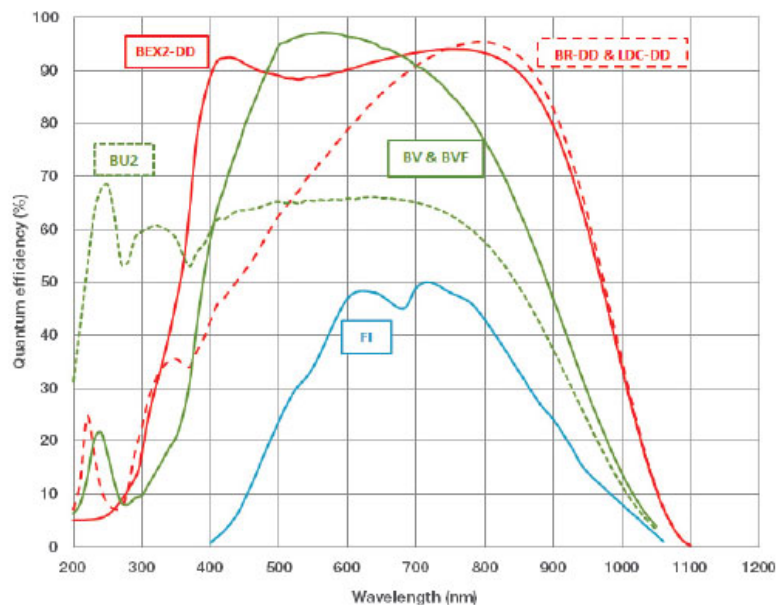
SOURCE: www.andor.com

Basic calibration of optical astronomical images normally deals with bias subtraction, which subtracts the chip bias signal, a constant signal in all images; flatfield correction, which compensates for pixel-to-pixel sensitivity variations; and dark counts (caused by thermal motions). These images are taken before the start or the end of the observation. The camera used during the observations is quite efficient preventing thermal counts in science images.

Dark current is a noise inherent to CCDs. A way to deal with this problem is to use a cooling system, which is the best way to avoid the addition of heat to the electronics during observations. The most commonly used cooling systems are air, liquid coolant, liquid nitrogen (LN_2) and thermoelectric (TE). The CCD camera model used during observations was an ANDOR SOLIS iKon-M, 512x512 pixels. And the method used to keep the camera cold was water cooling. The water flows through the heat sink, removing the heat very efficiently. The CCD temperature will be dependent only on the water and not on the room temperature. According to the manufacturer, using a water cooling system in which the water is kept at 10° the detector will be cooled to $-100°$ C. And it was good enough to not ass dark current to the data. The cooling system used was created by Dr. Morgenthaler's Winsonsin group and may be seen in Figure 5.11, along with the imager.

The use of multiple exposures is a good method to get rid of noise (the noise is inversely proportional to the square root of the total number of counts, and combining images results in more counts) and outliers (cosmic rays, stars in sky flats). The best way to do the basic image calibration is to combine it into a set of master images (masterbias, masterflats). By doing this one can remove cosmic ray hits that might be contaminating the images. Cosmic rays are quite easy to identify in the science images as they saturate only one or two pixels and are always positive. Astronomical objects will never do this.

Several bias images were taken in each night of observation. Sometimes bias images are called zero images because they are taken for zero seconds and without opening the camera shutter. Even though the exposure time was zero seconds and the shutter was never opened, it is still seen as a non-zero count level. These counts are intrinsic to the CCD. The idea is to combine the frames collectively to make a generalized bias and extract additional counts that are not real in the science images. The IDL routine created combined all bias frames into a single image making a stack of images by using the median function. That new single image is called masterbias image and then is subtracted from all flatfield and science images. Bias images vary from chip

Figure 5.11 - Instrument used during all the years of observations performed at McMath-Pierce Solar Telescope.
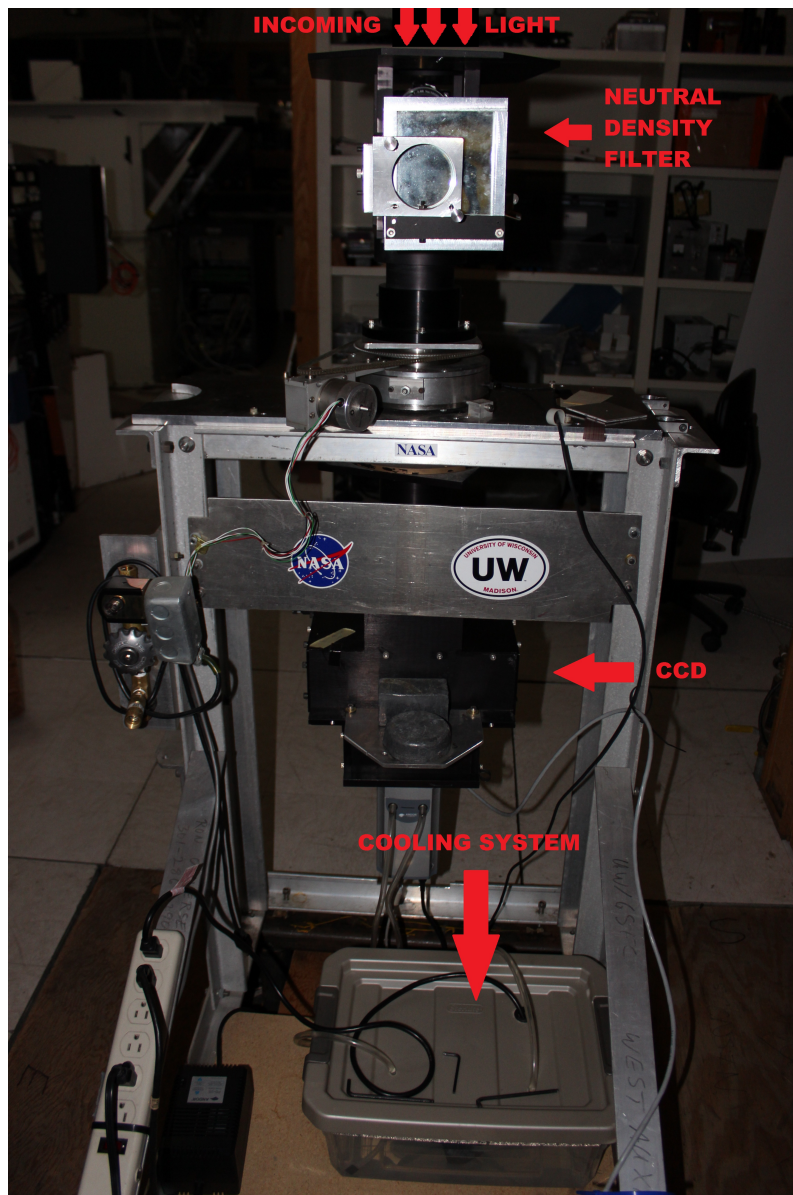
SOURCE: Author

to chip, and even from night to night. Typically the bias level is around 1500 ADU. This simple but efficient method assures that the images will be rid of any spurious counts. Figure 5.12 shows a typical bias image. As it as explained above it was taken to extract any spurious count added to the science images.

CCDs are manufactured to be as flawless as possible. Even so the chip can exhibit

Figure 5.12 - A typical bias image taken in October 11, 1997. For every night of observation at least 11 bias images were obtained. Then they were aggregated into a single image, the masterbias, using the median function.
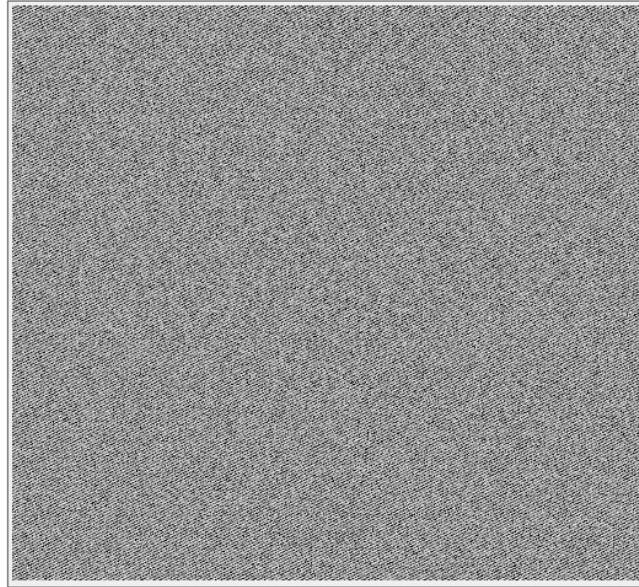
SOURCE: Author

slight variations in sensitivity from pixel to pixel. Those brightness variations cause differences across the image. In addition, defects or obstructions in the optical path can cause illumination fluctuations on the chip. This is the source of the "'dust doughnuts"' seen on uncalibrated CCD images. The reduction process starts the same way as the bias image, processing median function to combine flatfield images. The images are compared, pixel by pixel, and the median of the pixel values from the images are used for the resulting combined image. Other ways to combine images use the average of the pixel values or simply their sum. However, median combining has the advantage that it is insensitive to large outliers from the mean, whereas both the sum and the mean are quite sensitive to large spurious counts. After the creation of a single image with the flat field stack images, called masterflat image, it is divided by each flat field image, creating a new normalized flat. The next step is to divide the science images by this normalized flat. This procedure will lower artificially high pixels and raise artificially low ones, correcting them all to a uniform sensitivity level. In Figure 5.13 it is possible to see the implementation of the process described. In image (A) is seen the raw flatfield image, while the (B) image is the result after the correction. It is also good to remember that flatfields must be obtained with each filter used. During the observations only one filter was used, the 6731 Å filter. Image

55

calibration is a very efficient form to get rid of any systematic error of instrument or persistent noise in the science images.

Figure 5.13 - (A): Flatfield not corrected. Flatfield image where the visible spots are caused by dust and dirt. The dust, along with the scattered light are removed and discounted from the science images. (B): Flatfield after the corrections were implemented. The attenuation of the dust were efficient.
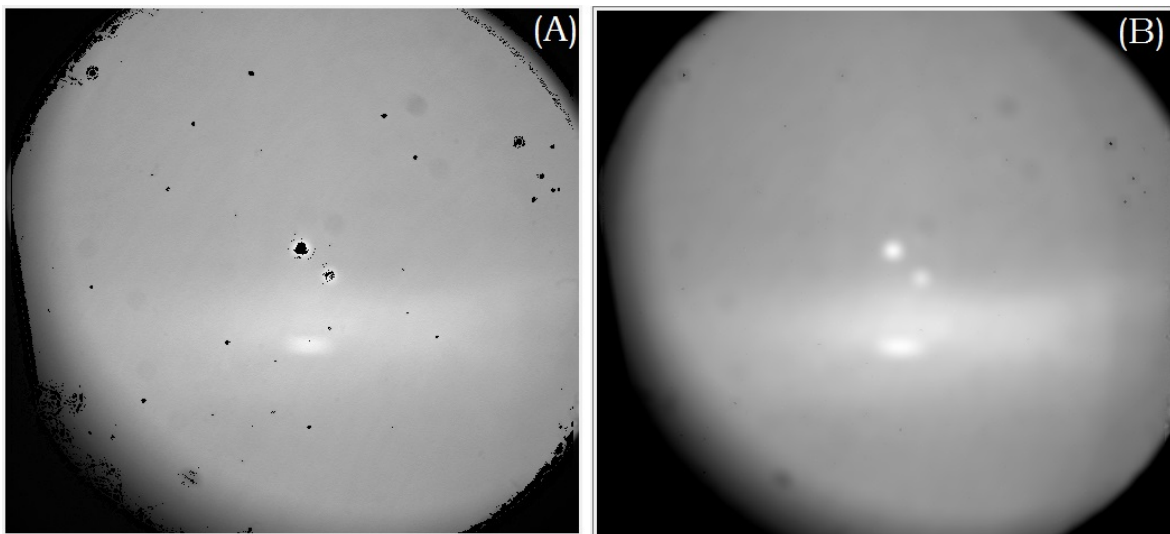
SOURCE: Author

5.3.2 Processing

In our images it was possible to observe Jupiter, the dawn (east) and dusk (west) ansae. Occasionally, a Galilean moon could get at the line-of-sight of one of the ansae. In those cases, the dawn and dusk ansae are not used in the final brightness counting. Figure 5.14 shows a typical science image obtained. It was taken on October 11, 1997. The frame presented shows how the image was displayed using the ATV routine, using the IDL program.

A very efficient method to obtain each ansa brightness is a simple photometric box around it. The ansae move in each exposure and the reduction could be done individually in each image or corrected by the System III longitude. Adjusting to the System III is possible because of the morphology change in the torus. The IPT wobbles together with Jupiter's magnetic field which is deeply connected with the System III longitude. The best way to process the images is to reduce each image

Figure 5.14 - Example of the Io plasma torus image. The brighter part at the sides has no filter applied on it. The strange shape is because the Neutral Density (ND) filter wasn't cut with precision. It doesn't affect our data, especially because the ND filter was used to attenuate Jupiter. Jupiter is at the center of the image, displayed with the *ATV* program of IDL. Closer to the image borders are the region of our interest, the dawn and dusk ansae. At this image is possible to observe both ansae but it is not always possible during all nights of observations. It happens when one or more of the Galilean moons are on our way to observe the ansae. A typical observation is made at a cadence of ~ 15 minutes and clearly show the torus transitioning from the "'open'" state to the "'closed'" state.
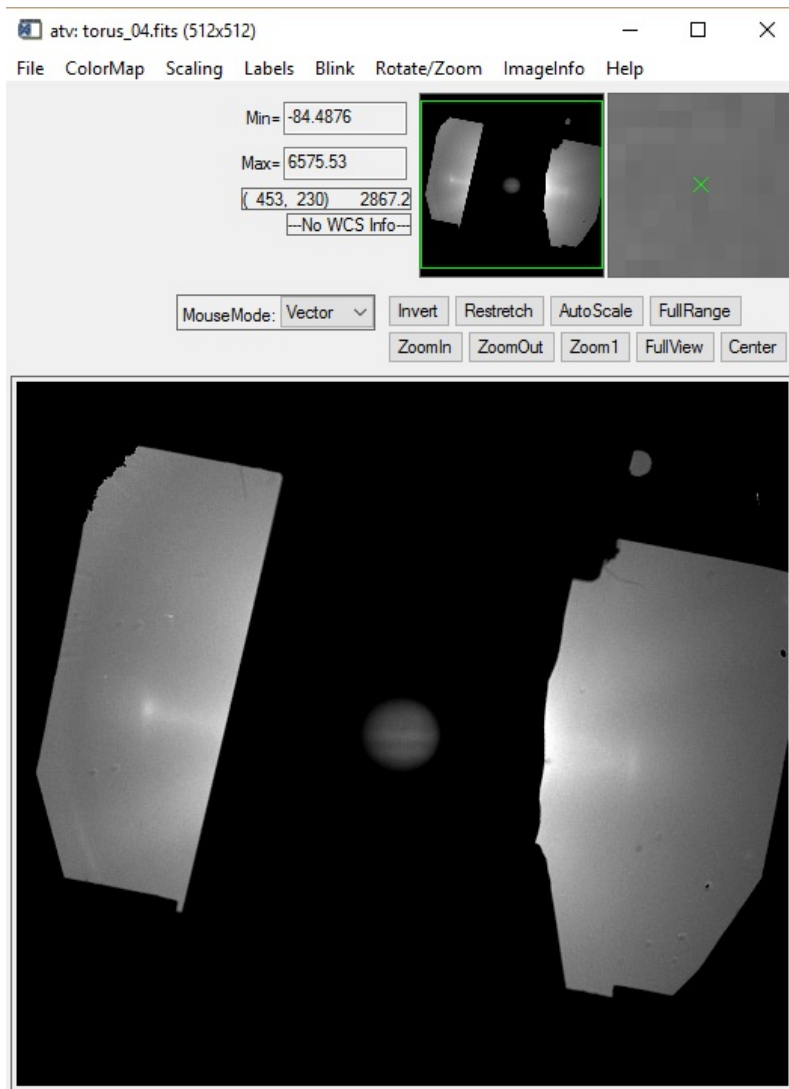
SOURCE: Author

individually as from frame to frame the ansae could vary due to an intensification of the brightness, and for that it is necessary to alter the size of the photometric box. In general, the size of the box used was 25x25 pixels. But there were cases where the size would be a bit larger as the purpose was to "put" the whole area of the ansa observed inside the box. The size of the box used to extract the brightness of the ansae was the same used for the background. Once the [SII] images where fully reduced and analyzed, it was obtained a time sequence of all individual torus configurations for the year of 1997.

Figure 5.15 - Examples of the method applied to extract the brightness of the ansae. The images were observed in October 11 and 14 of 1997. The right side of the (B) image was blocked (the reason why no image is observed) as a Galilean moon was on the way of the dusk ansa.
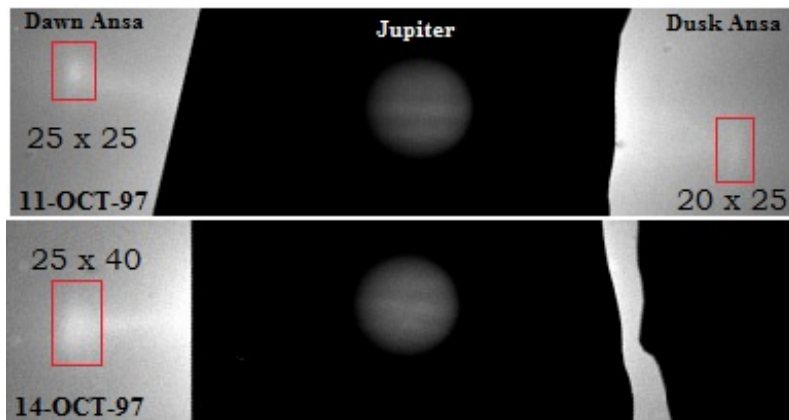
SOURCE: Author

When all the dawn and dusk ansae for the 276 images were obtained the next step is to convert the brightness into Rayleighs. The long formulation is on Appendix A and the short equation to the conversion is:

$$\textbf{conversion} = 0.5 * 10d/(2d * SQRT(2d * alog(2d))) * SQRT(2d * \pi)$$
$$*5.4 * 1D6/((JUPINTC - JUPBKGD) * 1D4) \qquad (5.5)$$
$$*BOXVALUE/(PIXinBOX)$$

where JUPINTC is the central Jovian intensity in a 11x7 pixel region; JUPBKGD

is the background intensity near Jupiter; BOXVALUE is the background subtracted the total ADU value in the ansa box, and PIXinBOX is the total number of pixels in the box. Then the boxes will be in Rayleighs. The statistical errors of the box may be seen in Appendix B. To a more precise calculation it is necessary to take into account the redshift of the IPT ansas to know where the resulting wavelengths fall on the filter transmission curve. From the result of the transmission filter (Figure 5.8), we divide it into the peak filter transmission to correct the above formula. And for that it is necessary to use the JPL ephemeris ($ssd.jpl.nasa.gov/horizons.cgi$) Doppler shift of Jupiter and add the ansa speeds to that.

The images presented in Figures 5.16 and 5.17 show the ansa and scattered light profiles obtained at the raw image (before reduction) and after the reduction was already performed. As it is observed in Figure 5.16, although the ansa profile doesn't seem to be affected by the scattered light, the subtraction of the scattered light is important to make sure no additional noise is being carried to the final results. In Figure 5.17 the same image is shown after all the processes of reduction were applied to the image. As it is possible to observe the noises were efficiently removed from the image.

Figure 5.16 - Science image before the reduction steps. It is possible to observe the profile obtained for the ansa and also the scattered light formed by the light spread in Earth's atmosphere forming a diffuse light in the image. The reduction processes attenuate that effect allowing that the ansa brightness may be observed with no contamination.
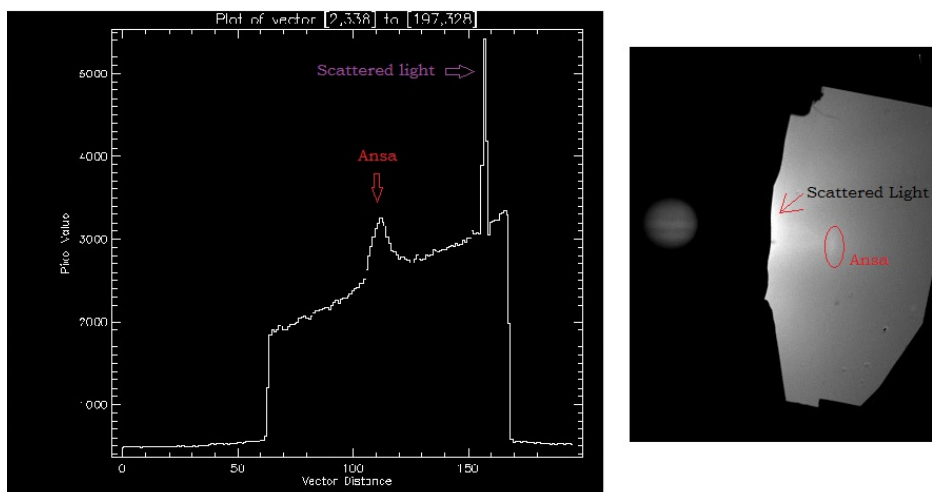
SOURCE: Author

Figure 5.17 - Observation of Jupiter with the dawn (east) ansa. The (A) shows the dawn
ansa profile along (vertical) of the ansa. This result was obtained after the
corrections applied to the science image. The (B) image is a typical image
obtained during the observations and in this case after the whole process
of reductions. (C) presents the profile of the ansa and Jupiter taken in the
horizontal way of the image. The peak observed at the left profile is the
intensity for the ansa. For Jupiter it is possible to observe that ND filter was
efficient to attenuate the planet's brightness.
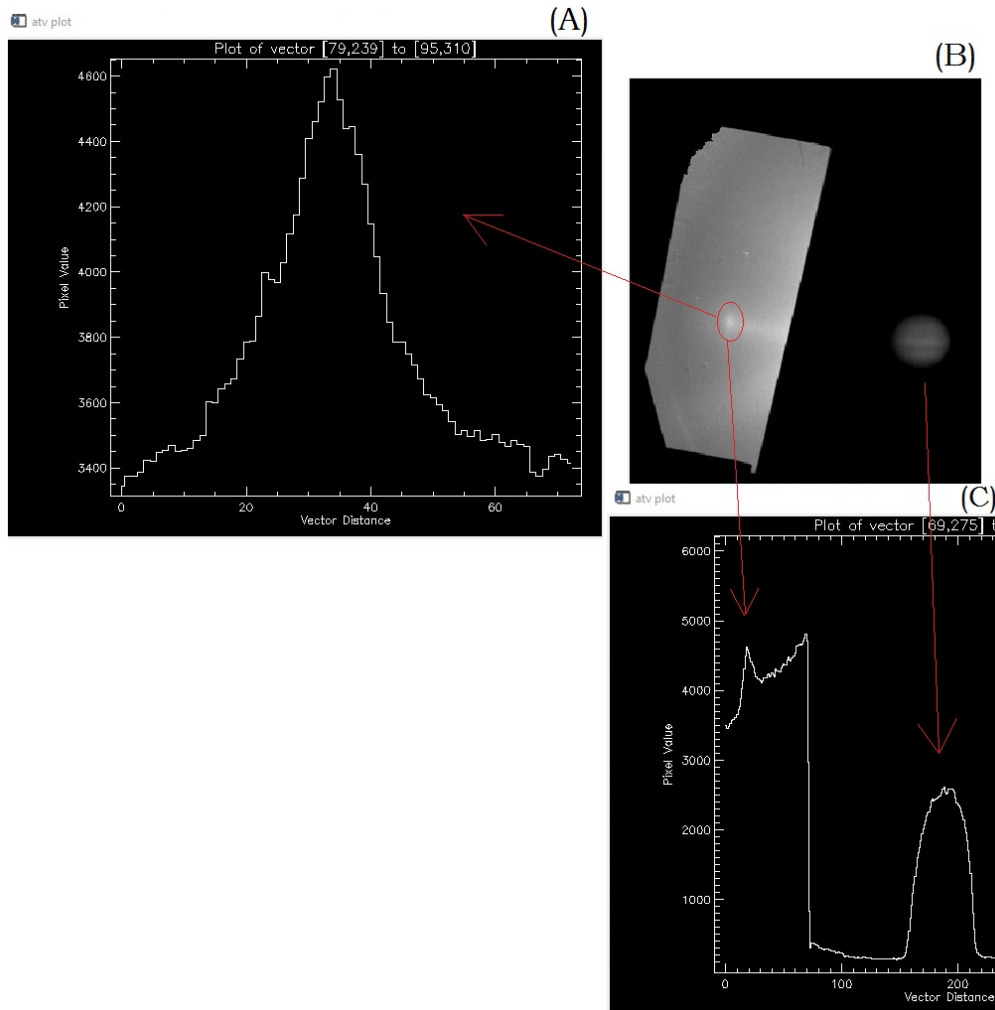
SOURCE: Author

5.3.3 Scattered Light

All images observed from 1997 to 2008 present a persistent azimuthally asymmetric scattered light (Figure 5.18) extending toward the lower left of the images. At first, it seemed a problem from the heliostat mirror. However, repeated cleaning

Figure 5.18 - The scattered light with "sword" format extending toward the lower left. The "sword" adds a time-dependent background to the ansa signal making extraction of the system IV period via periodogram analysis hard to obtain.
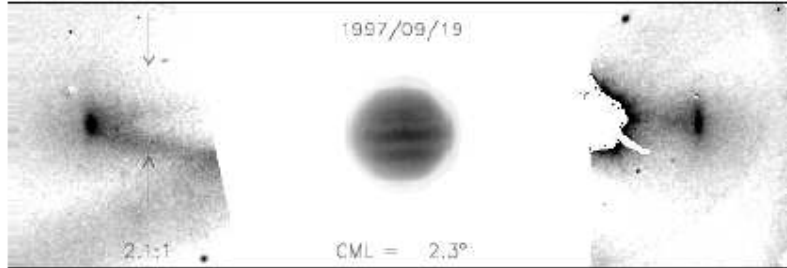
SOURCE: Jeff Morgenthaler

of the mirror did not seem to eliminate the scattered light of the images. During the observing run in 2013, the efforts were invested to understand the source of the azimuthally asymmetric scattered light. As it is possible to see in Figure 5.5, the solar telescope has a long tunnel where the second mirror converts the beam of light to the observation room, direct to the imager. Inside the tunnel, during one of the attempts to understand what was actually generating the azimuthally scattered light, I observed the same characteristic beam of light on the third mirror. Going to the top of the telescope and taking a more careful look, the first mirror of the west auxiliary telescope had the mirror holders with no paint (Figure 5.19). The absence of paint on the holders scatter light asymmetrically into the beam. It formed a "sword" shape in all images, really close to the dawn ansa. Scattered light on astronomical images always adds noise to the results. When the reductions started, the azimuthally asymmetric scattered light didn't seem to be important or would pose a problem to our results. Unfortunately, the scattered light posed as a problem when applying Lomb-Scargle periodogram method to obtain Jupiter's periodicities. In Figure 5.18 is possible to see the [SII] image observed at the MMPST which shows the persistent azimuthal asymmetric scattered light.

The asymmetric scattered light causes a second-order effect on the positions of the IPT ansae and the "sword" is primarily a radial effect. The idea to solve this problem is to perform a polar transform on the data image and then fit with a simple empirical function, such as polynomials in log space for the radial component and polynomials and/or Gaussian for the azimuthal component. Better positions will be obtained when the "sword" is removed.

Figure 5.19 - Image of the top of the solar telescope. The disposition of the mirror of the three telescopes, the east-auxiliary, the west-auxiliary and the main can be seen. Image 3 shows the internal region of the west auxiliary telescope where it is possible to see the telescope holders. Due to erosion (rain, wind, ...), the holders are no longer protected by paint.
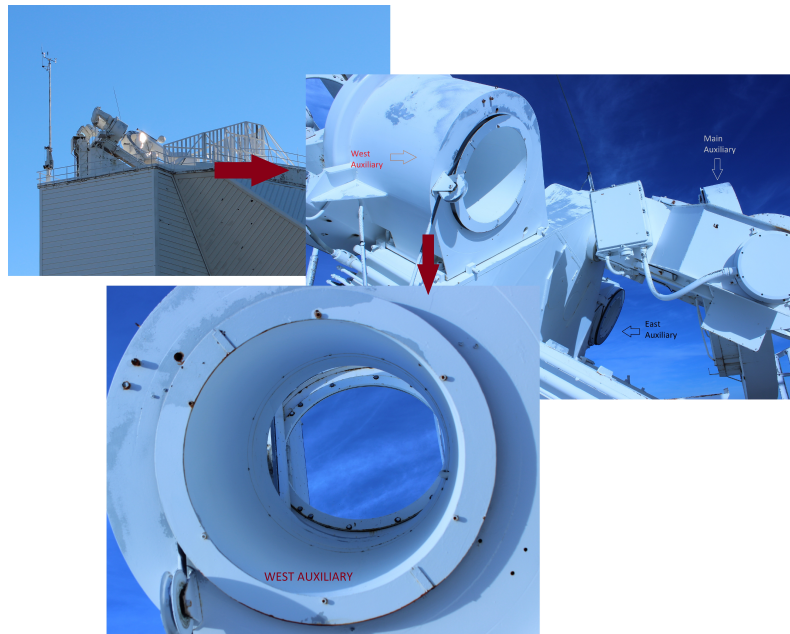
SOURCE: Author

5.4 Lomb-Scargle Periodogram

Most of the ground-based astronomical observations are not uniformly spaced. These problems are due to observations limited to night time, weather and the position of the object under observation. The Lomb-Scargle (LS) Periodogram was a method developed by (107, 108, 109) and is best described as a classical method used to find periodicities in irregularly-sampled data. And that's exactly what we want, to search for the periodic Systems (III and IV) of Jupiter in our sampled data. The reason for the use of periodogram analysis is that it provides a good approximation to the spectrum obtained by fitting sine waves by least-squares to the data and plotting the reduction in the sum of the residuals against frequency (107).

The periodogram is conventionally defined as (108):

(5.6)

Equation 5.6 is the formulation for the classical periodogram. The formulation says that if X contains a sinusoidal component of frequency ω_0, then at and near $\omega = \omega_0$ the factors X(t) and $exp(-i\omega t)$ are in phase and make a large contribution to the sums.

The normalization of the Lomb-Scargle Periodogram is defined as:

$$\hat{p}(\omega) = \frac{1}{\sum_i Y_i^2} \left\{ \frac{[\sum_i y_i cos\omega(t_i - \hat{\tau})}{]}^2 \sum_i cos^2\omega(t_i - \hat{\tau}) + \left\{ \frac{[\sum_i y_i sin\omega(t_i - \hat{\tau})]^2)}{\sum_i sin^2\omega(t_i - \hat{\tau})} \right. \right. \quad (5.7)$$

where the parameter $\hat{\tau}$ is obtained by:

$$tan2\omega\hat{\tau} = \frac{\sum_i sin2\omega t_i}{\sum_i cos2\omega t_i} \quad (5.8)$$

The periodogram involves the computation of a power, $P(w)$, at a set of frequencies, ω_i, measuring the periodic content as a function of period. The LS method is known to be a powerful way to find weak periodic signals. The peak in periodogram indicates a frequency with significant periodicity. One of the reasons to use the LS periodogram instead of, let's say, Fourier method is because of its statistical properties. Statistical behavior of the periodogram is a really important concept and must be analyzed carefully. A noisy data will produce a noisy periodogram and a large number of spurious spectral peaks may occur and be considered as significant peaks when they are not (108). For that, the False-Alarm Probability (FAP) is an extremely important tool to validate the result. The small value for the false-alarm probability indicates a highly significant periodic signal.

Then a power level, z_0, is desired to qualify the detection of the signal:

$$z_0 = -ln[1 - (1 - p_0)^{1/N}] \quad (5.9)$$

where N is the number of frequencies searched for the maximum and the false alarm probability, p_0, is a fixed small number, say $p_0 = 0.01$. As an example if N is 30, Z $(P_X(\omega))$ (108) must be greater than 8 to permit a signal with 99 % confidence.

The method was applied to the brightness obtained from each ansa of the IPT, after converting the ansae intensities to Rayleighs. Due to the azimuthally scattered light in the images and the fact that the scattered light has a periodic signal that is basically the same as System III, the LS periodogram obtained presented noises. The noises prevented to have a more reliable result. The LS formulation and details may be found at (107, 108, 109, 110).

5.5   Near Infrared Mapping Spectrometer (NIMS)

The monitoring of the volcanic activity of Io by the Galileo/*Near Infrared Mapping Spectrometer* instrument started in June 1996. Due to some problems with radiation effects there is no imaging data of Io when the spacecraft made the insertion into Jupiter's orbit in 1995. The NIMS instrument scanned over a 408-wavelength spectrum in the near-infrared range of 0.7-5.2 μm, measuring both reflected sunlight and thermal emission from Io. This spectral range is particularly diagnostic of minerals suspected to occur on planetary and satellite surfaces, and also includes many observable features of atmospheric species (111). The instrument includes a spectrometer with a scanning grating in combination with 17 detectors. The 17 wavelengths obtained for each grating position are acquired simultaneously and the spectra obtained for each different grating may not be precisely at the same spot on the surface as it took 0.33 seconds during the grating steps, meaning the field of view relative to the surface may have changed relative to the previous grating (112). In a more technical way the imaging is performed by a combination of one-dimensional instrument spatial scanning, coupled with orthogonal spacecraft scan-platform motion, yielding two-dimensional images for each of the NIMS wavelengths (111). The image was considered to have a hot spot when at the pixel the positive slope of the spectrum was found between 3.5 and 5 microns and greater than the slope of the spectrum found at pixels surrounding it. NIMS data can be fitted to a Planck function to yield a best-fit black body temperature for the spectra from each pixel (111). NIMS observed Io several times per orbit and most observations were taken at ranges between 244.000 and 866.000 Km, corresponding to spatial resolutions of 122 to 430 km/NIMS pixel. The observations were made in a way that all latitudes were covered and most of them imaged the whole disk. Only a few observations imaged part of the disk (112). An example of how an image was observed by the

NIMS instrument is observed in Figure 5.20.

Figure 5.20 - Io images obtained by the Galileo mission, on the left image observed with the Solid State Imaging (SSI) instrument, and on the right the image obtained with the Near Infrared Mapping Spectrometer (NIMS) instrument. Observations were taken during orbit G2, 6 September 1996. The SSI image shows a multicoloured surface. The NIMS image shows Io at 4.8 μm, with the most intense thermal sources labeled.
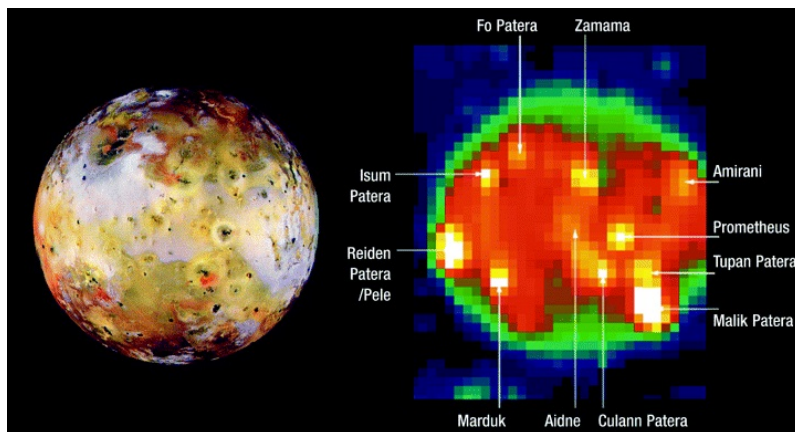
JPL/NASA

Preliminary results of NIMS data presented in (112) show that the single temperature that best fits the NIMS data for any given hot spot can vary significantly from orbit to orbit but this is expected because of variations in volcanic activity. Because of problems of two NIMS detectors also during the extension mission GEM's with the closest approach to Io, only 13 wavelengths were obtained during I24 orbits and subsequently. The reduced number of wavelengths didn't affect the determination of temperature and band ratio mapping for SO_2 (34).

5.5.1 NIMS Data Reduction

The NIMS instrument reduction software also used the IDL language. The NIMS data comes from different orbits, meaning it was acquired at different distances. More attention was given to the thermal emissions observed closer to the limb of Io and also to the orbit distances so all images were able to be compared when analyzing the total brightness of each orbit. For each orbit, in general, at least 10 observations of Io's surface were obtained. Dr. Rosaly Lopes was the primary collaborator for the Io volcanism study. Her participation was possible due to the

CNPq-Science Without Borders program. Dr. Rosaly Lopes expertise with volcanoes and NIMS data interpretation were essential to this part of the thesis, along with the collaboration of Dr. Julie A. Rathbun who joined the group to help with the reduction of the data, as she has experience with ground-based observations.

Figure 5.21 - Flowchart of the main steps taken to reduce the images obtained with the Galileo instrument, NIMS.
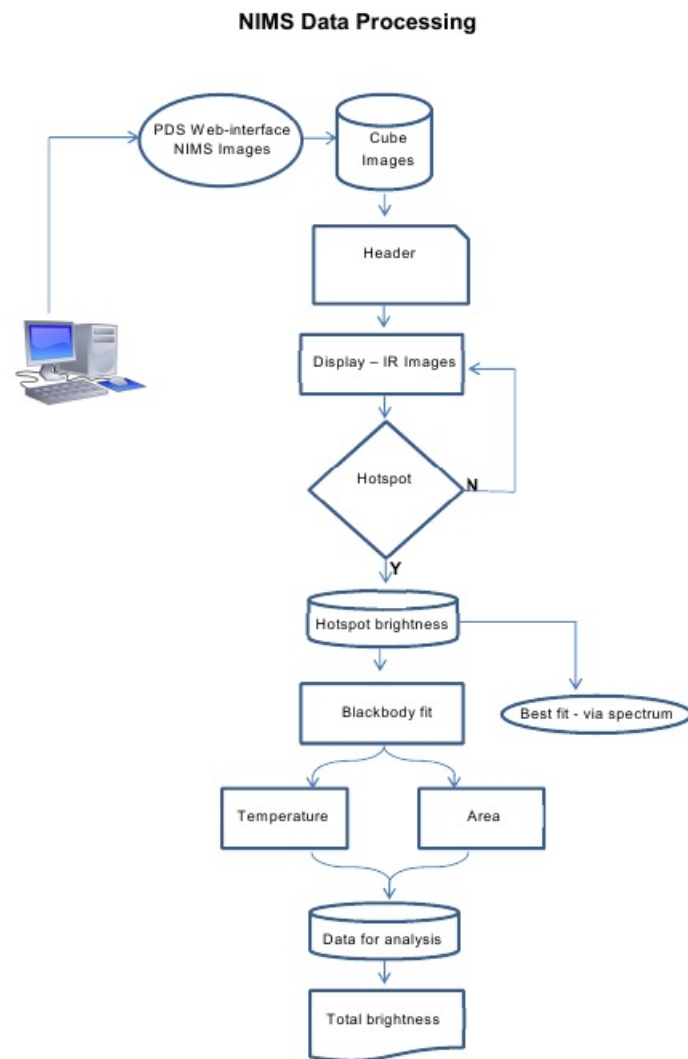
SOURCE: Author

From the 181 frames, a few had to be discarded as we were interested on images that give Io's global output. Then, the orbits designated for compositional mapping (SO_2) or that just observed a strip of Io's surface weren't used. The orbits not used in our analyzes were I24, I25, E26, I27, I31, I32. Therefore, 116 frames obtained with the NIMS instrument were used. The orbits are: G1, G2, C3, E4, E6, G7, G8, C9, C10, E11, E12, E14, E15, E16, C20, C21, C22, E26, G29, C30. Figure 5.21 is a flowchart where is explained the steps used to reduce the NIMS data. Different from the flowchart developed to reduce the IPT data, this one was not separated in pre-processing, processing and data reduction. The NIMS instrument used the image cube as a format to save its data. The image cube is a series of images of the target, each one in a different wavelength. It is also a set of spectra and each spectrum describes a small portion of the area. Then the data may be analyzed spatially, one image at a time. IDL routines were created to extract specific information from the given data cube. Accessing the header of the images it is possible to have all information concerning the observation.

After displaying the image, it was possible to obtain the hotspots intensities. All routines created are user dependent, being possible to choose the best condition of each hotspot. The images used were from dayside, nightside and also during eclipses. The nightside images do not have the problem of reflected sunlight. Eclipse images were also used. But the major problem was with the images of the dayside, as reflected sunlight was easily identified but not necessarily extracted with the method applied. The method applied used the footprint of the pixel on Io to calculate and obtain the spectrum of the hotspot in MW/str/micron. Then, a blackbody fit was adjusted to obtain the spectra. With the Planck's law, the temperature and area of the hotspot analyzed is obtained, along with their uncertainties. An example of the method is shown in Figure 5.22. It presents the results for the orbit G1 and known as G1INNSPEC01. It was obtained in June 28, 1996 and took 408 wavelength spectra in the near-infrared range. Image (A) shows the plus sign marking the hotspots analyzed. Image (B) shows the spectrum obtained at 5° latitude and 76° longitude. The plot is wavelength (μm) versus brightness ($w/\mu m/str$) and shows the best curve adjustment to the spectrum. It was during the first Galileo orbit when the instrument was fully operational. The same image was analyzed and published in Lopes-Gautier et al. (1997) (112). The hotspots obtained at the article matches with the hotspots obtained with our reduction. The image was a nightside observation. The latitudes, longitudes and volcanoes obtained in this thesis reduction are presented in Table 5.1.

Figure 5.22 - (A): Image obtained with NIMS (G1INNSPEC01) instrument. The plus signs represents the hotspots obtained for that image. (B): Spectrum obtained from the highest hotspot at the lower left part of the image. The spectrum is wavelength (μm) versus brightness ($W\mu mstr$). The latitude and longitude is given and also the fit curve to the data.
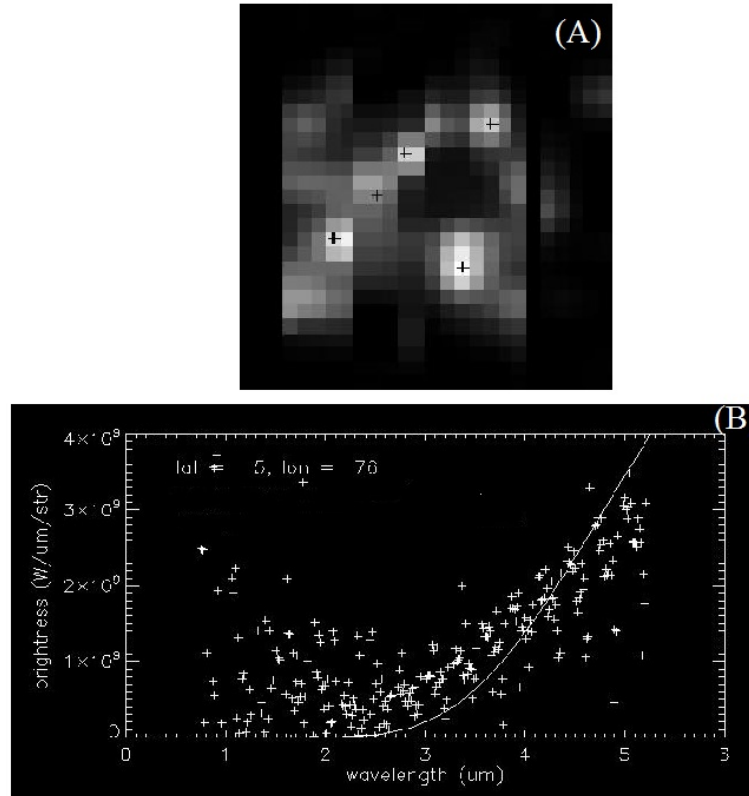
The routine developed during the thesis used a threshold to eliminate the reflected sunlight in the spectra. It was used the same threshold for day and night sides. At first at 3.5 μm and then a second cut at 4.5 μm. But with a higher threshold another problem was faced, there were cases where there were not enough wavelengths left to do the analysis (as it was not always 408-wavelengths observed). It became a problem when adjusting the blackbody fit to small quantity of points. This problem was observed when analysing the temperature obtained. The values were a bit higher than the expected for a single temperature fit. For coincidence, this situation was quite common with the dayside observations.

Table 5.1 - Results obtained from the hotspots analysis of $G1INNSPEC\_01A$ image.

Volcanoes	latitude (°)	longitude (°)	latitude (°) uncertainty	longitude (°) uncertainty
Altjirra	-25.1	107.6	7.27	8.52
Tupan	-10.1	137.9	6.13	6.07
Amirani	33.4	113.8	6.95	9.39
Zal	41.7	62.8	7.88	13.12
Sigurd	-3.3	95.1	6.42	7.75
Prometheus	2.0	153.7	5.77	6.17
Estan Patera	18.5	89.8	6.51	11.07
Culann	-29.4	127.0	7.37	7.02
Hiiaka	5.5	76.2	6.71	14.13

6 Results

After the description of the methods in the previous chapter, here it is presented the results of the data. Recapping, the MMPST results are for the year 1997, which shows the dawn (east) and dusk (west) ansa brightness. Observations were obtained during 14 days on September and during 8 days on October. From the dawn side 154 images were analyzed, while for the dusk side there were 122 images. In Figure 6.1 is plotted all observations for the dawn (top) and dusk (bottom) ansae, which are presented as period versus intensity in Rayleighs ($R \equiv \frac{10^6}{4\pi}$ photons/$cm^2/sr^1/s^1$). Each point on the plot is from an image observed for that day. Although it is part of the same observation run, it is possible to see that we do not have the same amount of observations for the dawn and dusk sides (as explained in the methodology chapter). The presence of one or more Galilean moons in front of the ansa, or close enough to it did not allow to obtain the brightness reliably. From this first results, the dawn side had a higher number of frames obtained during the nights of observations and all the days had observations with brightnesses around 1500 R. On the dusk side only the October period had observations with brightnesses around 1500 R.

Figure 6.1 - Intensity versus time on the dawn and dusk ansae brightness in 1997. Each point is a frame observed for a given day in the panels is plotted intensity versus time.
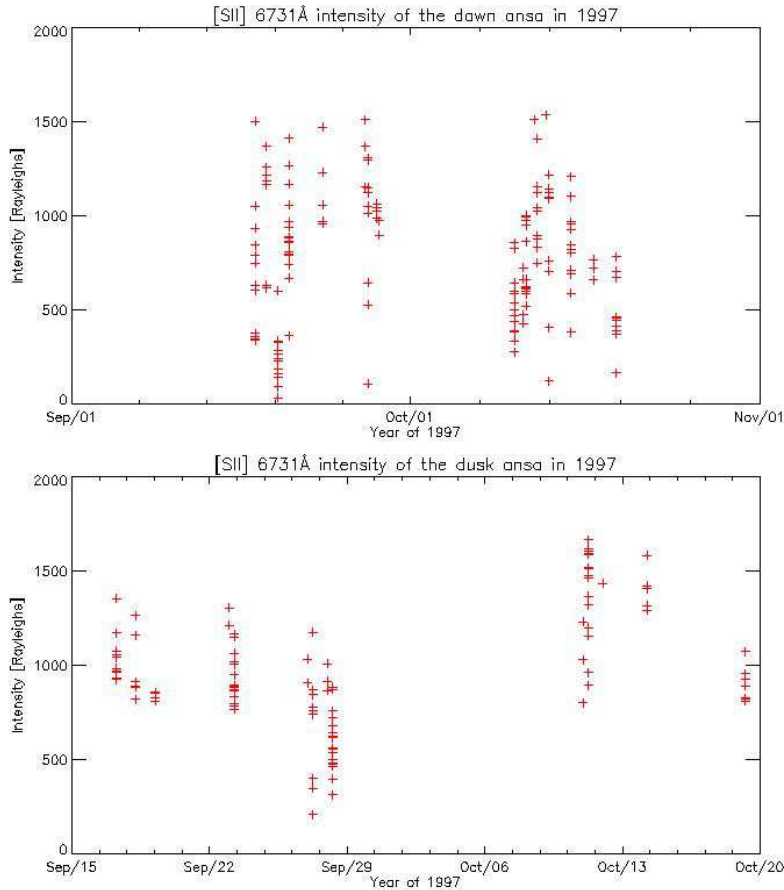
In Figure 6.2 is presented the average position for dawn and dusk side per day of observation. The results in Figure 6.2 show the same period of Figure 6.1 but now they are averaged per day, with their respective deviations. The abscissa shows the day of the year (DOY), from 240 to 320, versus intensity (R). From this plot stays clear the higher intensity on the dusk side when comparing the values from September and October. The highest intensities observed are 1332 R at 284 (October 11 1997), 1434 R at 285 (12 October 1997) and 1403 R at 287 (October 14 1997). While the highest intensity observed at the dawn ansa was 1238 R at 261 (18 September 1997).

Figure 6.2 - Variations of the ansae intensity of the 6731 Å emissions at dawn side at the top panel and dusk side at the bottom panel. Average [SII] of dusk side shows a increase on October when compared with September observations and also for the same period when compared with the dawn side.
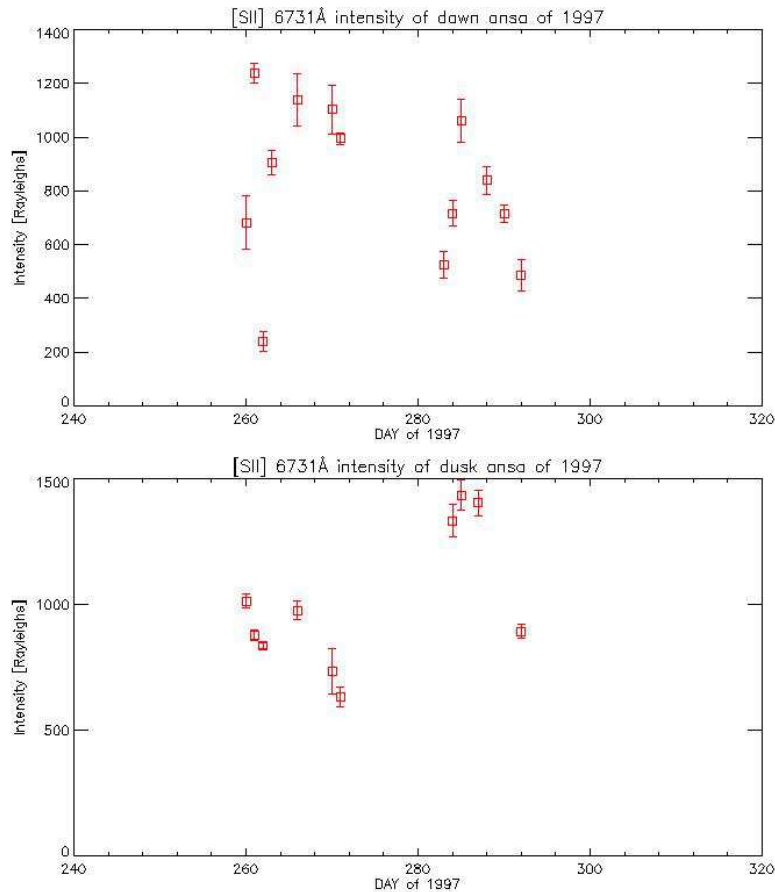
SOURCE: Author

Observations which were obtained in at least two weeks of observations are called as observations of long-term variation and they are thought to reflect Io's variable volcanic activity. All years of observations presented in this thesis (Figure 5.6) were made to last at least two weeks but due to weather conditions or instrument problems, sometimes the amount of days were less than 15 but it still does not invalidate the study of Io's influence at the IPT. The results presented in Figure 6.3 have two horizontal lines, one at 1000 R (red line) and the other at 1500 R (purple line). In our results we had no [SII] intensity higher than 1500 R and it is marked as the limit value of the dawn and dusk intensities. Both figures present DOY versus intensity (R). The top panel shows the results of the dawn ansa intensity variations for the 6731 Å emissions. Along the two months it is not possible to see any considerable

73

increase. The bottom panel shows the dusk ansa intensity variations for the 6731 Å emissions. In October, although the number of observations on the dusk-side were lower when compared with the dawn-side, the dusk intensities were higher, followed by a decrease observed in both ansae. Although there are fewer quantity of data for the dusk ansa, it is clear they seem to be following the same behavior of increase and decrease until the day 263 of the year. After that, both ansae start to increase their intensity, but rapidly a decrease is observed for the dusk side. Then it is the dusk side which starts to increase its intensity, while the dawn side decreases. Any further conclusion is quite difficult as there is only one year analyzed. Thus, in order to give more consistency to our analysis, we shall compare our results with other studies published in the literature.

Figure 6.3 - Long-term variations in the $[SII]$ 6731 Å intensity in the ansa region at dawn side (top panel) and dusk side (bottom panel). Average SII intensity shows a gradual and stable condition at the dawn side and an increase at the dusk side.
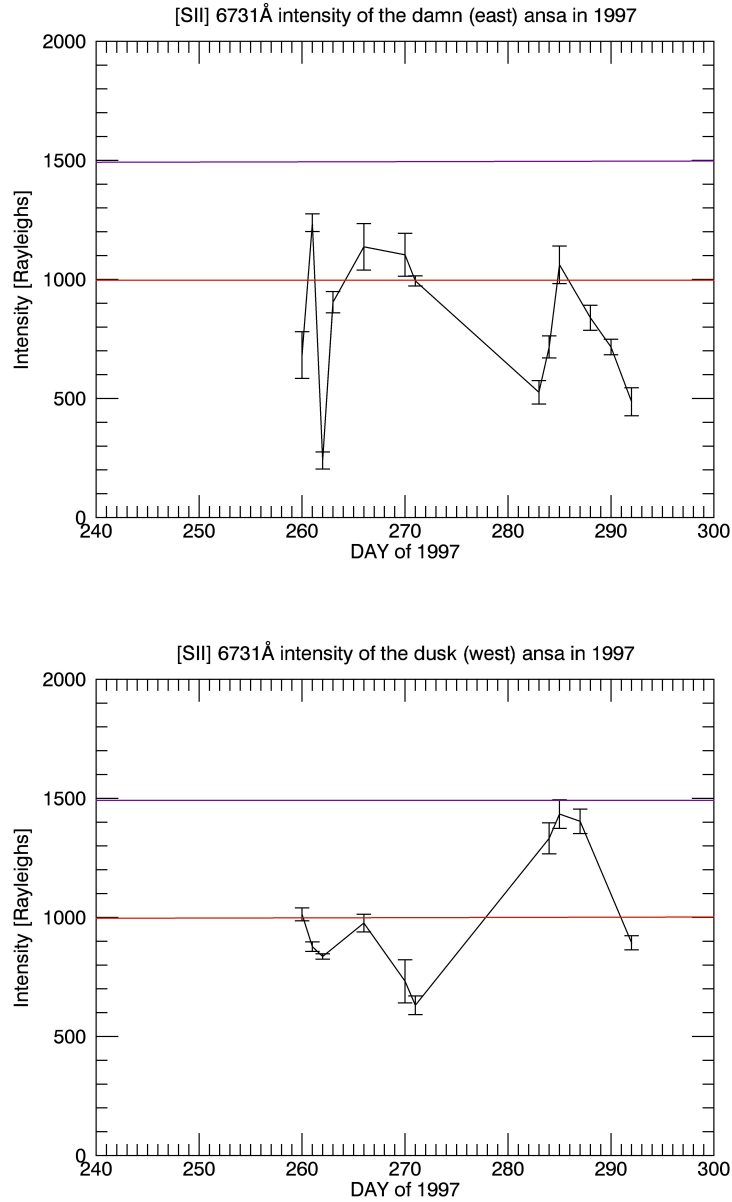
SOURCE: Author

In Figure 6.4 the results are arranged with respect to System III longitude. The system III longitude has a period of 9.925 hours (λ_{III}; $120° \leq \lambda_{III} \leq 180°$). The small amount of points and the fact that they are spread did not allow the adjust-

ment of a sinusoidal function for a better understanding of the behavior of the data regarding the System III. As previous mentioned, the plasma torus wobble, along Jupiter's orbit, is connected to System III.

Figure 6.4 - Ansae variations in intensity of the SII 6731 Å emissions at dawn ansa at the top panel and dusk ansa at the bottom panel for 1997 with respect to System III longitude. Both plots show observed a rapid enhancement relative to the specific range in the System III longitude (λ_{III}; $120° \leq \lambda_{III} \leq 180°$).

SOURCE: Author

76
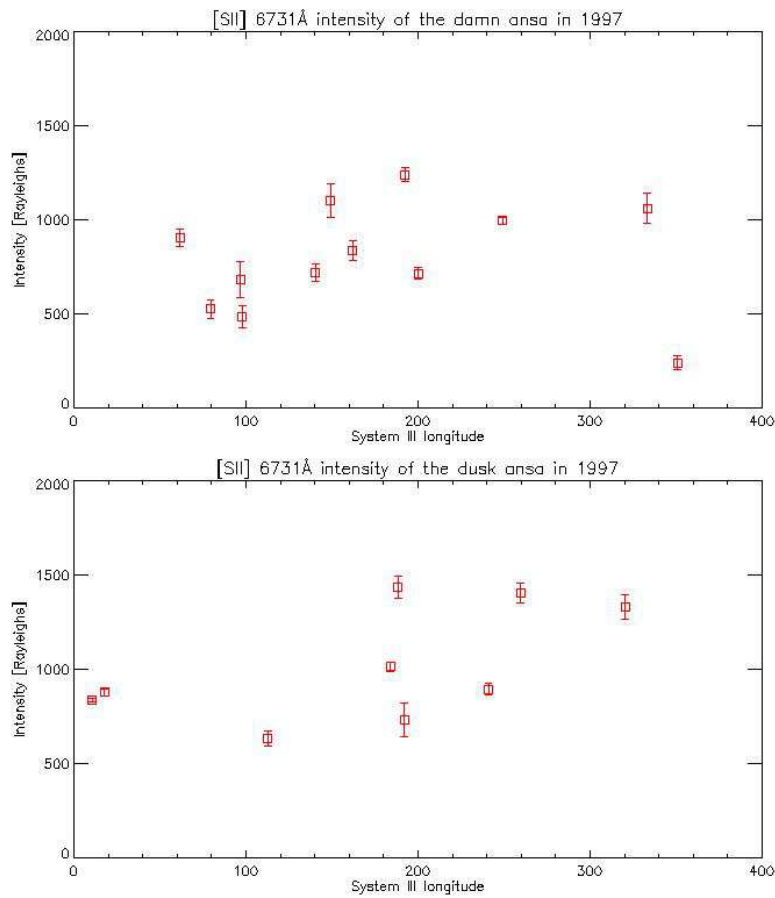
6.0.2 Results compared to the literature

6.0.2.1 Dust article

As previously described (Io chapter), two distinct types of plumes were observed on Io. One called Prometheus, known for release short plumes (~ 100 km), and being optically thick. While the other type of plume is more rare and energetic, exemplified by Pele. These plumes are really high (~ 400 km) and are hard to be observed on reflected light. The last type produces enormous deposits of material on the surface forming red rings, with a radius of ~ 600 km. Figure 6.5 was published by Kruger et al. (2004) (113) and presents the most energetic plumes observed by the Galileo mission assisted by the Dust Detector System (DDS) instrument. In Figure 6.5 it is presented the dust emission rate of Io. The attention is given to the year of 1997, during the G8 and E11 orbits. In 1997 an effusive eruption took place at the Pillan Patera. It lasted for 100 days and occurred between May and September. The Pillan Paterae is a explosion-dominated type of volcano and produces large deposits on Io surface. Pele (latitude: $20° \pm 3°$ S; longitude: $255° \pm 3°$ W) and Pillan (latitude: $13° \pm 3°$ S; longitude: $244° \pm 3°$ W) are located (the latitude and longitude were obtained with the Galileo mission) near each other. The five months period of the dust observation overlap to our ground-based observations. And the volcanoes observed are the ones with intense eruptions (outbursts) which it is expected to affect the IPT variability. No conclusion could be extracted at this point but a deeper analysis of the dust is extremely important to help correlate the events.

Figure 6.5 - Plot with the dust emission rate of Io. The triangles and crosses denote the maxima and minima derived from the measurements in the distance range $13 < r < 30R_J$, respectively (113). Our region of interest is limited by two vertical lines in purple and the Galileo orbits which had significant results for our data are G8 and E11. During that period no significant large-area surface changes have occurred.
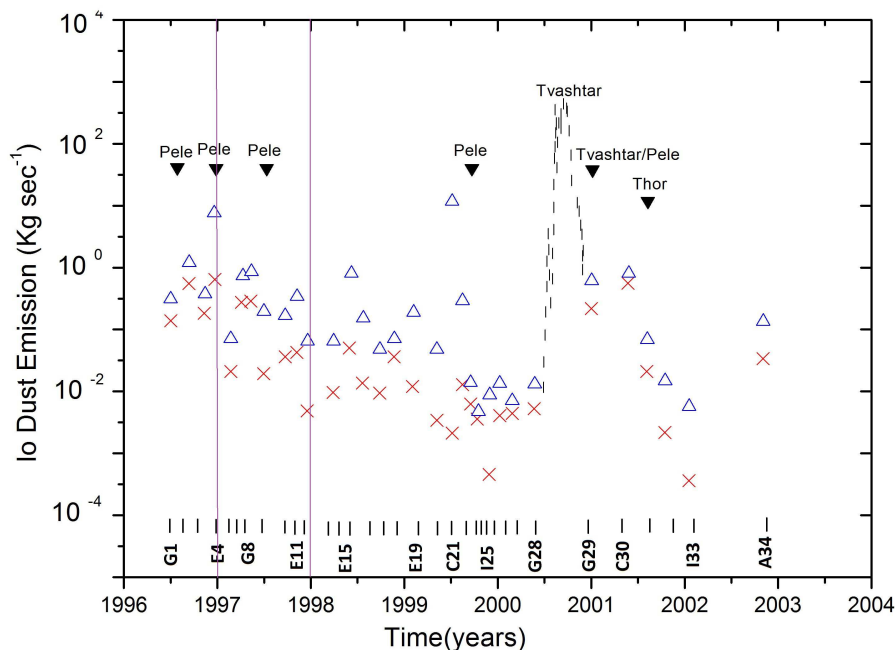
6.0.2.2 Nozawa et al. (2004) (28)

During the development of the thesis, I came across the work of Nozawa et al. (2004) (28). They made a similar study concerning observations of the [SII] 6731 Å emission lines of the IPT. They used a Schmidt-Cassegrain telescope (f28 or f35 cm), with an equatorial mount unit, a narrow-band interference filters and low-noise cooled charge-coupled device (CCD) camera. Observations took place at the Balloon Launching Station of the University of New South Wales, Alice Springs, Australia. Used the same time of exposures, 900 s. They had some problems during their 1997 and 1999 observations, leaving them with results only for the dawn ansa. After a private communication with Dr. Hiromassa Nozawa, he kindly provided the data published in his work of. Their observations were of at least 14 days and the

1997 period of observation being between August and September. More details and information may be found at (28).

In Figure 6.6 the results from the thesis and Nozawa's work are presented. The plot shows the results from August to October. The points plotted in black are the data from August and the red points are from September and October. The plots show period (year) versus intensity (R), and represent the average per night of observation. The main idea was to add Nozawa's results to have a longer period of observation for a better analysis of the plasma torus behavior and also to show the consistency of the thesis results. After an analysis of this longer time series the best conclusion is that the period analyzed from 1997 has no important variation, enhancement or effect observable. It seems a calm period with no considerable variations that would lead us to correlate with intense eruption observed with Pele plume, as mentioned in the previous section. The increase in brightness observed in October could be due to a volcanic eruption affecting the torus variability but with the information we have at this point does not allow more precise conclusions.

Figure 6.6 - Variations of ansae intensity of the SII 6731 Å emissions from the dawn side for 1997 with the red points being the data obtained in this thesis and the black points the data published by Nozawa's (2004) (28).

SOURCE: Author

As presented at the methodology chapter, the Lomb-Scargle Periodogram was the method chosen to obtain the time series of the 1997 data. Figures 6.7 and 6.8 show the time series results. Figure 6.7 shows the result for the dawn side where the highest peak is observed at 10.44h. The expected result was the highest peak to

79
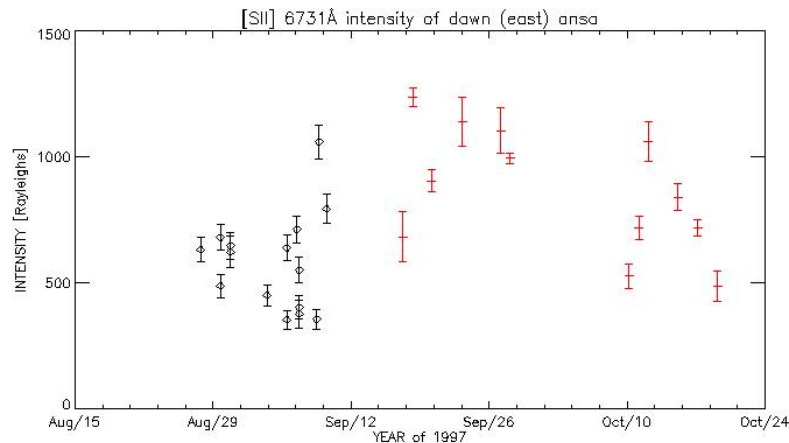
have the frequency of the System III (9.925 h), followed by a second peak, a little less intense, and that would be the System IV (10.20 h (27)). The result is shifted beyond the expected. The same is observed at the dusk side, the results are not as expected. At the dusk side the highest peak observed is at 10.52 h. There is a number of high peaks and that is a good evidence that even with all the image treatments done to eliminate the scattered light, part of it is still there. The noise observed was generated by the azymuthally scattered light that was not removed from our data due to the lack of time. From our results it is possible to observe how the Lomb-Scargle periodogram is a sensitive method due to the presence of noises.The bottom panel in Figure 6.7 is the same result from the top panel but zoomed in to show the region where systems III and IV should be observed.

Figure 6.7 - Periodogram results for the SII 6731 Å emissions at dawn ansa in 1997. The horizontal lines indicate the false-alarm probabilities. The vertical lines at the top image indicate the position of the higher peaks obtained.
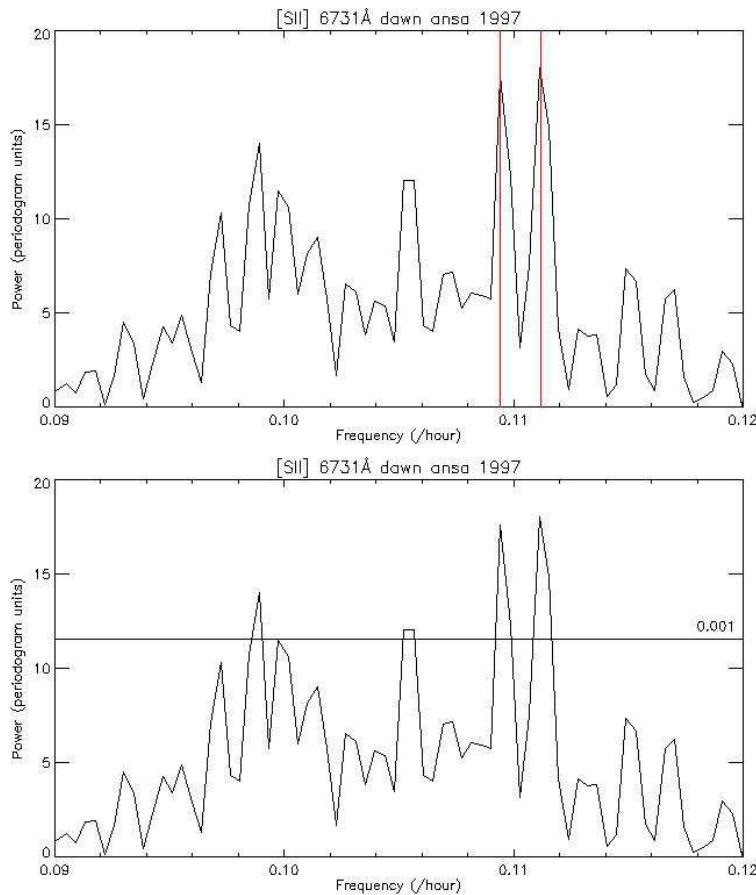
SOURCE: Author

Figure 6.8 - Periodogram results for the SII 6731 Å emissions at dusk ansa in 1997. The horizontal lines indicate the false-alarm probabilities of highest peak. The vertical yellow line at the bottom panel indicates the position of the System III period (9.925 hours).
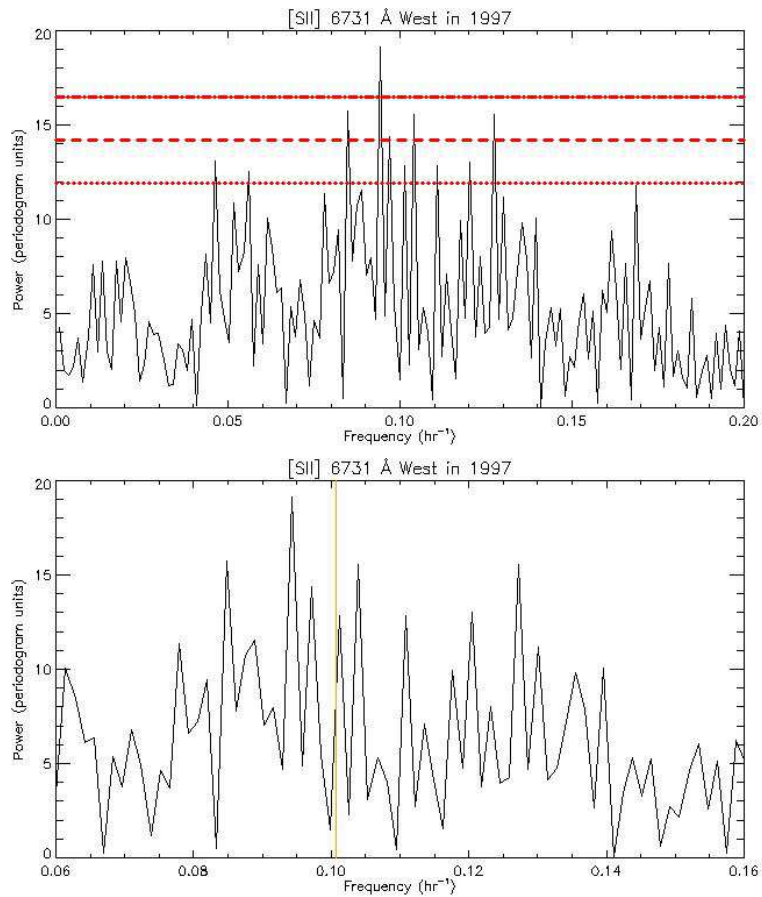
7 Conclusions and Future work

Throughout the text of this thesis, my intention was to give a broad vision of Io and the plasma torus but without forgetting the environment where it is found. But also the importance of the data obtained by space missions and ground-based observations. One of the main goals of this thesis was to understand the coupled system between Io and Jupiter and by analyzing more closely some regions (Io and IPT) it is clear their connection.

In the introduction chapter, the thesis motivations and objectives were presented, while in the methodology chapter not only the method was presented but also the problems which prevented the correlation and full reduction of the ground-based observations. From our results it can be concluded that the IPT ansae brightness have been fully analyzed. The brightness was obtained using the box photometric method and was efficient extracting the brightness of the ansa. A lot of time and effort was applied for the development of this thesis, and still our ultimate goal to correlate the results from the NIMS instrument with the ground-based observations was not achieved. But must certainly all the people involved in the development of this thesis has now a better understanding of the topics covered here. In our results, it was possible to observe a possible enhancement of the torus brightness. As mentioned in the results chapter, the period of dust emission presented at Kruger et al. (2004) (113) was observed between May and September of 1997. At this point it is not possible to confirm that the cause (Pele's plume) and effect (IPT enhancement) are related, but our results showed a variance at the expected period. The lack of the NIMS data made harder the correlation with infrared brightness but the results from the DDS instrument showed that the correlation is possible. However, the physical processes happening between an eruption and the IPT variance must still be studied.

Due to problems found in our routines, developed to reduce the NIMS data, the quantitative correlation with infrared data was not made. The single temperature fit proved to be indeed too simple to obtain thermal temperatures from the hotspots. The reduction of the NIMS data is not really complicated but there was not enough time to implement it for this thesis. On the other hand, the IPT torus reduction is more complicated. The ideas to eliminate the unwanted scattered light ("sword") have already been studied and will be implemented in a near future. The scattered light was a problem when trying to obtain Jupiter's period with the Lomb-Scargle periodogram. The Lomb-Scargle showed to be really sensitive to noise and for that reason the periodogram results obtained are not reliable. The next steps are to

extract the azimuthally scattered light ("sword") from the IPT data and correct the routine to obtain the brightness from Io's hotspots. And thanks to all the effort applied before, now it is known what worked for the reductions and where to start to make the proper corrections. This thesis covered all the steps, from the observations, to the development of the routines for the reductions (IPT and hotspots), to the analysis.

The results obtained in this thesis were compared with Nozawa et al. (2004) (28) to show the consistency with the thesis results. Both data set (thesis and Nozawa's) were acquired in a two week period and together they go from August to October. It was also shown an important result from Kruger et al. (2004) (113) where the dust observed during the whole period of the Galileo orbiter was summarized in one plot. It is eight years of results and when compared to our whole data set of the IPT, it will give important insights from Io's activity and how it is affecting the inner magnetosphere of Jupiter.

For the future, the more natural step to follow is to connect our results with Jupiter's aurora. We aim to know how they are influenced by the torus variability. Radio data of different space mission are available and from them it will be possible to understand how the IPT is affecting Jupiter's magnetosphere, and also observe effects in the magnetosphere and aurorae of Jupiter. The study of the coupled regions of the Jovian system is important to evolve our knowledge in this field of research.

REFERENCES

1   Mendillo, M.; Wilson, J.; Spencer, J.; Stansberry, J. Io's volcanic control of Jupiter's extended neutral clouds. **Icarus**, v. 170, p. 430–442, ago. 2004. 1, 3

2   Wilson, J. K.; Mendillo, M.; Baumgardner, J.; Schneider, N. M.; Trauger, J. T.; Flynn, B. The Dual Sources of Io's Sodium Clouds. **Icarus**, v. 157, p. 476–489, jun. 2002. 1, 32

3   Lopes, R. M. C.; Spencer, J. R. **Io After Galileo: A New View of Jupiter's Volcanic Moon**. United Kingdom: Springer Praxis Books / Geophysical Sciences, 2007. 1, 32

4   Anderson, J. D.; Null, G. W.; Wong, S. K. Gravitational Parameters of the Jupiter System from the Doppler Tracking of Pioneer 10. **Science**, v. 183, p. 322–323, jan. 1974. 2

5   Crary, F. J.; Bagenal, F. Coupling the plasma interaction at Io to Jupiter. **Geophysical Research Letters**, v. 24, p. 2135, set. 1997. 2

6   Bonfond, B.; Grodent, D.; Gérard, J.-C.; Stallard, T.; Clarke, J. T.; Yoneda, M.; Radioti, A.; Gustin, J. Auroral evidence of Io's control over the magnetosphere of Jupiter. **Geophysical Research Letters**, v. 39, p. L01105, jan. 2012. 2

7   Yoneda, M.; Tsuchiya, F.; Misawa, H.; Bonfond, B.; Tao, C.; Kagitani, M.; Okano, S. Io's volcanism controls Jupiter's radio emissions. **Geophysical Research Letters**, v. 40, p. 671–675, fev. 2013. 2

8   Bigg, E. K. Lunar Influences on the Frequency of Magnetic Storms. **Journal of Geophysical Research**, v. 69, p. 4971–4974, dez. 1964. 2, 31

9   Brown, R. A.; Chaffee JR., F. H. High-Resolution Spectra of Sodium Emission from IO. **Astrophysical Journal**, v. 187, p. L125, fev. 1974. 2

10   Morabito, L. A.; Synnott, S. P.; Kupferman, P. N.; Collins, S. A. Discovery of currently active extraterrestrial volcanism. **Science**, v. 204, p. 972, 1979. 2, 19, 25

11   Kupo, I.; Mekler, Y.; Eviatar, A. Detection of ionized sulfur in the Jovian magnetosphere. **Astrophysical Journal**, v. 205, p. L51–L53, abr. 1976. 2, 31, 33, 43

12   Brown, M. E.; Bouchez, A. H. The response of Jupiter's magnetosphere to an outburst on Io. **Science**, v. 278, p. 268–271, out. 1997. 3, 4

13   Treumann, R. A.; Jaroschek, C. H. The Heliospheric Termination Shock. **ArXiv e-prints**, jul. 2008. 7

14   Bagenal, F.; Dowling, T. E.; McKinnon, W. B. **Jupiter**. UK: Cambridge University Press, 2007. 8, 12

15   de Pater, I.; Lissauer, J. J. **Planetary Sciences**. United Kingdom: Cambridge University Press, 2001. 544 p. 7, 8

16   ECHER, E. Magnetosferas planetárias. **Revista Brasileira de Ensino de Física**, scielo, v. 32, p. 1 – 7, 06 2010. ISSN 1806-1117. 8

17   Hill, T. W.; Dessler, A. J.; Goertz, C. K. Magnetospheric models. In: _____. **Physics of the Jovian Magnetosphere**. United States of America: Cambridge Planetary Science Series, 1983. p. 353–394. 8

18   Khurana, K. K.; Kivelson, M. G.; Vasyliunas, V. M.; Krupp, N.; Woch, J.; Lagg, A.; Mauk, B. H.; Kurth, W. S. The configuration of Jupiter's magnetosphere. In: _____. **Jupiter. The Planet, Satellites and Magnetosphere**. UK: Cambridge University Press, 2004. p. 593–616. 8, 9, 10

19   Bagenal, F. Giant planet magnetospheres. **Annual Review of Earth and Planetary Sciences**, v. 20, p. 289–328, 1992. 9

20   Dessler, A. J. **Physics of the Jovian magnetosphere**. United States of America: Cambridge Planetary Science Series, 1983. 9, 10, 11, 35, 41, 42

21   Bagenal, F.; Sullivan, J. D. Direct plasma measurements in the Io torus and inner magnetosphere of Jupiter. **Journal of Geophysical Research**, v. 86, p. 8447–8466, set. 1981. 9, 43

22   Vasyliunas, V. M. Role of the plasma acceleration time in the dynamics of the Jovian magnetosphere. **Geophysical Research Letters**, v. 21, p. 401–404, mar. 1994. 9

23   Winglee, R. M.; Harnett, E. M. Magnetosphere Magnetic Field Wobble Effects on the Dynamics of the Jovian Magnetosphere. **ArXiv e-prints**, jul. 2016. 9

24   Sandel, B. R.; Dessler, A. J. Dual periodicity of the Jovian magnetosphere. **Journal of Geophysical Research**, v. 93, p. 5487–5504, jun. 1988. 11, 12

25   Brown, M. E. Periodicities in the io plasma torus. **Journal of Geophysical Research**, v. 100, p. 21683–21696, 1995. 11, 12, 33

26 Woodward JR., R. C.; Scherb, F.; Roesler, F. L. Periodic intensity variations in sulfur emissions from the io plasma torus. **Icarus**, v. 111, p. 45–64, 1994. 11, 12, 33, 46

27 Roesler, F. L.; Scherb, F.; Oliversen, R. J. Periodic intensity variation in (siii) 9531 a emission from the jupiter plasma torus. **Geophysical Research Letters**, v. 11, p. 128–130, 1984. 11, 12, 80

28 Nozawa, H.; Misawa, H.; Takahashi, S.; Morioka, A.; Okano, S.; Sood, R. Long-term variability of [sii] emissions from the io plasma torus between 1997 and 2000. **Journal of Geophysical Research (Space Physics)**, v. 109, p. 7209, 2004. 11, 12, 33, 36, 84, 102

29 Steffl, A. J.; Delamere, P. A.; Bagenal, F. Cassini UVIS observations of the Io plasma torus. III. Observations of temporal and azimuthal variability. **Icarus**, v. 180, p. 124–140, jan. 2006. 12

30 Douglas, J. N. A Uniform Statistical Analysis of Jovian Decameter Radiation, 1950. **Astronomical Journal**, v. 65, p. 487–488, 1960. 12

31 Seidelmann, P. K.; Divine, N. Evaluation of Jupiter Longitudes in System III(1965). In: **Bulletin of the American Astronomical Society**. USA: Bulletin of the American Astronomical Society, 1977. (Bulletin of the American Astronomical Society, v. 9), p. 474. 12

32 Murakami, G.; Yoshioka, K.; Yamazaki, A.; Uemizu, K.; Ishii, H.; Uji, K.; Yoshikawa, I.; Kagitani, M.; Tsuchiya, F. EXCEED: an extreme ultraviolet spectrometer onboard SPRINT-A. In: **Space Telescopes and Instrumentation 2012: Ultraviolet to Gamma Ray**. Japan: Space Telescopes and Instrumentation 2012: Ultraviolet to Gamma Ray. Proceedings of the SPIE, 2012. (procspie, v. 8443), p. 84432Y. 14

33 Lopes, R. M. C.; Williams, D. A. Io after galileo. **Reports on Progress in Physics**, v. 68, p. 303–340, 2005. 15, 23, 28, 31, 33, 34, 105

34 Perry, J.; Lopes, R. M. C.; Spencer, J. R.; Alexander, C. A summary of the Galileo mission and its observations of Io. In: _____. **Io After Galileo: A New View of Jupiter's Volcanic Moon**. United Kingdom: Springer Praxis Books / Geophysical Sciences, 2007. p. 35. 15, 16, 65

35 Lopes-Gautier, R.; Douté, S.; Smythe, W. D.; Kamp, L. W.; Carlson, R. W.; Davies, A. G.; Leader, F. E.; McEwen, A. S.; Geissler, P. E.; Kieffer, S. W.;

Keszthelyi, L.; Barbinis, E.; Mehlman, R.; Segura, M.; Shirley, J.; Soderblom, L. A. A Close-Up Look at Io from Galileo's Near-Infrared Mapping Spectrometer. **Science**, v. 288, p. 1201–1204, maio 2000. 15

36   Anderson, J. D.; Lau, E. L.; Sjogren, W. L.; Schubert, G.; Moore, W. B. Gravitational constraints on the internal structure of Ganymede. **Nature**, v. 384, p. 541–543, dez. 1996. 16

37   Lopes-Gautier, R.; McEwen, A. S.; Smythe, W. B.; Geissler, P. E.; Kamp, L.; Davies, A. G.; Spencer, J. R.; Keszthelyi, L.; Carlson, R.; Leader, F. E.; Mehlman, R.; Soderblom, L.; The Galileo NIMS; SSI Teams. Active Volcanism on Io: Global Distribution and Variations in Activity. **Icarus**, v. 140, p. 243–264, ago. 1999. 17, 26

38   Schubert, G.; Anderson, J. D.; Spohn, T.; McKinnon, W. B. Interior composition, structure and dynamics of the Galilean satellites. In: _____. **Jupiter. The Planet, Satellites and Magnetosphere**. UK: Cambridge University Press, 2004. p. 281–306. 19

39   Pappalardo, R. T.; Collins, G. C.; Head III, J. W.; Helfenstein, P.; McCord, T. B.; Moore, J. M.; Prockter, L. M.; Schenk, P. M.; Spencer, J. R. Geology of Ganymede. In: _____. **Jupiter. The Planet, Satellites and Magnetosphere**. UK: Cambridge University Press, 2004. p. 363–396. 20

40   Heller, R.; Pudritz, R. Water Ice Lines and the Formation of Giant Moons around Super-Jovian Planets. **Astrophysical Journal**, v. 806, p. 181, jun. 2015. 20

41   Spencer, J. R.; Schneider, N. M. Io on the Eve of the Galileo Mission. **Annual Review of Earth and Planetary Sciences**, v. 24, p. 125–190, 1996. 21, 23, 24

42   Kivelson, M. G.; Bagenal, F.; Kurth, W. S.; Neubauer, F. M.; Paranicas, C.; Saur, J. Magnetospheric interactions with satellites. In: _____. **Jupiter. The Planet, Satellites and Magnetosphere**. UK: Cambridge University Press, 2004. p. 513–536. 21

43   Veeder, G. J.; Matson, D. L.; Johnson, T. V.; Blaney, D. L.; Goguen, J. D. Io's heat flow from infrared radiometry: 1983-1993. **Journal of Geophysical Research**, v. 99, p. 17095–17162, ago. 1994. 21, 24

44   Peale, S. J.; Cassen, P.; Reynolds, R. T. Melting of io by tidal dissipation. **Science**, v. 203, p. 892–894, 1979. 21

45   Rathbun, J. A.; Spencer, J. R.; Davies, A. G.; Howell, R. R.; Wilson, L. Loki, Io: A periodic volcano. **Geophysical Research Letters**, Geophysical Research Letters, AGU, v. 29, p. 84–1, maio 2002. 22, 24

46   Spencer, J. R.; Rathbun, J. E.; Travis, L. D.; Tamppari, L. K.; Barnard, L.; Martin, T. Z. A Closeup Look at Io's Volcanos with Galileo PPR. In: **AAS/Division for Planetary Sciences Meeting Abstracts #32**. USA: American Astronomical Society, 2000. (Bulletin of the American Astronomical Society, v. 32), p. 1045. 22, 24

47   Carr, M. H.; McEwen, A. S.; Howard, K. A.; Chuang, F. C.; Thomas, P.; Schuster, P.; Oberst, J.; Neukum, G.; Schubert, G.; Galileo Imaging Team. Mountains and Calderas on Io: Possible Implications for Lithosphere Structure and Magma Generation. **Icarus**, v. 135, p. 146–165, set. 1998. 22

48   GEISSLER, P. Volcanic Activity on Io During the Galileo Era. **Annual Review of Earth and Planetary Sciences**, v. 31, p. 175–211, 2003. 22, 26

49   Radebaugh, J.; Keszthelyi, L. P.; McEwen, A. S.; Turtle, E. P.; Jaeger, W.; Milazzo, M. Paterae on Io: A new type of volcanic caldera? **Journal of Geophysical Research**, v. 106, p. 33005–33020, dez. 2001. 22, 23, 25

50   Davies, A. G. **Volcanism on Io**. New York: Cambridge Planetary Science, 2014. 22, 28

51   LOPES, R.; MITCHELL, K.; WILLIAMS, D.; MITRI, G. Beyond earth: How extra-terrestrial volcanism has changed our definition of a volcano. **Special Paper of the Geological Society of America**, Geological Society of America, v. 470, p. 11–30, 2010. ISSN 0072-1077. 23

52   Williams, D. A.; Howell, R. R. Active volcanism: Effusive eruptions. In: _____. **Io After Galileo: A New View of Jupiter's Volcanic Moon**. United Kingdom: Springer Praxis Books / Geophysical Sciences, 2007. p. 133. 23

53   Keszthelyi, L.; McEwen, A. S.; Phillips, C. B.; Milazzo, M.; Geissler, P.; Turtle, E. P.; Radebaugh, J.; Williams, D. A.; Simonelli, D. P.; Breneman, H. H.; Klaasen, K. P.; Levanas, G.; Denk, T.; Galileo SSI Team. Imaging of volcanic activity on Jupiter's moon Io by Galileo during the Galileo Europa Mission and the Galileo Millennium Mission. **Journal of Geophysical Research**, v. 106, p. 33025–33052, dez. 2001. 25

54   Lopes, R. M. C.; Kamp, L. W.; Smythe, W. D.; Mouginis-Mark, P.; Kargel, J.; Radebaugh, J.; Turtle, E. P.; Perry, J.; Williams, D. A.; Carlson, R. W.; Douté, S.; the Galileo NIMS; SSI Teams. Lava lakes on Io: observations of Io's volcanic activity from Galileo NIMS during the 2001 fly-bys. **Icarus**, v. 169, p. 140–174, maio 2004. 23

55   Lopes, R. M. C.; Kamp, L. W.; Douté, S.; Smythe, W. D.; Carlson, R. W.; McEwen, A. S.; Geissler, P. E.; Kieffer, S. W.; Leader, F. E.; Davies, A. G.; Barbinis, E.; Mehlman, R.; Segura, M.; Shirley, J.; Soderblom, L. A. Io in the near infrared: Near-Infrared Mapping Spectrometer (NIMS) results from the Galileo flybys in 1999 and 2000. **Journal of Geophysical Research**, v. 106, p. 33053–33078, dez. 2001. 23, 28

56   Radebaugh, J.; McEwen, A. S.; Milazzo, M. P.; Keszthelyi, L. P.; Davies, A. G.; Turtle, E. P.; Dawson, D. D. Observations and temperatures of Io's Pele Patera from Cassini and Galileo spacecraft images. **Icarus**, v. 169, p. 65–79, maio 2004. 23

57   Rathbun, J. A.; Johnson, S. T.; Spencer, J. R. Loki, Io: An Update on Activity from Groundbased Data. In: Mackwell, S.; Stansbery, E. (Ed.). **Lunar and Planetary Science Conference**. LPI: 34th Annual Lunar and Planetary Science Conference, 2003. (Lunar and Planetary Science Conference, v. 34). 24

58   Rathbun, J. A.; Spencer, J. R. Io from Ground-based Eclipse Observations: Implications for the Eruptive History of Loki. **AGU Fall Meeting Abstracts**, American Geophysical Union, AGU, dez. 2008. 24

59   Spencer, J. R.; Rathbun, J. A.; Travis, L. D.; Tamppari, L. K.; Barnard, L.; Martin, T. Z.; McEwen, A. S. Io's Thermal Emission from the Galileo Photopolarimeter- Radiometer. **Science**, v. 288, p. 1198–1201, maio 2000. 24

60   Spencer, J. R.; Howell, R. R.; Clark, B. E.; Klassen, D. R.; O'Connor, D. Volcanic activity on Io at the time of the ULYSSES encounter. **Science**, v. 257, p. 1507–1510, set. 1992. 24

61   Davies, A. G.; Keszthelyi, L. P.; Lopes-Gautier, R. M. C.; Smythe, W. D.; Carlson, L. K. R. W.; Nims, G.; SSI Teams. Eruption Evolution of Major Volcanoes on Io: Galileo Takes a Close Look. In: **Lunar and Planetary Science Conference**. LPI: 31st Annual Lunar and Planetary Science Conference, 2000. (Lunar and Planetary Science Conference, v. 31). 24

62   GEISSLER P. E. MCEWEN, A. P. C. K. L. S. J. Surface changes on io during the galileo mission. In: **EGS - AGU - EUG Joint Assembly**. EGU: EGS - AGU - EUG Joint Assembly, 2003. 25

63   Geissler, P. E. Volcanic Plumes and Plume Deposits on Io. In: Mackwell, S.; Stansbery, E. (Ed.). **36th Annual Lunar and Planetary Science Conference**. LPI: 36th Annual Lunar and Planetary Science Conference, 2005. (Lunar and Planetary Science Conference, v. 36). 25, 27

64   Geissler, P. E.; Goldstein, D. B. Plumes and their deposits. In: _____. **Io After Galileo: A New View of Jupiter's Volcanic Moon**. Chichester, UK: Springer Praxis Books / Geophysical Sciences, 2007. p. 163. 25, 26

65   Spencer, J. R.; Sartoretti, P.; Ballester, G. E.; McEwen, A. S.; Clarke, J. T.; McGrath, M. A. Pele plume (Io): Observations with the Hubble Space Telescope. **Geophysical Research Letters**, v. 24, p. 2471, out. 1997. 26

66   McEwen, A. S.; Keszthelyi, L.; Spencer, J. R.; Schubert, G.; Matson, D. L.; Lopes-Gautier, R.; Klaasen, K. P.; Johnson, T. V.; Head, J. W.; Geissler, P.; Fagents, S.; Davies, A. G.; Carr, M. H.; Breneman, H. H.; Belton, M. J. S. High-temperature silicate volcanism on jupiter's moon io. **Science**, v. 281, p. 87, 1998. 26

67   Geissler, P. E.; McEwen, A. S.; Keszthelyi, L.; Lopes-Gautier, R.; Granahan, J.; Simonelli, D. P. Global Color Variations on Io. **Icarus**, v. 140, p. 265–282, ago. 1999. 26

68   Tsang, C. C. C.; Rathbun, J. A.; Spencer, J. R.; Hesman, B. E.; Abramov, O. Io's hot spots in the near-infrared detected by LEISA during the New Horizons flyby. **Journal of Geophysical Research (Planets)**, v. 119, p. 2222–2238, out. 2014. 27

69   Kieffer, S. W. Dynamics and thermodynamics of volcanic eruptions - Implications for the plumes on Io. In: Morrison, D. (Ed.). **Satellites of Jupiter**. STI: In: Satellites of Jupiter, 1982. p. 647–723. 28

70   Johnson, T. V.; Blaney, D. B.; Davies, A. G.; Matson, D. L.; Veeder, G. J. Resurfacing Io with Silicates. In: **AAS/Division for Planetary Sciences Meeting Abstracts #27**. ADS: American Astronomical Society, 1995. (Bulletin of the American Astronomical Society, v. 27), p. 1161. 28

71 Radebaugh, J.; Jaeger, W. L.; Keszthelyi, L. P.; Turtle, E. P.; Milazzo, M. P.; Perry, J.; McEwen, A. S.; Lopes, R.; Davies, A. G.; Geissler, P. Relationships Between Paterae, Mountains, and Hotspots on Io from a Global Database. In: Mackwell, S.; Stansbery, E. (Ed.). **Lunar and Planetary Science Conference**. LPI: 35th Lunar and Planetary Science Conference, 2004. (Lunar and Planetary Science Conference, v. 35). 28

72 Marchis, F.; de Pater, I.; Davies, A. G.; Roe, H. G.; Fusco, T.; Mignant, D. L.; Descamps, P.; Macintosh, B. A.; Prangé, R. High-Resolution Keck Adaptive Optics Imaging of Violent Volcanic Activity on Io. **Icarus**, v. 160, p. 124–131, nov. 2002. 29

73 Tsang, C. C. C.; Spencer, J. R.; Jessup, K. L. Io's Atmosphere in 2010: Synergistic Observations of Longitudinal Distribution in the Near-Ultraviolet and the Mid-Infrared. In: **Lunar and Planetary Science Conference**. LPI: 43rd Lunar and Planetary Science Conference, 2012. (Lunar and Planetary Science Conference, v. 43), p. 2789. 29

74 Ballester, G. E.; McGrath, M. A.; Stobel, D. F.; Zhu, X.; Feldman, P. D.; Moos, H. W. Detection of the SO2 atmosphere on Io with the Hubble Space Telescope. **Icarus**, v. 111, p. 2–17, set. 1994. 29

75 Ingersoll, A. P. Io meteorology - How atmospheric pressure is controlled locally by volcanos and surface frosts. **Icarus**, v. 81, p. 298–313, out. 1989. 29

76 Moreno, M. A.; Schubert, G.; Kivelson, M. G.; Paige, D. A.; Baumgardner, J. Io's volcanic and sublimation atmospheres. **Icarus**, v. 93, p. 63–81, set. 1991. 29

77 Hinson, D. P.; Kliore, A. J.; Flasar, F. M.; Twicken, J. D.; Schinder, P. J.; Herrera, R. G. Galileo radio occultation measurements of Io's ionosphere and plasma wake. **Journal of Geophysical Research**, v. 103, p. 29343–29358, dez. 1998. 29

78 Moses, J. I.; Zolotov, M. Y.; Fegley, B. Photochemistry of a Volcanically Driven Atmosphere on Io: Sulfur and Oxygen Species from a Pele-Type Eruption. **Icarus**, v. 156, p. 76–106, mar. 2002. 29

79 Zolotov, M. Y.; Fegley, B. Volcanic Origin of Disulfur Monoxide (S $_2$O) on Io. **Icarus**, v. 133, p. 293–297, jun. 1998. 29

80 McGrath, M. A. Hubble Space Telescope Observations of Europa and Ganymede. **AGU Fall Meeting Abstracts**, dez. 2002. 29

81   Herbert, F.; Schneider, N. M.; Hendrix, A. R.; Bagenal, F. Hubble Space Telescope observations of sulfur ions in the Io plasma torus: New constraints on the plasma distribution. **Journal of Geophysical Research (Space Physics)**, v. 108, p. 1167, maio 2003. 31

82   Goodman, E. W. **A fine-structure chemistry model of the Io plasma torus**. Tese (Doutorado) — University of Southern California, 2006. 31

83   Burke, B. F.; Franklin, K. L. Observations of a Variable Radio Source Associated with the Planet Jupiter. **Journal of Geophysical Research**, v. 60, p. 213–217, jun. 1955. 31

84   Brown, R. A. Optical line emission from Io. In: Woszczyk, A.; Iwaniszewska, C. (Ed.). **Exploration of the Planetary System**. STI: In: Exploration of the planetary system; Proceedings of the Symposium, 1974. (IAU Symposium, v. 65), p. 527–531. 31, 32

85   Connerney, J. E. P.; Baron, R.; Satoh, T.; Owen, T. Images of Excited H_3^+ at the Foot of the Io Flux Tube in Jupiter's Atmosphere. **Science**, v. 262, p. 1035–1038, nov. 1993. 32

86   Trafton, L. An explanation for the alternating north-south asymmetry of Io's sodium cloud. **Icarus**, v. 44, p. 318–325, nov. 1980. 33

87   Pilcher, C. B. Images of Jupiter's sulfur ring. **Science**, v. 207, p. 181–183, jan. 1980. 33, 43

88   Trauger, J. T.; Muench, G.; Roesler, F. L. A study of the Jovian forbidden line S II nebula at high spectral resolution. **Astrophysical Journal**, v. 236, p. 1035–1042, mar. 1980. 33

89   Morgan, J. S. Models of the io torus. **Icarus**, v. 63, p. 243–265, 1985. 33

90   _____. Temporal and spatial variations in the Io torus. **Icarus**, Lunar and Planetary Exploration; Satellites of Jupiter, v. 62, p. 389–414, jun. 1985. 33

91   Schneider, N. M.; Trauger, J. T. The Structure of the Io Torus. **Astrophysical Journal**, v. 450, p. 450, set. 1995. 33

92   Woodward JR., R. C.; Scherb, F.; Roesler, F. L.; Mendillo, M.; Wilson, J.; Spencer, J.; Stansberry, J. Variations in optical s$^+$ emission from the io plasma torus: Evidence for quasi periodicity. **Astrophysical Journal**, v. 479, p. 984–991, ago. 1997. 33, 46

93   Broadfoot, A. L.; Belton, M. J.; Takacs, P. Z.; Sandel, B. R.; Shemansky, D. E.; Holberg, J. B.; Ajello, J. M.; Moos, H. W.; Atreya, S. K.; Donahue, T. M.; Bertaux, J. L.; Blamont, J. E.; Strobel, D. F.; McConnell, J. C.; Goody, R.; Dalgarno, A.; McElroy, M. B. Extreme ultraviolet observations from voyager 1 encounter with jupiter. **Science**, v. 204, p. 979–982, 1979. 34

94   Sandel, B. R.; Shemansky, D. E.; Broadfoot, A. L.; Bertaux, J. L.; Blamont, J. E.; Belton, M. J. S.; Ajello, J. M.; Holberg, J. B.; Atreya, S. K.; Donahue, T. M. Extreme ultraviolet observations from Voyager 2 encounter with Jupiter. **Science**, v. 206, p. 962–966, nov. 1979. 34

95   Bagenal, F. Torus-Magnetosphere Coupling. **NASA Special Publication**, v. 494, 1989. 34, 37

96   Ip, W.-H.; Goertz, C. K. An interpretation of the dawn-dusk asymmetry of UV emission from the Io plasma torus. **Nature**, v. 302, p. 232, mar. 1983. 36

97   Barbosa, D. D.; Kivelson, M. G. Dawn-dusk electric field asymmetry of the Io plasma torus. **Geophysical Research Letters**, v. 10, p. 210–213, mar. 1983. 36

98   Smyth, W. H.; Marconi, M. L. The Spatial Nature of the Iogenic Plasma Source near Io. In: **AAS/Division for Planetary Sciences Meeting Abstracts #30**. AAS: American Astronomical Society, 1998. (Bulletin of the American Astronomical Society, v. 30), p. 1117. 36

99   Smyth, W. H.; Peterson, C. A.; Marconi, M. L. A consistent understanding of the ribbon structure for the Io plasma torus at the Voyager 1, 1991 ground-based, and Galileo J0 epochs. **Journal of Geophysical Research (Space Physics)**, v. 116, p. A07205, jul. 2011. 36

100   Brown, R. A.; Pilcher, C. B.; Strobel, D. F. Spectrophotometric studies of the Io Torus. In: _____. **Physics of the Jovian Magnetosphere**. STI: In: Physics of the Jovian magnetosphere, 1983. p. 197–225. 41, 44

101   Brown, R. A. Jupiter's Sulfur Nebula. In: **Bulletin of the American Astronomical Society**. ADS: Bulletin of the American Astronomical Society, 1976. (Bulletin of the American Astronomical Society, v. 8), p. 468. 42

102   Chamberlain, J. W. **Physics of the aurora and airglow**. United States of America: Elsevier, 1961. 42

103   Hill, T. W.; Dessler, A. J.; Michel, F. C. Configuration of the Jovian magnetosphere. **Geophysical Research Letters**, v. 1, p. 3–6, 1974. 43

104   Mekler, Y.; Eviatar, A.; Coroniti, F. V. Sodium in the Jovian Magnetosphere. In: **Bulletin of the American Astronomical Society**. ADS: Bulletin of the American Astronomical Society, 1975. (Bulletin of the American Astronomical Society, v. 7), p. 387. 43

105   Pierce, A. K. The McMath solar telescope of Kitt Peak National Observatory. **Applied Optics IP**, v. 3, p. 1337, dez. 1964. 44

106   Wells, D. C.; Greisen, E. W.; Harten, R. H. FITS - a Flexible Image Transport System. **Astronomy and Astrophysics Supplement**, v. 44, p. 363, jun. 1981. 52

107   Lomb, N. R. Least-squares frequency analysis of unequally spaced data. **Astrophysics and Space Science**, v. 39, p. 447–462, fev. 1976. 62, 64

108   Scargle, J. D. Studies in astronomical time series analysis. II - Statistical aspects of spectral analysis of unevenly spaced data. **Astrophysical Journal**, v. 263, p. 835–853, dez. 1982. 62, 63, 64

109   Horne, J. H.; Baliunas, S. L. A prescription for period analysis of unevenly sampled time series. **Astrophysical Journal**, v. 302, p. 757–763, mar. 1986. 62, 64

110   Zechmeister, M.; Kürster, M. The generalised Lomb-Scargle periodogram. A new formalism for the floating-mean and Keplerian periodograms. **Astronomy and Astrophysics**, v. 496, p. 577–584, mar. 2009. 64

111   Carlson, R. W.; Weissman, P. R.; Smythe, W. D.; Mahoney, J. C. Near-Infrared Mapping Spectrometer experiment on Galileo. **Space Science Reviews**, v. 60, p. 457–502, maio 1992. 64

112   Lopes-Gautier, R.; Davies, A. G.; Carlson, R.; Smythe, W.; Kamp, L.; Soderblom, L.; Leader, F. E.; Mehlman, R.; Galileo NIMS Team. Hot spots on Io: Initial results from Galileo's near infrared mapping spectrometer. **Geophysical Research Letters**, v. 24, p. 2439, out. 1997. 64, 65, 67

113   Krüger, H.; Horányi, M.; Krivov, A. V.; Graps, A. L. Jovian dust: streams, clouds and rings. In: _____. **Jupiter. The Planet, Satellites and Magnetosphere**. UK: Cambridge University Press, 2004. p. 219–240. 77, 78, 83, 84

APPENDIX A

A.1 Conversion to Rayleighs

Jupiter is 5.4 MegaRayleighs/Angstrom (it is like a long rectangle on a brightness versus wavelength), and the torus [SII] 6731 Å line is essentially a delta function at 6731 Å +/-, its redshift due to the torus rotation. It means one redshift on the west and another on the east. It is assumed the torus material to rotate at the system III angular velocity and the ansae are at radius of Io's orbit ($\sim 6\ R_J$). Io's emission line will fall near the peak of the filter. The long rectangle for Jupiter will also be modified by the filter. In other words, the amount of light from Jupiter detected by the CCD is the integral of the whole filter profile times Jupiter's 5.4 MegaRayleighs/Angstrom. The integral of the whole filer profile ends up reading in units of Angstroms, it is a dimensionless fraction at each point. Then it is multiplied by the distance in angstroms between each point. This total number of angstroms for the filter it is equivalent width in angstroms. Once multiplied by 5.4 MR/A, it is the actual Rayleighs. It is also necessary to be divide by the neutral density filter, which means take the 5.4 MR/A and divide it by 10^4. Once the value of Jupiter is calculated in Rayleighs on the CCD, then it may be compared to the bias-subtracted, flat fielded and exposure time-divided signal it is seen for Jupiter (per pixel). This would read in ADU/s/pix. If it is divided by the gain of the CCD (electrons/ADU), electrons/s/pix.

So you have real Rayleighs for Jupiter on the CCD and detected signal for Jupiter on the CCD in ADU/s/pix. Divide these to get a conversion factor of Rayleighs/(ADU/s/pix). The ansa brightness obtained is in ADU/s (the ansae were divided by the exposure time).

In case the steps presented above are not clear, follows the step executed in IDL. The example presented was obtained in October 10 1997:

- 1 Rayleigh $\equiv \frac{10^6}{4\pi}$ photons $cm^{-2}\ sr^{-1}\ s^{-1}$

- Jupiter = 5.4 MegaRayleighs / Angstrom

- JUP-INTC = 2338.81 (Central Jovian intensity in a 11x7 pixel region)

- JUP-BKGD = 86.1122 (Background intensity near Jupiter)

ATV shows that this is per pixel, so to convert to ADU/pix in a 900 s exposure behind a 1E4 ND filter:

$$x(pixel\,to\,ADU/pix) = 2338.81 - 86.1122 = 2252.6978\,ADU/pix \qquad \text{(A.1)}$$

The idea is to get a conversion factor that goes from ADU in each pix in an exposure of a particular length to kR in each pix. The plate scale is 512 by 512 pixels and to get the right ascension (RA) and declination (DEC) it is necessary to use ephemeris. It was used the Horizon Web-Interface ($ssd.jpl.nasa.gov/horizons.cgi$)

- Image = 512 x 512 pixels

- Comment: Io and Europa, 1 sec, 03:36UT

- Observation was made 20/09/97 09:33:23 (UT).

From the Horizon Web-Interface:

- SITECOORD = 248.405325000, 31.958416667, 2.06675

moon	R.A.(ICRF/J2000.0)	DEC (ICRF/J2000.0)	R.A.(a-apparent)	DEC Azi (a-appr)
Io	21 01 45.94	-17 57 14.6	21 01 38.81	-17 57 38.3
Europa	21 01 43.84	-17 57 23.0	21 01 36.71	-17 57 46.7

Converting to decimal degrees:

a) RA1 = 21./24.*360 + 01/60. + 38.81/3600.

b) DC1 = -1. * (17 + 57/60. + 38.3/3600.)

c) RA2 = 21/24.*360 + 01/60. + 36.71/3600.

d) DC2 = -1. * (17 + 57/60. + 46.7/3600.)

dis = 30.946204838078280 arcsec

sqrt($(113.8 - 139.4)^2 + (362.1 - 329.9)^2$) = 41.1364 pix

print, dis / sqrt($(113.8 - 139.4)^2 + (362.1 - 329.9)^2$) = 0.75228343 arcsec/pix

Then check with a Jupiter image. On that night Jupiter angular diameter was 46.00166 arcsec

Using aperture tool:

$30. * 2. * 0.75228343 = 45.137009$ arcsec

~ 1 arcsecond is good enough. Then WEST AUX PLATE SCALE obatined was 0.75228343 arcsec/pix

The next step is to make a system variable with this:

$$sr =$$

(!dradeg $*3600d)^2d$ 42545170296.152206 = 4.25E10 $arcsec^2$ (A.2)

Working out filter characteristics assuming simple Gaussian with 50 % transmission and 10 A FWHM.

The integral of a Gaussian ($a* \exp$(-1d $* (x - b)^2/(2d*$ c)))is :

$$a * c * sqrt(2d * \pi) \tag{A.3}$$

where a is the height (peak transmission of filter), c is sigma, and b is the central wavelength.

$$FWHM = 2d * sqrt(2d * ln(2d)) * c \tag{A.4}$$

so

$$c = FWHM/(2d * sqrt(2d * ln(2d))) \tag{A.5}$$

In our case FWHM = 10A and a = 0.5

So integral over all angstroms of Gaussian filter profile is

$$a * c * sqrt(2d * \pi) \tag{A.6}$$

$$0.5 * 10d/(2d * sqrt(2d * alog(2d))) * sqrt(2d * \pi) \tag{A.7}$$

This is the equivalent width of the filter in angstroms assuming a signal of constant strength 1 per angstrom is 5. It would be about 10 if transmission was 1. Our constant strength is 5.4 MR/A, so Jupiter's signal going through the narrow-band filter, but not including ND filter:

$$0.5 * 10d/(2d * sqrt(2d * alog(2d)))$$
$$*sqrt(2d * \pi) * 5.4 \tag{A.8}$$
$$= 28.740610032220530 MR/A * A$$

Convert to real photon units 1 Rayleigh is 1E6 phot/cm^2/s/sr:

$$0.5 * 10d/(2d * sqrt(2d * alog(2d))) * sqrt(2d * \pi)$$
$$*5.4 * 1D6 * 1D6 = 28740610032220.535 \tag{A.9}$$

which unit is phot/cm^2/s/sr and it is still without the ND filter.

Recaping:

$$x = 2338.81 - 86.1122 = 2252.6978 ADU/pix \tag{A.10}$$

The result was in a 900 s exposure behind a 1E4 ND filter. Divided by exposure time / (arcsec/pix) * (arcsec/sr) / area of telescope and correct for ND filter:

$$(2338.81 - 86.1122)/900d/0.75d$$

$$*42545170296.152206/(90d/2d)^2 * 1D4 \qquad \text{(A.11)}$$

$$= 701171689131.77869(ADU/pix/s/(arcsec/pix) * NDfilter)$$

That is ADU/s/cm^2/sr in front of ND filter, but behind narrow-band filter. Now it is possible to convert the factor of photons/ADU:

$$0.5 * 10d/(2d * sqrt(2d * alog(2d))) * sqrt(2d * \pi)$$

$$*5.4 * 1D6 * 1D6/((2338.81 - 86.1122)/900d/0.75d$$

$$*42545170296.152206/(90d/2d)^2 * 1D4) \qquad \text{(A.12)}$$

$$= 40.989404560541239(photons/ADU)$$

For this particular 900s exposure with (JUP-INTC)-(JUP-BKGD) = 2252.6978. So if we multiply the image by this factor, we get the correct number of photons in each pixel and not accounting for the effect of the narrow-band filter on those photons. Then convert back to 1E6 phot/cm^2/s/sr to get Rayleighs. That means it is necessary to multiply by almost the whole factor we used before to convert to ADU/s/cm^2/sr.

$$1d/1d6 * 1d/900d/0.75d * 42545170296.152206/(90d/2d)^2$$

$$= 1E6(phot1/s1/sr1/cm^2) \qquad \text{(A.13)}$$

But it was just divided by that, so everything but the neutral density filter cancels out:

$$0.5 * 10d/(2d * sqrt(2d * alog(2d)))$$

$$*sqrt(2d * \pi) * 5.4 * 1D6/((2338.81 - 86.1122) * 1D4) \qquad \text{(A.14)}$$

$$= 1.2758307226250569$$

R/ADU for this particular exposure, and that is the conversion factor, but it also need to consider spectral response. Jupiter is a continuum source and the IPT is a mono-chromatic source. Lets assume the IPT falls on the peak of the filter transmission. The calculation was made to have all Jupiter's photons fall into that wavelength. The size of the box used in this example is $25 * 25$ pixels:

$$214026.3/(25d * 25d) = 342.44207499999999 \tag{A.15}$$

So this is what we want to convert to Rayleighs:

$$
\begin{aligned}
0.5 * 10d/(2d * sqrt(2d * alog(2d))) * sqrt(2d * \pi) \\
*5.4 * 1D6/((2338.81 - 86.1122) * 1D4) \\
*214026.3/(25d * 25d) \\
= 436.89812000447392(R/ADU * \text{ADU/pix})
\end{aligned}
\tag{A.16}
$$

The value obtained is a reasonable one, especially after it is compared with the results obtained by Nozawa et al. (2004) (28).

The demonstration lead us to the general conversion to Rayleighs to be:

$$
\begin{aligned}
0.5 * 10d/(2d * sqrt(2d * alog(2d))) \\
*sqrt(2d * !dpi) * 5.4 * 1D6 \\
/((JUPINTC - JUPBKGD) * 1D4) * BOXVALUE/(PIXinBOX)
\end{aligned}
\tag{A.17}
$$

where BOXVALUE is the background-subtracted total ADU value in the ansa box and PIXinBOX is the total number of pixels in that box. Once the background is subtracted from the images, we just multiply the image by the formula up to BOXVALUE so that each pixel will read in Rayleigh.

APPENDIX B

B.1   Statistical errors

To calculate the statistical errors it is necessary to obtain some information from the header of the image:

- GAIN-SET = 4 (Detector Gain Setting: 1 (low) or 4 (high))

- GAIN-1 = 4.90000 (e^-/ADU)

- GAIN-4 = 1.20000 (e^-/ADU)

Once the bias is subtracted bias, multiply it by 1.2 e^-/ADU in order to get electrons. After the pixels are read in electrons, then it is possible to calculate the error using Poisson statistics:

$$error = SQRT(number - of - electrons) \qquad (B.1)$$

The fractional error is then:

$$x = SQRT(number - of - electrons)/number - of - electrons \qquad (B.2)$$

As the box was so big and encompassed so many ADU (basically electrons), the fractional Poisson error is very small. But the Poisson statistics is just part of the picture. The fact that the box is a box and doesn't encompass the perfect torus shape, it means it is necessary to do some systematic errors. That is, the system to determine the number of electrons in the ansa is not perfect. The determination of the background has the same problem. It was used the ATV for measuring the counts in the boxes. By experimenting with different aperture sizes and ATV parameters, it was found something between 10 - 20 %. Note the estimated systematic error of 10 - 20 % of estimating the counts in the boxes doesn't include the effect of scattered light non-uniformity ("sword"). At this point it is not possible to determine the systematic uncertainty caused by the azimuthally scattered light.

ANEXO A - GALILEO MISSION

Table A.1 gives the summary of the name and number of the flybys performed by the Galileo mission. The orbit and flybys were already explained in the text and the table gives a summary of important information such as closest approaches and important characteristics observed at Io. Table was adapted from Lopes and Williams (2005) (33).

Orbit	Mission	Flyby moons	Closest approach distance to Io (km)	Notable Io activities
J0		Io	897	Fields and particles observations
G1		Ganymede	697.000	NIMS dayside and nightside maps, first eclipse images
G2		Ganymede	441.000	NIMS maps
C3		Callisto	244.000	Topography of anti-Jupiter hemisphere
E4		Europa	321.000	Global color imaging
5		None		
E6		Europa	401.000	Eclipse imaging
G7		Ganymede	531.000	NIMS observations of Loki
G8		Ganymede	956.000	Eclipse imaging, auroral emissions
C9		Callisto	607.000	Discovery of Pillan eruption
C10		Callisto	319.000	Dark Pillan deposits
E11		Europa	780.000	SSI plume inventory
E12	GEM	Europa	485.000	NIMS spectral maps
13	GEM	None	438.000	
E14	GEM	Europa	252.000	Multi-spectral color of anti-Jupiter hemisphere
E15	GEM	Europa	312.000	Best UVS observation
Continued on next page				

Orbit	Mission	Flyby satellite	Closest approach distance to Io (km)	Notable Io activities
E16	GEM	Europa	702.000	NIMS spectral maps
E17	GEM	Europa	800.000	
E18	GEM	Europa	996.000	
E19	GEM	Europa	856.000	
C20	GEM	Callisto	789.000	NIMS spectral maps
C21	GEM	Callisto	127.000	Best SSI resolution
C22	GEM	Callisto	737.000	Distant plume monitoring
C23	GEM	Callisto	448.000	
I24	GEM	Io	611	First close-up remote sensing
I25	GEM	Io	301	Tvashtar eruption images (SSI, NIMS)
E26	GMM	Europa	340.000	NIMS maps
I27	GMM	Io	198	high-resolution remote sensing
G28	GMM	Ganymede	379.000	
G29	GMM	Ganymede	963.000	Tvashtar plume and NIMS maps
G30		Ganymede	342.000	NIMS dayside and nightside maps
I31		Io	194	Discovery of Thor eruption (NIMS and SSI)
I32		Io	184	high-resolution remote sensing
I33		Io	102	
A34		Amalthea	45.800	
J35		Jupiter	impact	

PUBLICAÇÕES TÉCNICO-CIENTÍFICAS EDITADAS PELO INPE

Teses e Dissertações (TDI)

Teses e Dissertações apresentadas nos Cursos de Pós-Graduação do INPE.

Notas Técnico-Científicas (NTC)

Incluem resultados preliminares de pesquisa, descrição de equipamentos, descrição e ou documentação de programas de computador, descrição de sistemas e experimentos, apresentação de testes, dados, atlas, e documentação de projetos de engenharia.

Propostas e Relatórios de Projetos (PRP)

São propostas de projetos técnico-científicos e relatórios de acompanhamento de projetos, atividades e convênios.

Publicações Seriadas

São os seriados técnico-científicos: boletins, periódicos, anuários e anais de eventos (simpósios e congressos). Constam destas publicações o Internacional Standard Serial Number (ISSN), que é um código único e definitivo para identificação de títulos de seriados.

Pré-publicações (PRE)

Todos os artigos publicados em periódicos, anais e como capítulos de livros.

Manuais Técnicos (MAN)

São publicações de caráter técnico que incluem normas, procedimentos, instruções e orientações.

Relatórios de Pesquisa (RPQ)

Reportam resultados ou progressos de pesquisas tanto de natureza técnica quanto científica, cujo nível seja compatível com o de uma publicação em periódico nacional ou internacional.

Publicações Didáticas (PUD)

Incluem apostilas, notas de aula e manuais didáticos.

Programas de Computador (PDC)

São a seqüência de instruções ou códigos, expressos em uma linguagem de programação compilada ou interpretada, a ser executada por um computador para alcançar um determinado objetivo. Aceitam-se tanto programas fonte quanto os executáveis.